THE DOSIMETRY OF LOW ENERGY X-RAYS

by

Anthony Thomas Redpath, B.Sc.

Thesis presented for the Degree of Doctor of Philosophy of the University of Edinburgh in the Faculty of Medicine, October, 1967.

CONTENTS

A B S T R A C T

The energy fluence of various X-ray beams generated at 30kV and below has been determined absolutely by calorimetry. The X-ray unit used has a Machlett, beryllium window tube, and a constant potential generator. The calorimeter is of the constant temperature environmental type employing twin gold absorbers. A large amount of thermal damping has been used to reduce the effects of room temperature variations, and temperature drift rates in the detector of better than 10^{-4}°C per min. are always obtainable with a relatively simple system. X-ray intensities in the range 1 to 100μW per cm^2 at the absorber have been measured to an accuracy of ± 0.5%.

Temperature changes were detected by employing thermistors in an a.c. Wheatstone bridge, and conditions for optimum operation of this bridge have been investigated. The out of balance signal was amplified, passed through a phase sensitive detector and displayed on a recorder. Impedance matching has been used throughout the system.

Various methods of operation of the calorimeter have been discussed, and an experimental comparison of their merits obtained. It has been shown that a method of thermal cycling, as developed, provides the most accurate method of measurement with a vast saving in operational time.

Under identical experimental conditions, a comparison of the calorimeter response with that of various secondary dosimeters has been made. An ionization chamber operated at pressures of up to three atmospheres of argon has been used to totally absorb the various X-ray beams. The saturation of this chamber has been fully investigated, and currents obtained were integrated on capacitors of accurately known value. This has yielded a $\bar{W}$ value for argon of 26.3 ± 0.2SeV per ion pair, and no significant variation of $\bar{W}$ in the energy

range investigated was found. A further comparison of calorimetric dosimetry with ferrous sulphate and solid state dosimetry, has yielded G values for ferrous sulphate and $\bar{W}$ values for silicon, in a similar energy range. The results obtained are estimated to be correct to $\pm$ 1%, constituting a great improvement over previously determined values.

Finally a theory to estimate the energy loss due to radiation scattered from each of these dosimeters has been produced. Corrections to be applied for each X-ray beam used have been made.

CHAPTER 1

INTRODUCTION

1.1 The Dosimetry of X-rays

X-rays possess certain well known properties and the utilization of these properties forms the basis of an X-ray dosimeter. The temperature rise produced when an X-ray beam is attenuated in a medium is a fundamental measurement of the energy in that beam. However the small temperature rises involved make this a very insensitive method of dosimetry. Hence calorimetry is rarely used in routine measurements, but is only used to calibrate more robust and sensitive dosimeters.

An essential feature of calorimetry is that all the X-ray energy deposited in the medium concerned is converted into thermal energy, for in certain media this energy may produce biological and chemical effects. For obvious reasons the biological effect of X-rays is not used as a dosimeter, but the chemical effect has long been used. Perhaps the best established of the chemical methods is the ferrous sulphate dosimeter, which uses the conversion of ferrous ions to ferric ions as a measure of the absorbed dose.

Solid-state systems have recently produced a large impact on dosimetry; semiconductors, plastics and even glass have been used. The thermo-luminescent property of lithium fluoride has probably made it the most valuable recent dosimeter (1).

An intermediate step in the absorption of X-rays is the ionization and excitation which is produced by the liberation of secondary electrons. Gases are readily ionized by the action of X-rays, and the ions produced

by these secondary electrons can be collected by an applied electric field between two electrodes in a gas. This constitutes an ionization chamber and provides an extremely sensitive dosimeter. $\bar{W}$, which is the mean energy required to produce an ion pair, varies with the gas used, may vary with the energy of the incident radiation, and so it must be known before an ionization chamber can be used as a dosimeter. Its determination necessitates the intercomparison of an ionization chamber with a calorimeter under controlled experimental conditions.

1.2 Aim of experiment.

The aim of this work is to measure, in absolute units, the energy in various beams of X-rays generated at 30kVp and below, using a total absorption calorimeter. A comparison is then to be effected between this calorimeter and a total absorption ionization chamber, and $\bar{W}$ values for argon determined for these various X-ray beams.

1.3 Principles of calorimetry.

A calorimeter consists of an absorber of thermal capacity k at a temperature Θ, which is thermally isolated from its surroundings at a temperature Θ_o. The system obeys Newton's law of cooling which states that

$$k \left(\frac{d\Theta}{dt}\right)_c \propto \Theta - \Theta_o \qquad \ldots\ldots\ldots 1 - 1$$

Assuming $\Theta > \Theta_o$, and the absorber is losing heat to the surroundings, then

$$k \left(\frac{d\Theta}{dt}\right)_c = - L (\Theta - \Theta_o) \qquad \ldots\ldots\ldots 1 - 2$$

The constant of proportionality L is the thermal leakage constant of the system. If a power P is liberated in the absorber, and this causes the

temperature to rise, then

$$k \left(\frac{d\Theta}{dt}\right)_H = P - L(\Theta - \Theta_o) \qquad \ldots\ldots\ldots 1 - 3$$

There are three principal types of calorimeter.

1.3.1 Adiabatic

In adiabatic calorimeters the temperature of the surroundings is made to rise with the temperature of the absorber, so at all times $\Theta = \Theta_o$. Equation 1 - 3 then reduces to

$$k \left(\frac{d\Theta}{dt}\right)_{H \text{ at } \Theta = \Theta_o} = P \qquad \ldots\ldots\ldots 1 - 4$$

$\left(\frac{d\Theta}{dt}\right)_H$ is measured experimentally. P can be determined by a knowledge of k or by calibration, that is by introducing known values of P into the absorber. This operation is ideal but difficult in practice. The temperature of the surroundings has to be measured, and a feedback system, usually employing a servomotor, used to control this temperature (Genna, Jaeger, Nagl and Sanielevici (2)). Although heat losses are reduced, perfect temperature control cannot be achieved, and the evaluation of the remaining heat losses may be difficult. Adiabatic calorimeters have not, in general, been widely used. They have been used for the measurement of high dose rates (Myers, Le Blanc and Fleming (3)).

1.3.2 Isothermal

The only noted isothermal calorimeters which have been used are ice-calorimeters. It appears that for high dose rates ice calorimeters can achieve high accuracy (Ginnings, Ball and Vier (4)), but they are not convenient for microcalorimetry. The calorimeter absorber consists of a

thermally insulated ice-water mixture, and a decrease in volume of this mixture occurs when energy is dissipated in the absorber. This can be measured by observing the fall of the ice-water mixture in a capillary tube. The difficulty is in obtaining thermodynamic equilibrium, lack of which produces random changes in absorber volume.

1.3.3 Constant temperature environment

In constant temperature environment calorimetry θ_o is maintained constant at all times. Equation 1 - 3 then solves to give

$$\theta - \theta_o = \frac{P}{L}\left\{1 - \exp\left(\frac{-Lt}{k}\right)\right\} \qquad \ldots\ldots\ldots 1 - 5$$

and an exponential variation of temperature with time is observed.

Numerous methods of achieving a constant temperature environment have been used. Thermal baths have been widely used, and it is necessary to minimise thermal gradients within these baths. A large amount of stirring together with thermostatic control is therefore required. The liquid bath requires a high thermal conductivity, and it is suggested that water, as used by Genna and Laughlin (5) and Myers et al (3), is probably the best liquid to use. Transformer oil was used by Laughlin, Beattie, Henderson and Harvey (6) and by Kruglov and Lopatin (7), but no reason was given for this use. Schleiger, Goldstein and Tochilin (8) used ethylene glycol to minimise corrosion. Dove and Cole (9) used an ice-water bath and reported it to be stable to $0.0001^{\circ}C$. The ice bath has an advantage in size, as thermostated baths required a large volume for efficient temperature stability (3). Liquid nitrogen was used by Gomberg et al (10) and by Goldstein Schleiger and Tochilin (11). The latter found temperature control

rather difficult, but, as will be shown, if control can be achieved the advantages to be gained by operation at very low temperatures are substantial.

Thermal damping has been used by Goodwin (12) for absorbed dose measurements of low and medium kilovoltage X-rays. The absorber was embedded in tissue equivalent wax. Temperature control should have been improved by using a vacuum system. Tian (13) proposed a system whereby the absorber is surrounded by a series of shells, which are alternately constructed of insulating and conducting media. This thermal damping system may virtually eliminate any temperature variations in the calorimeter jacket. This principle was used by Genna et al (2).

One of the main problems with a beam calorimeter is the necessity for an entrance window which must not attenuate the beam to any extent. This immediately produces a region in which temperature control is extremely difficult. This problem is even more critical with low-energy X-ray or electron beams where the window must be very thin indeed.

There are several methods of determining the input power in constant temperature environment calorimetry.

1.3.3.1 Steady state method.

The experiment is allowed to continue to infinite time, until a steady state temperature Θ_∞ is attained. Equation 1 - 5 then gives

$$P = L(\Theta_\infty - \Theta_o) \qquad \ldots\ldots\ldots 1 - 6$$

and from this L must be determined. This method, as used by Radak and Markovic (14), does not determine the initial slope of the exponential and therefore depends on heat losses remaining constant during a particular

Figure 1

KINETIC METHOD OF MEASUREMENT

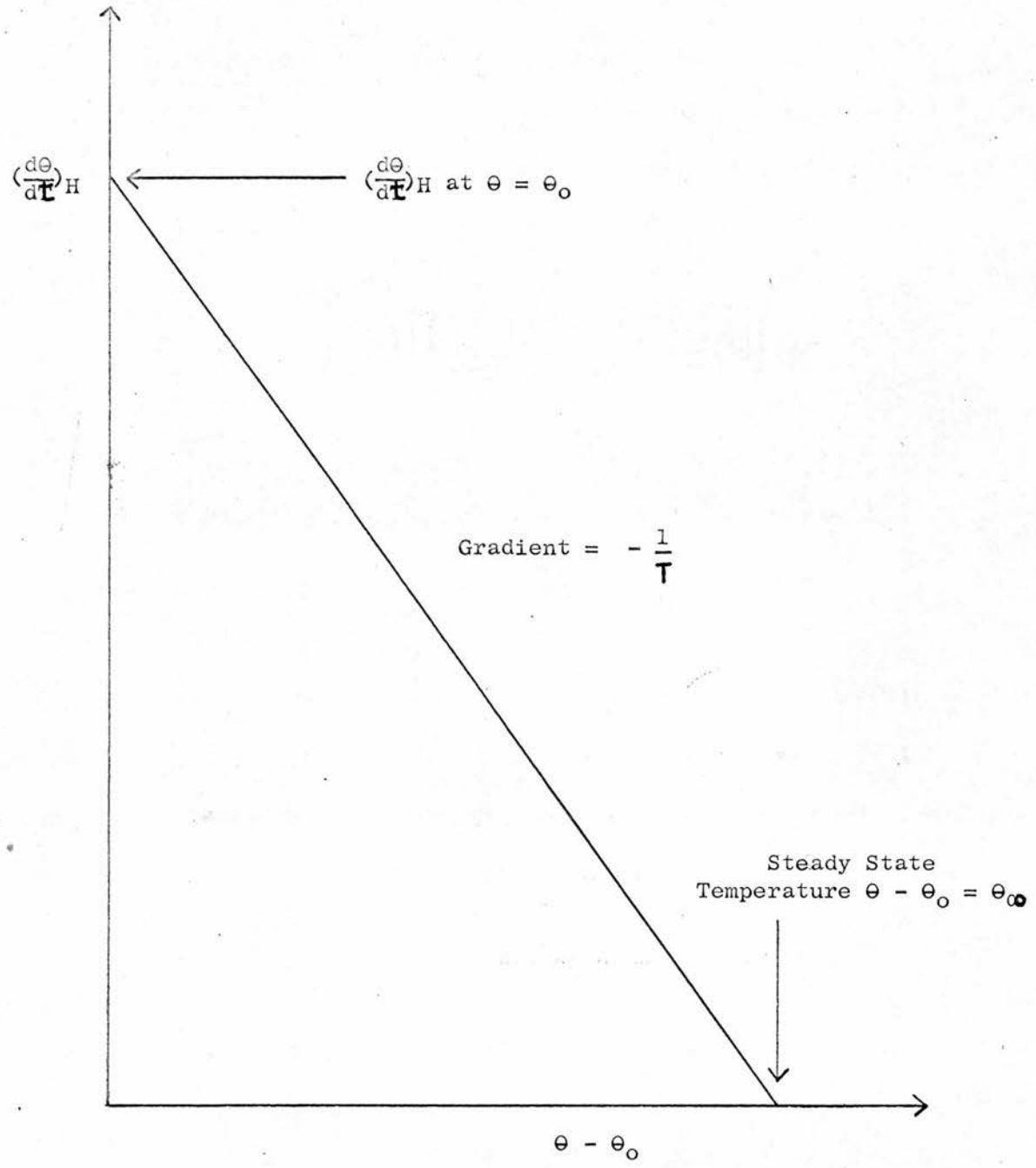

series of experiments. Good environmental temperature control is also required, and the time taken to reach the steady state temperature may be considerable. Reducing this time, that is reducing the time constant of the system, results in poorer temperature control and sensitivity.

1.3.3.2 Heating and cooling rates

The heating and cooling rates of the absorber are determined at the same temperature above the surroundings. Addition of equations 1 - 2 and 1 - 3 gives

$$k\left(\frac{d\theta}{dt}\right)_H + k\left(\frac{d\theta}{dt}\right)_C = P$$

At any temperature above the surroundings

$$\left(\frac{d\theta}{dt}\right)_H + \left(\frac{d\theta}{dt}\right)_C = \text{a constant} = \left(\frac{d\theta}{dt}\right)_H \text{ at } \theta = \theta_o$$

and the result is the same as in the adiabatic operation. This method was previously used by Redpath, Law, Greening and Randle (15).

1.3.3.3 Kinetic method

If in equation 1 - 3, $\left(\frac{d\theta}{dt}\right)_H$ is plotted against $\theta - \theta_o$ a straight line is obtained as shown in figure 1. From this is obtained

1. The steady state temperature θ_∞ when $\left(\frac{d\theta}{dt}\right)_H = 0$
2. $\left(\frac{d\theta}{dt}\right)_H$ at $\theta = \theta_o$ as in the adiabatic operation.
3. The time constant of the system $T = \frac{k}{L}$

This method was used by Keene and Law (16) and by Radak and Markovic (14). The latter compared the steady state temperature obtained by this method with that obtained by operation as described in 1.3.3.1.

These last two methods take into account any variation in heat losses within the system. However the inaccuracy involved in both methods

Figure 2

SEMI ADIABATIC METHOD OF MEASUREMENT

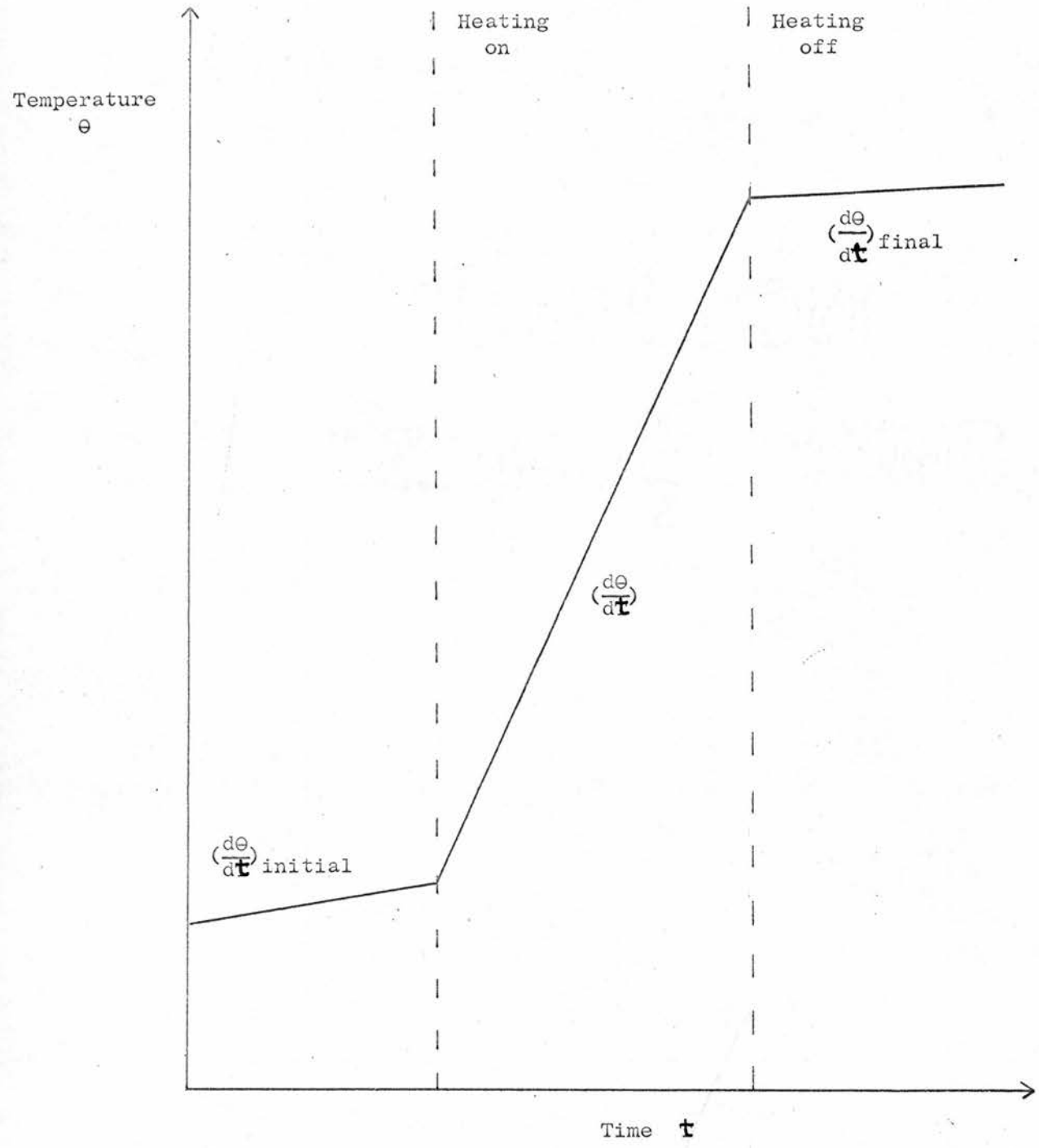

occurs in drawing tangents in order to obtain the heating rate at a particular point on the exponential.

1.3.3.4 Semi-Adiabatic

If the time of observation $t \ll T$ the time constant of the system, then equation 1 - 5 can be expanded to give

$$\theta - \theta_o = \frac{P}{L}\left\{1 - (1 - \frac{Lt}{k})\right\}$$

$$\theta - \theta_o = \frac{Pt}{k} \qquad \ldots\ldots\ldots 1 - 7$$

and $$\left\{\frac{\theta - \theta_o}{t}\right\}_{t \ll T} = \left(\frac{d\theta}{dt}\right)_H \text{ at } \theta = \theta_o$$

Measurements are now being taken of the linear part of the exponential and equation 1 - 7 is again the same as in the adiabatic operation. A response curve as shown in figure 2 is obtained. The initial and final temperature drift rates of the absorber are averaged, and this correction applied to the measured heating rate, giving

$$\left(\frac{d\theta}{dt}\right)_H = \left(\frac{d\theta}{dt}\right) - \frac{1}{2}\left\{\left(\frac{d\theta}{dt}\right)_{\text{initial}} + \left(\frac{d\theta}{dt}\right)_{\text{final}}\right\}$$

Genna and Laughlin (5) used this method in calibrating a Cobalt-60 gamma-ray beam. This method is very successful when working with calorimeters which have a small thermal leakage constant. When working with low energy X-rays, the absorber must, out of necessity, have a high area to heat capacity ratio, resulting in a high thermal leakage constant. The drawback of this method in this case is that X-ray exposures have to be short ($t \ll T$), and so accurate timing is required.

1.3.3.5 Temperature rise after a measured time

The heating time is so chosen to be sufficiently short that heat

losses only have a second order effect on the results, but sufficiently long to be accurately measured. Various methods, which will be described later, can be used to measure this temperature rise. Bewley (17) used the ohmic out of balance of a thermistor bridge, but this is subject to sensitivity changes in the measuring system.

1.3.3.6 Thermal cycling

The absorber is allowed to cool from temperature Θ_1 to Θ_2 and is heated from Θ_2 to Θ_1, and the cooling and heating periods are measured. There is no noted use of this method, but Dove and Cole (9) give a mathematical analysis -

After the cooling period t_1, $\Theta_2 - \Theta_s = (\Theta_1 - \Theta_s)\exp\left(-\frac{Lt_1}{k}\right)$

Θ_s is the temperature of the surroundings.

After the heating period t_2,

$$\Theta_1 - \Theta_s = \left\{1 - \exp\left(-\frac{Lt_2}{k}\right)\right\}\frac{P}{L} + (\Theta_2 - \Theta_s)\exp\left(-\frac{Lt_2}{k}\right)$$

Eliminating Θ_s,

$$P = \frac{L}{2}(\Theta_1 - \Theta_2)\left\{\coth\left(\frac{Lt_1}{2k}\right) + \coth\left(\frac{Lt_2}{2k}\right)\right\}$$

or approximately.

$$P = k(\Theta_1 - \Theta_2)\left(\frac{1}{t_1} + \frac{1}{t_2}\right) \qquad \ldots\ldots\ldots 1 - 8$$

and they quote the error in P to be less than 0.3% provided t_1 and t_2 are less than $0.2\frac{k}{L}$ ($< 0.2T$).

Therefore $P \propto \frac{1}{t_1} + \frac{1}{t_2}$ and a comparison of known input powers against a particular X-ray beam can be made without allowing the absorber to cool to an equilibrium temperature, giving a vast saving in operational time.

Methods 1.3.3.1, 1.3.3.2 and 1.3.3.3 have initially been rejected

Table 1

Calorimetric Measurements of Energy Fluence

Date	Authors	Energy	Absorber	Intensity	Detector
1926	Kulenkampff (20)	6-22 kVp	Silver foil	1 $\mu W/cm^2$ ± 5%	Thermocouple
1927	Rump (22)	43-150 kVp	Mercury	100 $\mu W/cm^2$ ± 1.6%	Capillary rise
1928	Crowther and Bond (21)	50 kVp	Oil	200 $\mu W/cm^2$ ± 2%	Thermocouple
1953	Laughlin et al. (23)	400 kVp	Lead Cylinders	100 $\mu W/cm^2$ ± 1%	Thermistors
1959	Pauly (24)	25-45 kVp	Aluminium, Copper, Lead, Plexiglass	50-50,000 $\mu W/cm^2$ ± 2%	Thermocouple
1965	Cockelbergs et al. (25)	30-60 kVp	Gold foil	100-1,000 $\mu W/cm^2$ ± 7%	Thermocouple
1965	Gomberg et al. (10)	5-10 keV	Gold foil	1-5 $\mu W/cm^2$ ± 2.5%	Thermistors

for reasons given, but an experimental comparison of methods 1.3.3.3, 1.3.3.4, 1.3.3.5 and 1.3.3.6 has been carried out.

1.4 Review of total absorption calorimetry of X-rays

The work in this thesis is entirely concerned with beam calorimetry, and as calorimetry in general covers a vast field, it is only intended to deal with this particular aspect of calorimetry. Calorimetry is a well established and widely used technique, and Gunn (18, 19) has given a comprehensive survey of the whole field. Table 1 summarises the published work in the field of total absorption calorimetry of low energy X-rays. All calorimeters used were of the constant temperature environmental type. In the early work sensitivity and precision were limited mainly due to insensitive temperature detection by thermocouples. The detection circuits of Kulenkampff (20) and of Crowther and Bond (21) only consisted of a sensitive galvanometer across which the thermocouples were connected. Environmental temperature control was rather crude. Estimations of X-ray energy loss due to scatter contributed a large amount to the uncertainty in these results. It is interesting to note that Rump (22) used a cup-shaped calorimeter body in his experiments, hence reducing the energy loss from the front surface. He measured the expansion of the mercury forming the absorber by capillary rise to $\pm$ 1.6%. However much sensitivity must have been lost by the extra thermal capacity introduced by use of such an absorber.

The advent of thermistors increased the sensitivity of calorimetry and the first noted use of these was by Laughlin in 1951 (23). The same paper is also the first recorded use of a twin calorimeter. The principle here involved, is that a second unirradiated absorber is included in the

calorimeter, and the temperature difference between the two absorbers is now measured. These two absorbers are matched in their thermal capacity, and placed in similar geometrical surroundings, within the calorimeter. External temperature variations then affect both in a similar manner, and hence are effectively reduced. Laughlin used various temperature controlled baths (5, 6) surrounding twin lead absorbers, and measured 400 kVp X-rays to $\pm$ 1% (6).

Thermocouples have still been used by Pauly (24) and Coekelbergs (25) but uncertainties in their results are rather high. These are due to inadequate environmental temperature control; Coekelbergs did not consider evacuation of the calorimeter system, and the absorber - window distance in Pauly's calorimeter was too small. Gomberg et al (10) have produced the most worthwhile work in this group. They used a liquid nitrogen calorimeter, evacuated to 10^{-7} mm Hg by means of an ion pump. A d.c. thermistor bridge was used for temperature detection, but this could have been improved by the use of an a.c. system. They claim a $\pm$ 2% error in the electrical calibration circuit due to the use of a $\mu\mu$ ammeter, whereas a simple standardised voltage source would have reduced this error. Although an excellent calorimeter was produced, they lost much in their choice of detection and calibration circuits. However, a detection limit of 0.6μ watts cm^{-2} was obtained, and the overall error in a measurement was $\pm$ 2.5%.

Figure 3

POWER TRANSFER IN CALORIMETER SYSTEM

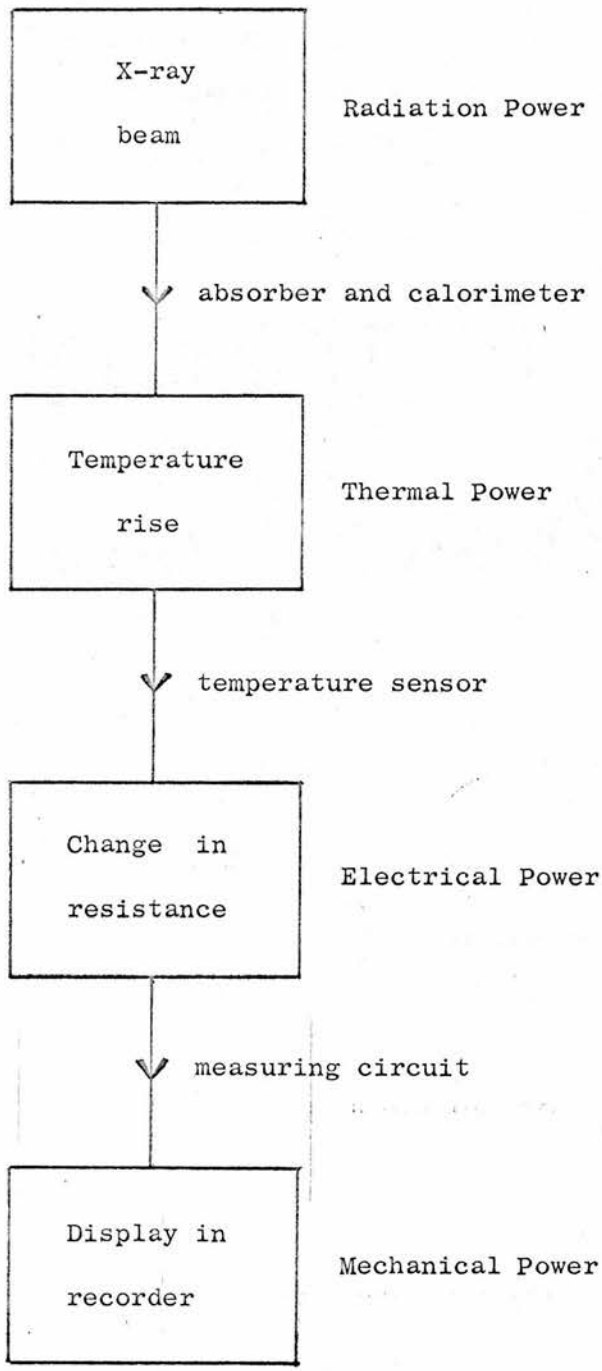

CHAPTER 2

DESCRIPTION OF CALORIMETER

2.1 Introduction

In a system where extreme sensitivity is required, it is essential that at every point in this system power transfer is maximised. The power transfer in a calorimeter system can be represented as shown in figure 3.

It is the purpose of the calorimeter to maximise the temperature rise for a given input power. Two points have to be considered here; firstly the medium in which the X-rays are absorbed, and secondly the environment in which the absorber exists.

2.2 Choice of absorbing element

Consider an absorber of thickness t, density ρ, and surface area A. A monochromatic beam of intensity I_o is incident upon the absorber and the transmitted intensity is I.

$$\text{Then} \quad I = I_o \exp\left(-\frac{\mu}{\rho}\right)(\rho t) \qquad \ldots\ldots\ldots 2 - 1$$

where $\frac{\mu}{\rho}$ is the mass attenuation coefficient of the absorber for the beam in question.

$$\text{Therefore} \quad t = \frac{1}{\rho\left(\frac{\mu}{\rho}\right)} \ln \frac{I_o}{I} \qquad \ldots\ldots\ldots 2 - 2$$

and the mass of the absorber

$$M = \frac{A}{\left(\frac{\mu}{\rho}\right)} \ln \frac{I_o}{I} \qquad \ldots\ldots\ldots 2 - 3$$

If S is the specific heat of the absorber, and an energy deposition E per unit area produces a temperature rise Θ, then

$$EA = MS\Theta$$

$$\Theta = \frac{E\left(\frac{\mu}{\rho}\right)}{S \ln \frac{I_o}{I}} \qquad \ldots\ldots\ldots 2 - 4$$

This analysis tells us that the absorbing medium must have a low specific heat and a high μ/ρ (or high atomic number). Other factors which govern the choice of absorber are thermal conductivity and emissivity. Thermal conductivity must be good so that any heat deposited is quickly spread throughout the absorber giving a uniform temperature rise. Thermal emissivity must be low so that radiation heat transfer between the absorber and its environment is minimised.

The X-ray beam to be used is expected to contain a considerable fraction of tungsten L-characteristic radiation. If the L-absorption edge of the absorber is at a lower energy than the tungsten L-radiation there will be a greater loss of energy from the absorber through the escape of fluorescent radiation. So it is essential that the L-absorption edge is at a higher energy. After a consideration of all these facts gold was chosen as the absorbing element.

2.3 Construction of absorber and heater

The absorber is constructed of three 0.025mm thick gold foils each two centimetres square, and this will absorb more than 99.9% of 20keV photons. The centre foil has a heating coil wound around it in order to simulate the radiation heating by electrical heating. In constructing the coil two points have to be taken into consideration. Firstly the percentage resistance of the coil which is not embedded in the absorber must be small, in order that power developed in the coil only heats the absorber. Thus the length of the coil should be maximised. Secondly the coil resistance must be large so that relatively large voltages can be used to develop small powers. This entails using wire of small diameter, and thus provides a reduction in heat conduction losses from the absorber along

Figure 4

ABSORBER CONSTRUCTION

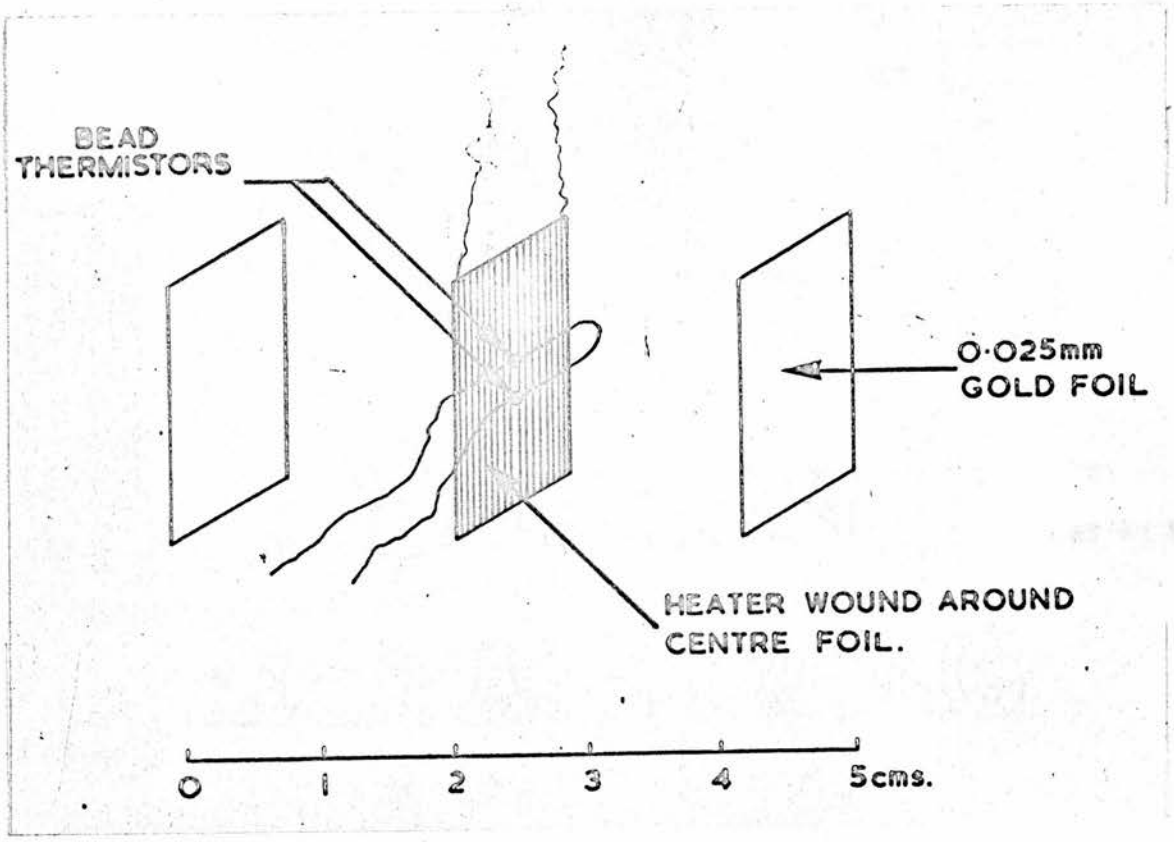

Figure 5

ABSORBER SUSPENSION

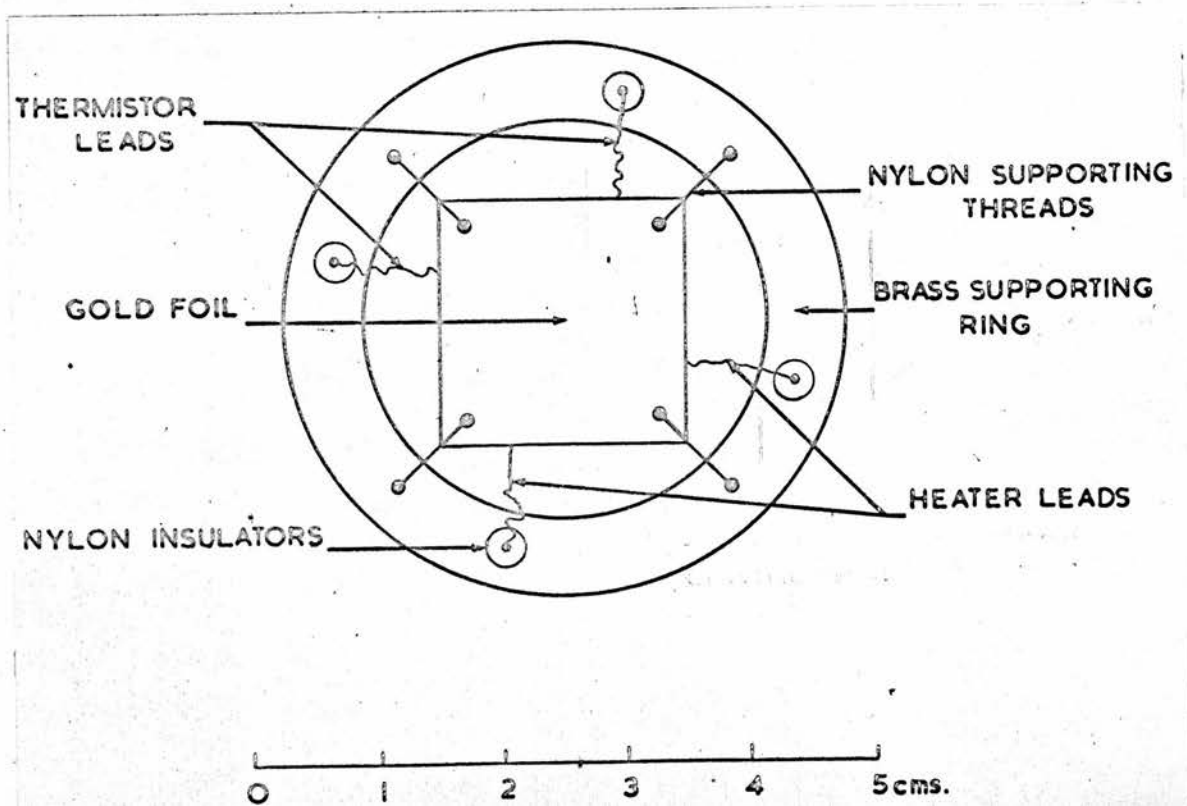

these wires. The wire used was Evanohm (26), resistance 103 Ω/cm, and diameter 0.0014cm.

There are three basic methods of detecting small temperature rises. These are

1. Thermocouples
2. Platinum resistance thermometers
3. Thermistors

Sensitivities of the order of 50μV per ^{o}C can be obtained from a thermocouple, and so to detect a temperature change of $10^{-5o}C$, 500μμV would have to be measured. This method is unsuitable due to the difficulty of amplifying such small voltages. This sensitivity can be increased by using a thermopile, but then heat losses due to lead conduction increase at an equal rate and constructional difficulties arise.

Platinum resistance thermometers have a temperature coefficient of resistance of 0.4% per ^{o}C. However thermistors are a factor of ten better than this, and can be used in a sensitive a.c. bridge system with the consequent use of impedance matching, a.c. amplification and phase sensitive detection. Thermistors were therefore used, and these were type U 14 US bead thermistors manufactured by Stantel, with lead wires 0.025 mm in diameter.

The construction of the absorber is shown in figure 4. The bead thermistors are sandwiched between the foils, and the foils secured with a small amount of 'Araldite'. The assembly is suspended by fine nylon threads from a brass ring as shown in figure 5. The nylon threads are 0.1mm in diameter, and again heat conduction losses are minimised by using these. Connections are made to the thermistors and heater through nylon insulators embedded in the brass ring.

2.4 Heat losses in the calorimeter

The purpose of the calorimeter is to reduce heat transfer between the absorber and its surroundings. Heat losses are:-

2.4.1 Convection

Dove and Cole (9) state that air convection does not occur when $R < 1620$, where R is Rayleigh's number, given by

$R = a\, d^3 \delta\Theta$ for parallel plates,

d is separation of plates,

$\delta\Theta$ is temperature difference between plates, and

a is convection modulus for air.

a is proportional to the density squared. This shows that convection does not take place between parallel plates 1cm apart separated by air at atmospheric pressure, provided the temperature difference is less than $16.2^{\circ}C$. Convection heat losses are therefore not a problem in calorimetry due to the small temperature differences involved.

2.4.2 Lead conduction

The heat conducted away from the absorber by the leads is

$$Q = kA \frac{d\Theta}{dx} \text{ watts}.$$

k is the thermal conductivity

A is cross-sectional-area of the leads

$\frac{d\Theta}{dx}$ is the temperature gradient along a lead

Thus Q is kept small by using leads of small diameter and low thermal conductivity. An estimation of the heat lost through the leads is given in Table 2.

Table 2

Leads	Number of Leads (length = 1cm)	Thermal Conductivity Watts/cm-°C	Diameter (cm)	Total Heat Lost μW/°C
Heater wires (Evanohm)	2	0.152	0.0014	0.54
Thermistor wires (Platinum)	2	0.70	0.0025	6.86
Supporting threads (Nylon)	4	0.002	0.010	0.64

Total heat lost along lead connections $\sim 8\mu W$ per °C

2.4.3 Air conduction

It can readily be shown that the thermal conductivity of air remains constant with decreasing pressure until the mean free path of the air molecules exceeds the dimensions of the enclosure in question.

The mean free path L is given by

$$L = \frac{1}{2^{\frac{1}{2}} n \pi \sigma^2}$$

where n = number of molecules per cc.

σ = molecular diameter.

The number of molecules per cc of air is given by

$$n = \frac{6.02 \times 10^{23} \times 0.001293 \times P}{28.8 \times 76}$$

at any pressure P (in cms of Hg)

and $\sigma = 3 \times 10^{-8}$ cm

Therefore $L \times P = 7 \times 10^{-4}$

If L = 1cm (that is equal to the dimensions of the chamber), then $P = 7 \times 10^{-3}$ mm Hg. So by reducing the air pressure in the chamber below this value, heat losses due to conduction will be reduced.

Roberts (27) states that the heat loss per unit area per second due to air conduction at low pressures is given by

$$Q = \frac{1}{4J} \frac{\gamma + 1}{\gamma - 1} \sqrt{\frac{2R}{\pi M}} pa \frac{T_2 - T_1}{\sqrt{T_1}} \text{ cals.cm}^{-2}\text{sec}^{-1}$$

where J is the mechanical equivalent of heat in ergs per cal.

γ is the ratio of the specific heats of air.

R is the gas constant in ergs per degree.

M is the molecular weight.

P is the pressure in dynes per cm^2.

a is the accommodation coefficient of air.

T_2 is temperature of the body (= molecular temperature as they leave the surface of the body).

T_1 is the molecular temperature before striking the surface of the body.

A diffusion pump is used to evacuate the calorimeter and the pressure inside the calorimeter as estimated by a Penning gauge is 5×10^{-6} mm Hg. Taking this value for P, a = 0.75 (28) and $T_2 - T_1 = 1^{\circ}C$, then

$$Q = 2.48 \mu\text{watts per } ^{\circ}C \text{ per } cm^2$$

The area of the absorber is 8 cm^2, therefore

$$Q = 19.8 \mu\text{watts per } ^{\circ}C$$

2.4.4 Radiation

Radiation heat loss Q (in watts) from a body is given by

$$Q = 5.67 \times 10^{-12} \times A \times e \times (\Theta^4 - \Theta_o^4)$$

where A = surface area of radiation body

e = emissivity of body

Θ_o = temperature of surroundings

Θ = temperature of body

$\Theta - \Theta_o = \delta\Theta$ and if this is small

$$\Theta^4 - \Theta_o^4 \simeq 4\,\Theta_o^3\,\delta\Theta$$

If $\delta\Theta = 1^oC$ then

$Q = 2.27 \times 10^{-11} \times A \times e \times \Theta_o^3$ watts per ^oC.

Radiation heat losses can be reduced by having a low emissivity for the radiating body. It is also essential that the surroundings have a low emissivity so that heat transfer to the absorber is minimised. As Q is proportional to Θ_o^3, radiation losses can be greatly reduced by working at a low temperature. At room temperature (20^oC), taking $e \simeq 0.05$ (29) for the total emissivity,

$$Q = 234\ \mu W \text{ per } ^oC$$

(c.f. liquid nitrogen temperature $Q = 3\ \mu W$ per ^oC)

At liquid nitrogen temperature radiation heat losses would be the same order of magnitude as conduction losses, however at room temperatures radiation losses are completely dominant.

Total heat loss = 234 + 20 + 8 = 262 μW per ^oC

Therefore at room temperature the thermal leakage constant L = 262 μW per ^oC.

2.5 Construction of calorimeter body

2.4.1 First calorimeter

For reasons given in Chapter 1, it was decided to use a constant temperature environment calorimeter. More complicated systems are required by adiabatic and isothermal calorimetry, and as operational space is limited,

Figure 6

DIAGRAM OF FIRST CALORIMETER

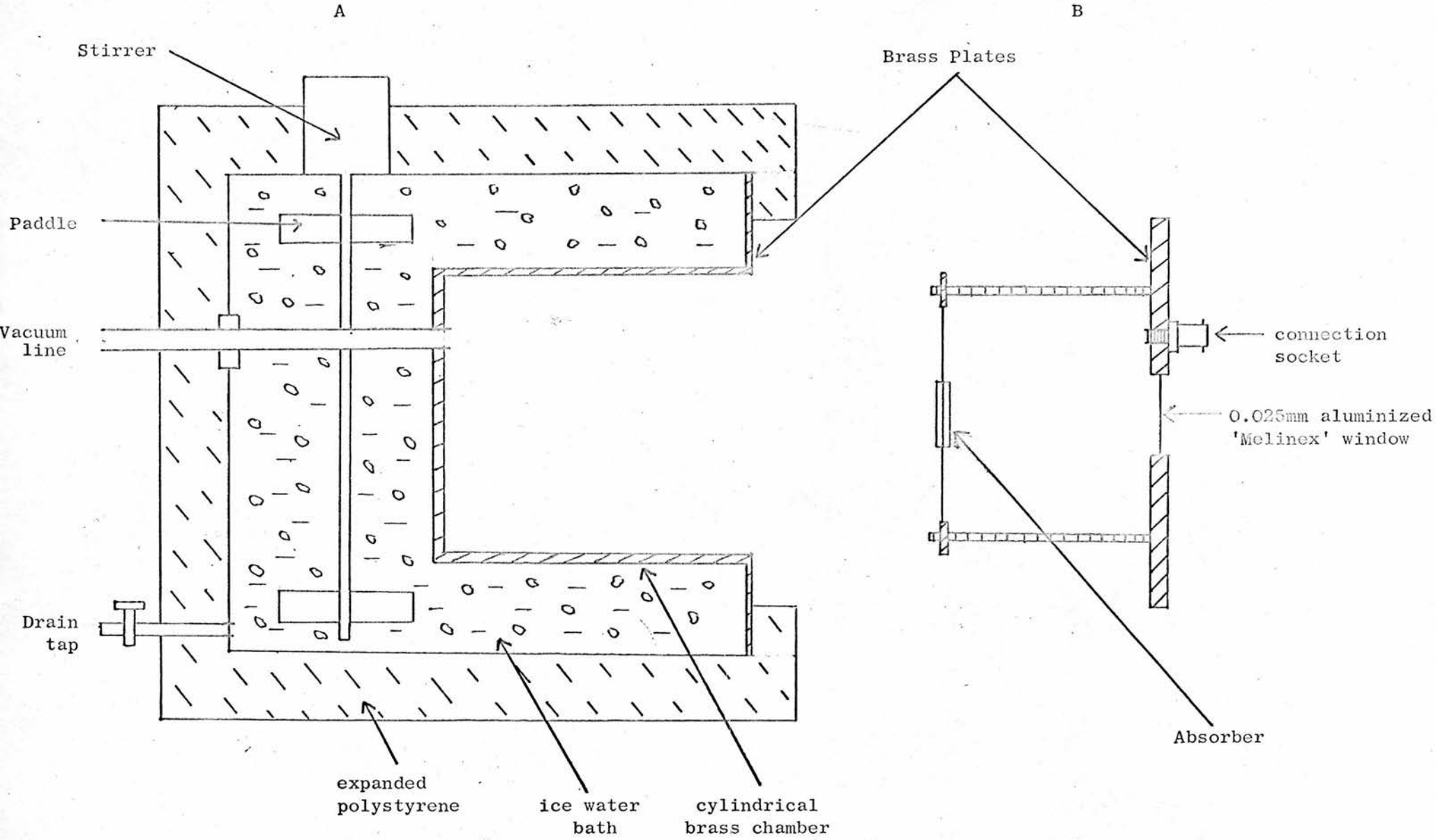

this is the obvious choice.

The efficient operation of a constant temperature environment calorimeter may rely upon a constant temperature thermal bath, or upon a large amount of thermal damping to form the calorimeter body. A successful constant temperature bath will provide better temperature control than thermal damping, and it was initially decided to use this. An ice-water bath (as used by Dove and Cole (9)), requires less volume, is cheaper to build, and again if successful should provide better temperature control than a thermostatically controlled water bath. The first calorimeter therefore employed an ice-water bath.

Figure 6(a) shows a cylindrical brass chamber, attached at the front end to a square brass plate, and with a vacuum connection provided at the rear end. This assembly was silver plated to reduce radiation heat loss and mounted in a perspex box. The constant temperature bath was made by allowing a crushed ice and water mixture to equilibriate at $0^{\circ}C$. The perspex box was filled with this mixture, and a stirrer, mounted on the lid of the box, constantly stirred the mixture. As the ice content diminished, excess water could be drained by a tap at the bottom of the box, and the content restored by adding ice-water mixture through the lid of the box.

Figure 6(b) shows the absorber assembly. The brass plate contained a 0.025 mm aluminized 'Melinex' window, sealed by a conventional 'O' ring, and the plate was itself 'O' ring sealed to the front of the calorimeter. The absorber was suspended from a brass ring in a manner similar to that described in 2.3, and this ring was supported by screwed brass rods from the front plates. Electrical connections were made through

this plate. The assembly was then bolted together and surrounded by expanded polystyrene.

Drift rates obtained with this calorimeter were rarely better than 10^{-3}°C per min, about two orders of magnitude more than required. The limitations seemed to be due to the geometry of the system rather than to the instability of the ice bath. The angle subtended by the front plate at the absorber was too great resulting in excessive radiation heat transfer. This could also occur directly with the absorber and could have been reduced by the interposition of radiation heat shields. Heat conduction could occur directly by means of the brass supporting rods.

The front plate relied too much on conduction to obtain a constant temperature, and appeared to be greatly subject to room temperature variations. So at once was seen the difficulty of providing a window with adequate temperature control. The only noted limitation of the ice bath was that it failed to remain at 0°C for a sufficiently long time (e.g. overnight), and this caused a problem in the fact that it took a considerable length of time for the calorimeter to equilibrate at 0°C even without evacuation. Neither could the calorimeter be described as portable, it was cumbersome and the ice-bath required a lot of attention. However this served its purpose in that it provided an excellent background for the design of a second calorimeter.

2.5.2 Second calorimeter

In this calorimeter it was decided, for simplicity, to use a large amount of thermal damping in an attempt to reduce room temperature variations, and to abandon the thermal bath. Twin absorbers were also employed, and although thermal matching is difficult with absorbers of such small physical size, a certain amount of matching can still be obtained.

Figure 7

SCHEMATIC DIAGRAM OF THE CALORIMETER

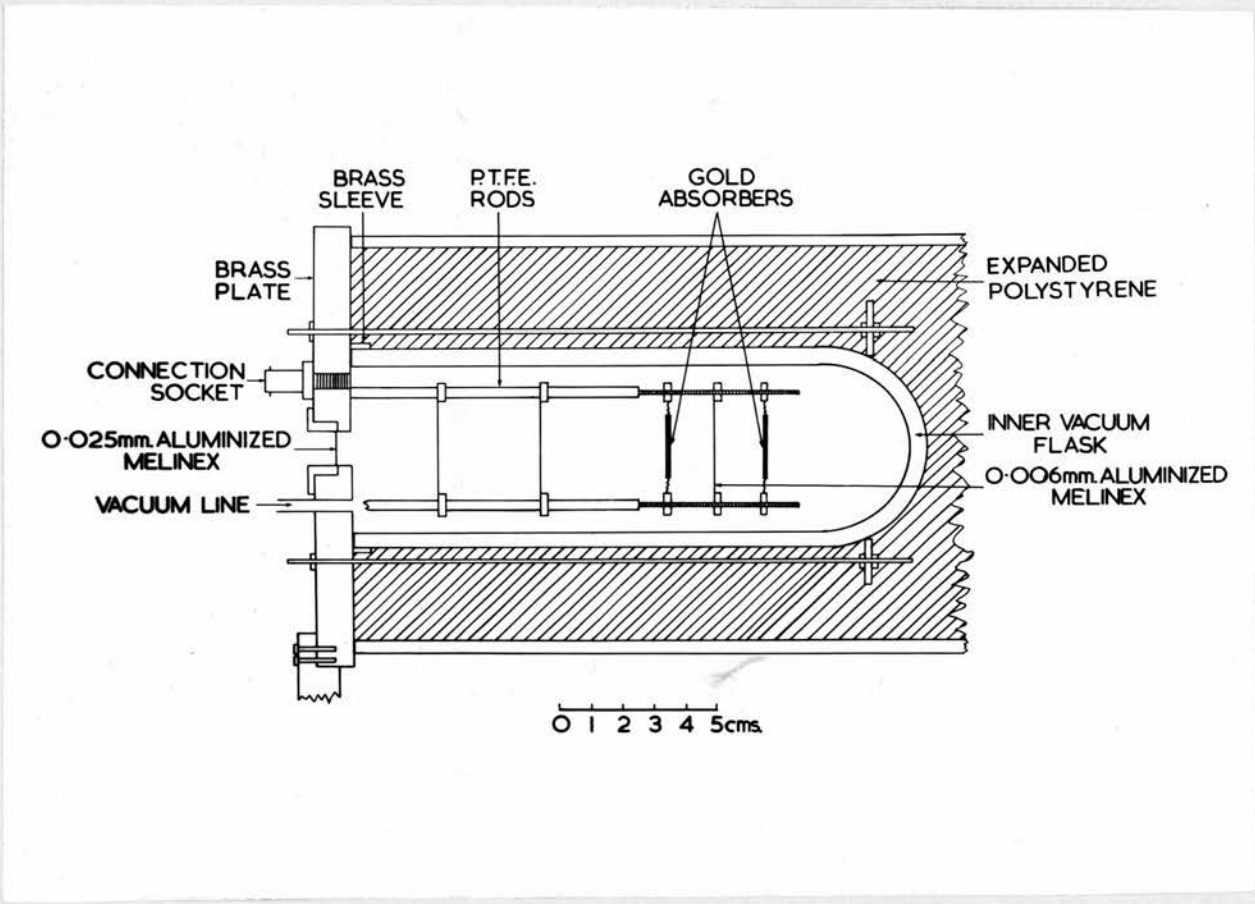

Working at room temperature will greatly increases radiation heat losses, but simplicity has been achieved, and a high developed to produce a high sensitivity calorimeter produced without such experimental complications.

The calorimeter is shown in figure 7. The dummy absorber contains only one thermistor and does not contain a heating coil. It is suspended in a similar manner to the irradiated absorber, and both are enclosed in a vacuum flask. The vacuum flask is ideal for this purpose, radiation heat transfer is reduced by the silvered surface, and conduction transfer by the vacuum gap. This flask is vacuum sealed to a brass plate by means of a neoprene washer, and is itself evacuated. The X-rays enter through a 0.025mm aluminized 'Melinex' window, which is again vacuum sealed by a neoprene washer. The dummy absorber is suspended behind the irradiated absorber; the absorbers are separated from each other and from the window by 0.006mm aluminized 'Melinex' heat shields. Conduction heat transfer from the front plate is reduced by using P.T.F.E. rods for suspension. Electrical and vacuum connections are made through the front plate, and the whole assembly is then enclosed in expanded polystyrene.

2.6 Experimental situation

The X-ray tube used is a Machlett type OEG-50-A, with a beryllium window 1mm in thickness and a focal spot 1.5mm square. The target is made of special high purity tungsten. The kilovoltage is continuously variable from 0 to 50kV and the milliamperage from 0 to 30mA with the condition that the maximum power dissipation is 800 watts. The H.T. output is stabilised within plus or minus 50 volts over a period not exceeding 4 hours at full load,

Figure 8

OPTICAL BENCH WITH CALORIMETER IN POSITION

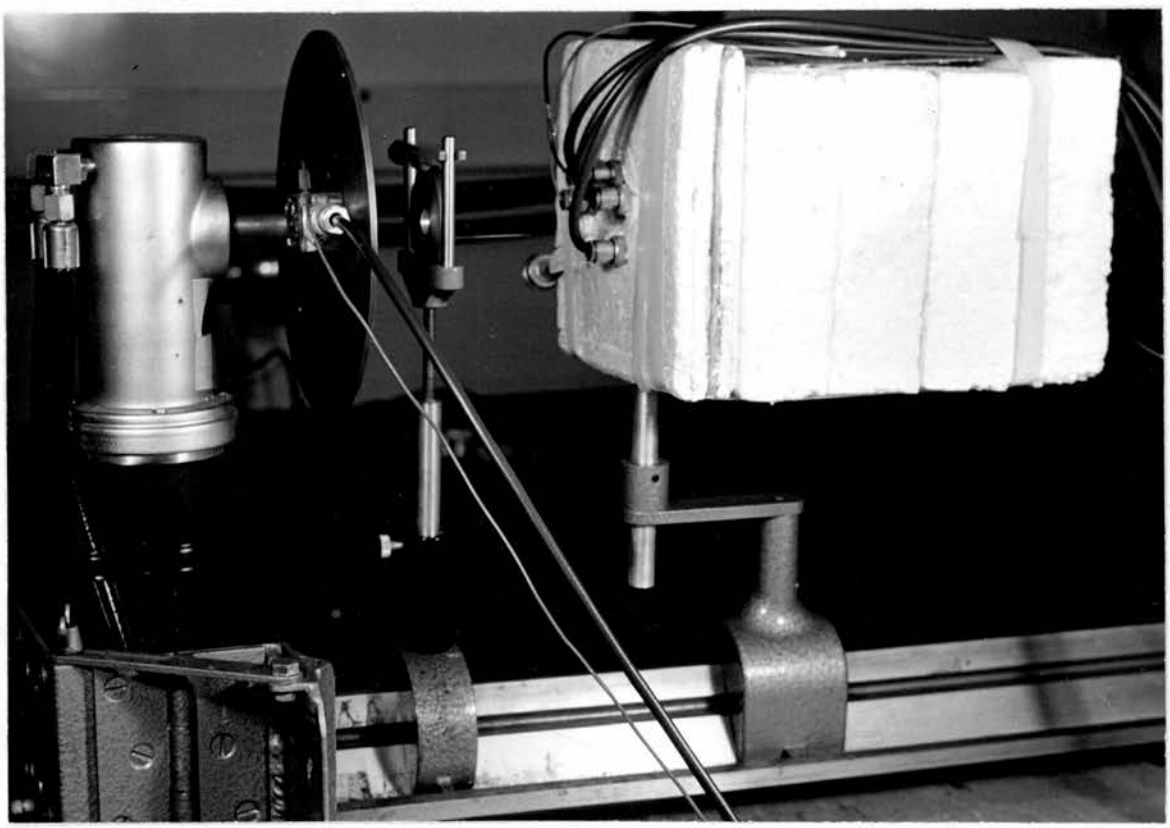

Figure 9

APERTURE FOR DEFINING X-RAY BEAM

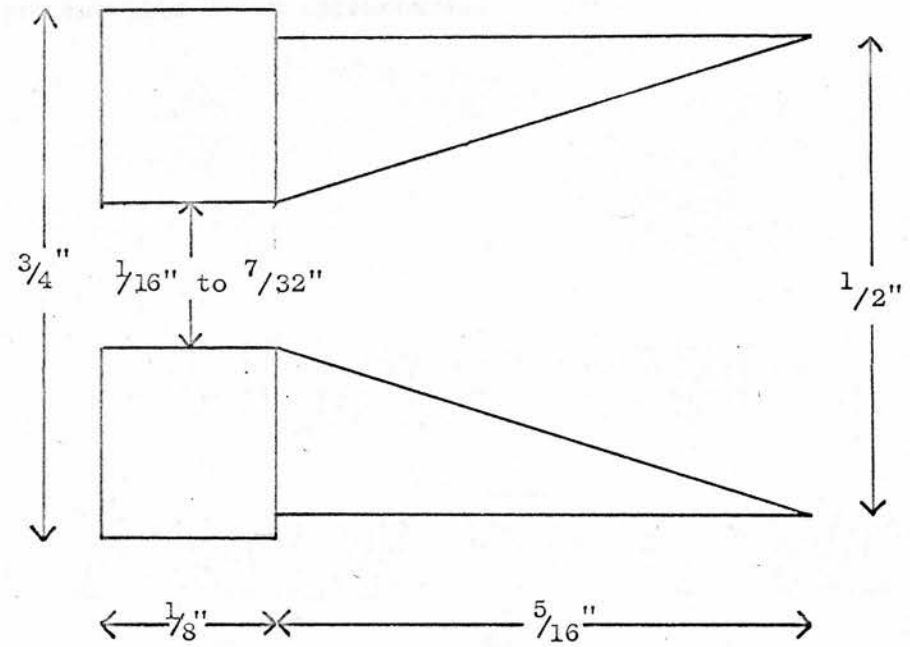

Figure 10

LINING-UP OF CALORIMETER

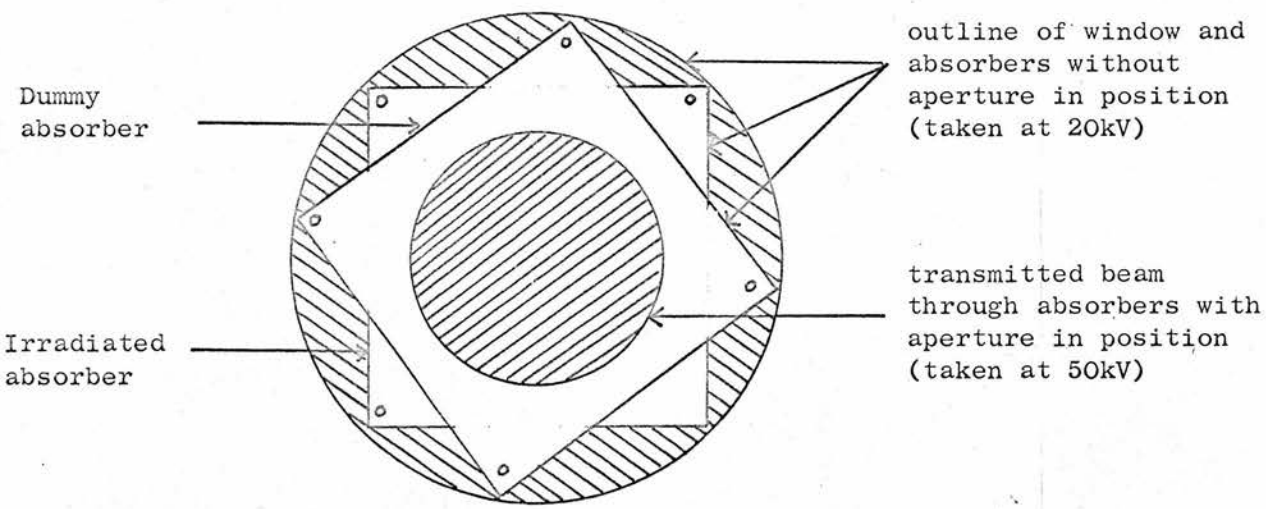

Diagram of photograph obtained at rear of absorbers without vacuum flask in position

and the H.T. ripple is quoted as 0.07kV per mA. Kilovoltage measurement is made on a variable scale 'Scalamp' galvanometer which measures the current through a high resistance leak across the X-ray tube. This provides two ranges:-

1. 0 - 10kV, sensitivity 1mm = 0.1kV, f.s.d. = 100mm.
2. 0 - 50kV, sensitivity 1mm = 0.5kV, f.s.d. = 100mm.

Although the reproducibility of a kilovoltage setting is better than $\pm$ 1%, absolute measurement as quoted by the manufacturers is only within $\pm$ 5%. However, the indicated kilovoltage has been checked by the Greening method (73) and found to be accurate to $\pm$ 0.5kV.

The X-ray tube is attached to an optical bench which lies parallel to and beneath the primary X-ray beam. The calorimeter is mounted on this bench as shown in figure 8, and is positioned by means of a pointer at a known position on the bench. This pointer touches a marked point on the front of the calorimeter. Similar points are marked on all other dosimeters, and they are so designed that in each case the distance from the front face to the window is constant. This ensures that all dosimeters are in the same geometrical position with respect to the X-ray beam, and that a similar amount of air attenuation occurs in each case. The X-ray beam to be measured is then defined by a brass aperture (figure 9), held in a stand at a known position on the bench. Positional errors will be mainly due to inverse square law, and it is more accurate to position the aperture in this manner than if it were situated in the window of the calorimeter.

The calorimeter is also positioned by removing the vacuum flask and a photograph taken behind the absorbers. The result is shown in figure 10.

An exposure made without an aperture in position and at 20kV, gives an outline of the absorbers in a circle formed by the calorimeter window, a second exposure with an aperture in position and at 50kV, gives a circle due to transmission through the absorbers. This circle is central on the absorbers when the calorimeter is correctly aligned. This has been checked by determining the calorimeter response to apertures of different areas (Appendix 1.1).

Figure 11

DIAGRAM OF CONVENTIONAL WHEATSTONE BRIDGE

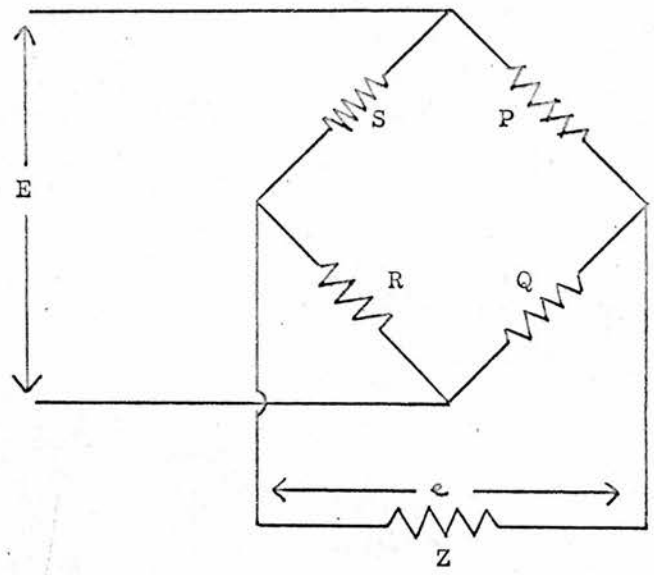

Figure 12

EQUIVALENT CIRCUIT OF MATCHED WHEATSTONE BRIDGE

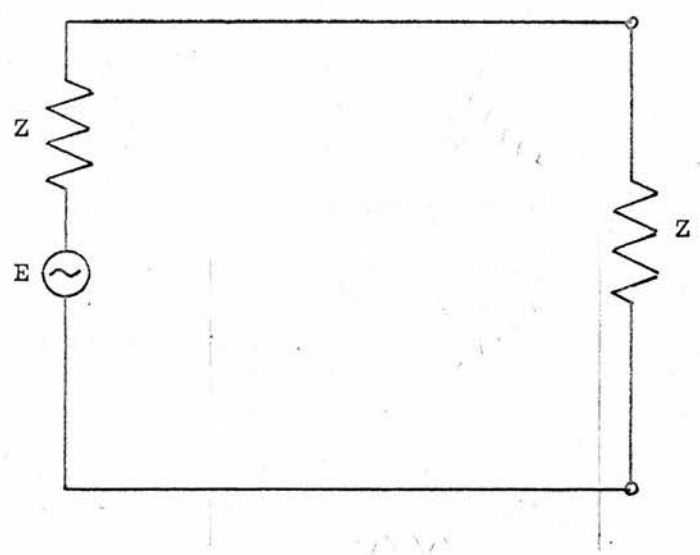

CHAPTER 3

TEMPERATURE MEASURING CIRCUIT

3.1 Sensitivity of a Wheatstone Bridge

3.1.1 Introduction

The conventional method of measuring a resistance is to use a Wheatstone bridge. Conditions for optimum operation of this system have long been sought after, but no universally accepted theory has been developed. In this section it is hoped that some of the difficulties involved in computing such a theory may be clarified, and that some optimum conditions may be found.

3.1.2 Voltage sensitivity

Figure 11 represents a simple Wheatstone bridge. E is the applied voltage; P, Q and R are the resistances in three arms of the bridge, and S is the variable thermistor resistance. The input resistance of the detector is $\mathcal{Z}$. One point which can immediately be stated is that, in as far as signal detection is concerned, it is impossible to do better than to match the output resistance of the bridge to the input resistance of the detector.

$$\text{Thus} \quad \mathcal{Z} = \frac{SR}{S + R} + \frac{PQ}{P + Q} \qquad \ldots\ldots\ldots 3 - 1$$

and by the use of Thevenin's theorem, the circuit can be represented as shown in figure 12. The out of balance voltage across $\mathcal{Z}$ is then a half of that obtained with infinite detector resistance, and given by

$$e = \frac{1}{2} \times \left(\frac{Q}{P + Q} - \frac{R}{R + S} \right) \times E \qquad \ldots\ldots\ldots 3 - 2$$

A small change δS in S will produce a small change δe in e given by

$$\delta e = \frac{E}{2} \times \frac{R}{(R + S)^2} \times \delta S \qquad \ldots\ldots\ldots 3 - 3$$

The equation describing the behaviour of the thermistor is

$$S = S_o \exp \left(\frac{B}{\Theta} - \frac{B}{\Theta_o} \right) \qquad \ldots\ldots\ldots 3 - 4$$

where B is a constant for the thermistor (in degrees absolute)

S is the resistance at Θ (degrees absolute)

S_o is the resistance at Θ_o (degrees absolute)

Differentiating 3-4 with respect to Θ gives the change in thermistor resistance δS for a change in temperature $\delta\Theta$

$$\delta S = - \frac{BS}{\Theta^2} \delta\Theta \qquad \ldots\ldots\ldots 3 - 5$$

and substituting for δS in 3 - 3 gives

$$\frac{\delta e}{\delta \Theta} = - \frac{BE}{2\Theta^2} \times \frac{RS}{(R + S)^2} \qquad \ldots\ldots\ldots 3 - 6$$

It seems at first logical to define the sensitivity in this way. The result gives $\frac{\delta e}{\delta \Theta} = f(S,R)$ where S and R are independent variables. Solving the simultaneous equations

$$\frac{\partial}{\partial S} \left(\frac{\delta e}{\delta \Theta} \right)_R = \frac{\partial}{\partial R} \left(\frac{\delta e}{\delta \Theta} \right)_S = 0$$

gives a maximum at S = R. No relationship is given between the values of S and R and the value of P and Q. This appears to be the limitation of the theory. The condition R = S is by no means critical.

3.1.3 Power sensitivity

In any measuring system power is detected, and as power matching has been used it is more correct to look for an optimum condition in the power sensitivity. The change in the power developed in the detector δP_D is given by

$$\delta P_D = \frac{(\delta e)^2}{\mathcal{Z}} \quad \ldots\ldots\ldots 3 - 7$$

Substituting equations 3 - 1 and 3 - 6 for $\mathcal{Z}$ and δe gives

$$\delta P_D = \frac{E^2}{4} \times \frac{B^2 \delta\theta^2}{\theta^4} \times \frac{R^2 S^2}{(R+S)^4} \times \left(\frac{RS}{R+S} + \frac{PQ}{P+Q}\right)^{-1} \quad \ldots\ldots\ldots 3 - 8$$

It can at once be seen that both P and Q have to be less than S and R in order to maximise δP_D. It is now required to maximise

$$\delta P_D = \frac{E^2}{4} \times \frac{B^2 \delta\theta^2}{\theta^4} \times \frac{RS}{(R+S)^3} \quad \ldots\ldots\ldots 3 - 9$$

This equation does not solve to give an optimum relationship between S and R. However, for a given value of the thermistor resistance S a maximum is obtained with S = 2R. These conditions have been used in this work. Once again this is not a complete analysis, and the obtained conditions are not critical. This is shown as follows:-

Sensitivity	S = 0.5R	S = R	S = 2R	S = 4R
$\frac{\delta e}{\delta\theta}$	88.9%	100%	88.9%	64%
δP_D	50%	84.4%	100%	86.4%

3.1.4 Thermal considerations

Obviously the sensitivity can be increased by increasing E, but a limit to this increase is set by variations inherent in E. An oscillator is used to supply the voltage to the bridge (3 - 2) and this is reported to be stable to $\pm$ 1dB. This means that a voltage variation of approximately $\pm$ 12% can be expected. The power developed in the thermistor is given by

$$P_T = \frac{E^2 S}{(R+S)^2} \quad \ldots\ldots\ldots 3 - 10$$

Thus P_T can vary by $\pm$ 24%, and any other variations will be small compared to this. If the limit $P_T = 0.1\ \mu W$ is set, then variations in this will be $\pm$ 0.025μW. Power measured with the calorimeter are at least a factor of 100 greater than this variation. E is thus adjusted to give $P_T = 0.1\mu W$.

A further problem now arises. Can a limit to E be set independently (as shown above), or should the sensitivity be normalised so as to become independent of E.

3.1.5 Normalisation of the sensitivity

The voltage drop across the thermistor V_T is given by

$$V_T = \frac{ES}{R + S} \qquad \ldots\ldots\ldots 3 - 11$$

and normalising equation 3 - 6 by equation 3 - 11 gives

$$\frac{1}{V_T}\ \frac{\delta e}{\delta \Theta} = -\frac{B}{2\Theta^2}\ \frac{R}{R + S}$$

which increases as $\frac{R}{S}$ increases. An identical result is obtained on normalising equation 3 - 9 by equation 3 - 10. However little information is obtained from this. An interesting result is obtained by looking for optimum conditions in $\frac{P_D}{P_T}$ using a substitution method suggested by Callendar in 1910. This is as follows:-

$$S = S \qquad R = \alpha Y \qquad P = \beta Y \qquad Q = \alpha\beta Y$$

where α and β are arbitary numbers, and S = Y at balance

$$\frac{P_D}{P_T} = \frac{E^2}{4} \times \left(\frac{Q}{P + Q} - \frac{R}{R + S} \right)^2 \times \left(\frac{PQ}{P + Q} + \frac{RS}{R + S} \right)^{-1} \times \frac{(R + S)^2}{E^2 S} \qquad \ldots\ldots 3 - 12$$

$$\frac{P_D}{P_T} = \frac{1}{4} \times \frac{(QS - RP)^2\ (R + S)}{S(P + Q)\left[PQ(R + S) + RS(P + Q)\right]} \qquad \ldots\ldots\ldots 3 - 13$$

Using the above substitution gives

$$\frac{P_D}{P_T} = \frac{1}{4} \times \frac{\alpha(S - Y)^2 (\alpha Y + S)}{SY(1 + \alpha)\left[\beta(\alpha Y + S) + S(1 + \alpha)\right]} \qquad \ldots\ldots\ldots 3 - 14$$

This approaches a maximum when $\beta \rightarrow 0$, that is R and S $\gg$ P and Q. It is now required to maximise

$$\frac{P_D}{P_T} = \frac{1}{4} \times \frac{(S - Y)^2}{S^2 Y} \times \frac{\alpha(\alpha Y + S)}{(1 + \alpha)^2} \qquad \ldots\ldots\ldots 3 - 15$$

There is now a maximum when $\alpha \rightarrow \infty$, that is R and Q $\gg$ P and S

Summarising R and S $\gg$ P and Q
R and Q $\gg$ P and S
} These conditions conflict as regards S and Q. optimum conditions are therefore given by $R > \begin{Bmatrix} S \\ Q \end{Bmatrix} > P$

Yet another set of operating conditions has been found. Thus it appears that the crux of the problem lies in the definition of the sensitivity. Two points amplify this statement.

1. When power detection is considered it is always found that the output resistance of the bridge is determined by S and R, that is P and Q are small compared to S and R.
2. Any normalisation by the power developed in the thermistor results in the condition R > S. This implies that for a given E, the power dissipation in the thermistor should be minimised for maximum sensitivity. This is not sensible, and it is therefore suggested that a limit to E can be set independently.

As stated, the conditions as found in 3.1.3 have been used, but it is by no means certain that these are correct. However as the obtained conditions are not critical, it is unlikely that any great loss in sensitivity may have been suffered.

3.2 Measuring Circuit

There are three basic modes of operation of a Wheatstone Bridge

1. D.C. operation, current detection
2. D.C. operation, voltage detection
3. A.C. operation

The first method was used by Kruglov and Lopatin (7). They employed a galvanometer with a sensitivity of 10^{-10} amps per mm, but no amplification or recording of the signal was used and galvanometer deflections were recorded manually. An electronic galvanometer was used by Radak and Markovic (14), but again no mention of a recording system was made. Keene and Law (16) used a galvanometer amplifier employing photocells; such systems are noted for their susceptibility to electrical drift, but the authors did not seem to be troubled by this.

Certain systems have been used employing equal bridge resistances and a high impedance voltage detector is then used. Gomberg et al. (10) used such a configuration with a microvoltmeter as a detector. D.C. amplifiers have been used by Milvy et al. (30) and by Laughlin et al. (6). The d.c. out of balance voltage is chopped to produce an a.c. voltage, and a.c. amplification followed by rectification is then used. Such amplifiers are not reported to be as stable as direct a.c. amplifiers. Laughlin used power matching between bridge and amplifier, but did not consider the structure of the bridge.

A.C. systems have not been widely used. Bewley (17) employed a low frequency (20 c/s) system. The out of balance wasamplified, filtered, synchronously rectified and displayed on a recorder. Bridge

Figure 13

TEMPERATURE MEASURING CIRCUIT

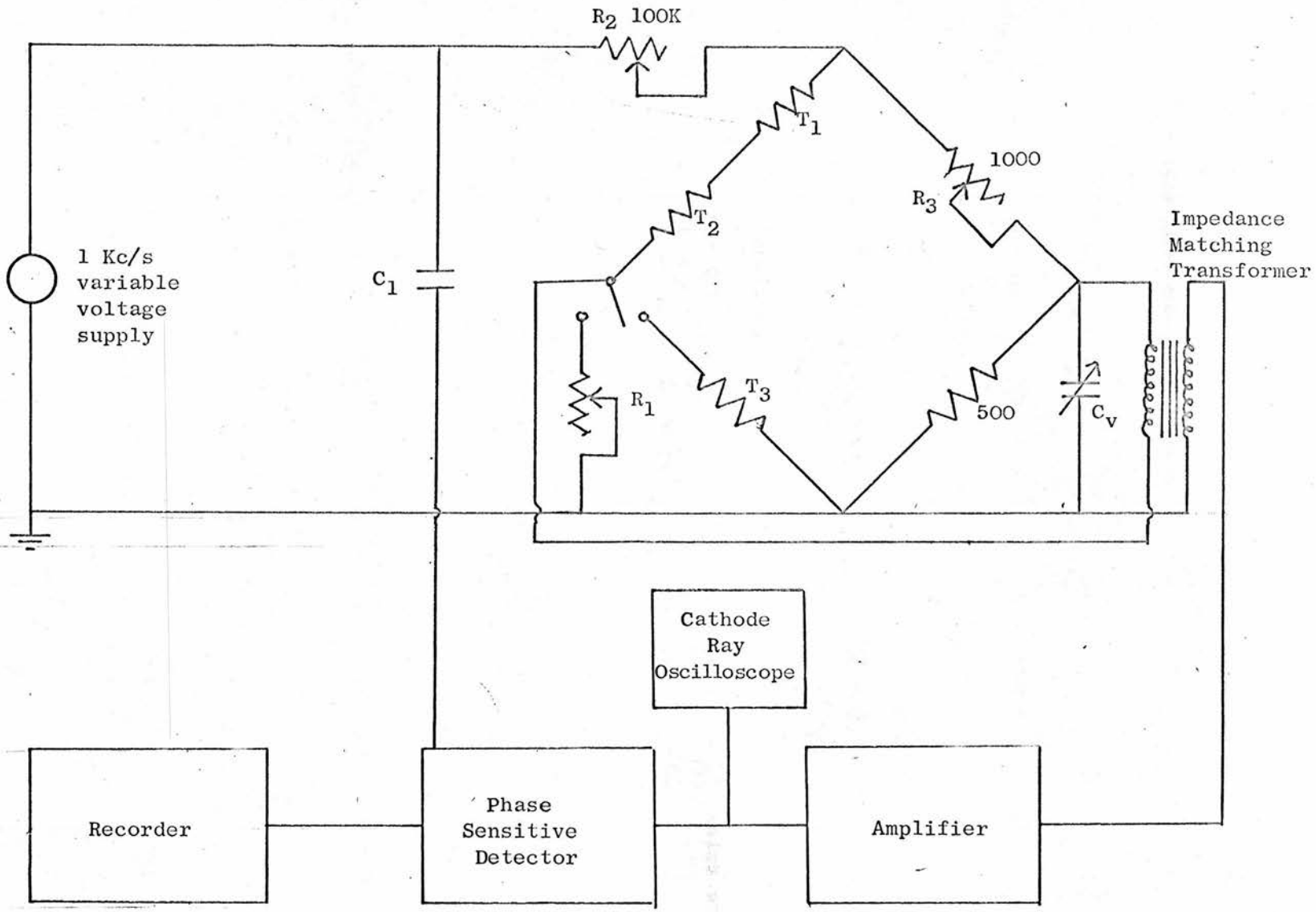

Thermistors T_1, T_2, T_3 nominally 10KΩ at room temperature

resistances were all equal and power matching was not considered.

No noted analysis of the Wheatstone network has been carried out in the literature on calorimetry. Genna and Laughlin (28) give a summary of various conditions that have been used. Beakley (31), in a paper on the design of thermistor thermometers with linear calibration, has considered the sensitivity of the circuit in terms of current change per unit temperature change. Mitvalsky (32), has pursued similar work. He produced a rather complicated analysis for an unbalanced Wheatstone bridge, and linked his results to those of Heaviside in 1873.

The electrical circuit used for measuring temperature changes inside the calorimeter is shown in figure 13. As the ratio of the arms in the bridge is 2:1, it is necessary to have two thermistors in one arm of the bridge. T_1 and T_2 are the thermistors in the irradiated absorber and T_3 is the thermistor in the dummy absorber. These are situated in opposing arms of the bridge, and all are nominally 10kΩ at room temperature. The other two arms have to be small in resistance compared to the thermistors, and are 1000Ω and 500Ω. The 1000Ω is variable in steps of 0.001Ω.

The out of balance signal from the bridge is amplified, and the output impedance of the bridge is matched to the input impedance of the amplifier by a transformer. The output impedance of the bridge as given by equation 3 - 1 is 7kΩ, and this has to be matched to 300kΩ. The primary to secondary turns ratio of the transformer required must therefore be $\sqrt{\frac{300}{7}}$:1, or 6.5:1.

The circuit is a conventional a.c. bridge. A.C. was preferred to d.c. because greater sensitivity is obtained through the impedance matching of detectors. Furthermore a.c. voltages are easier to amplify, and a better signal to noise ratio can be obtained by the use of a phase sensitive

Figure 14

PRINCIPAL OF OPERATION OF PHASE SENSITIVE DETECTOR

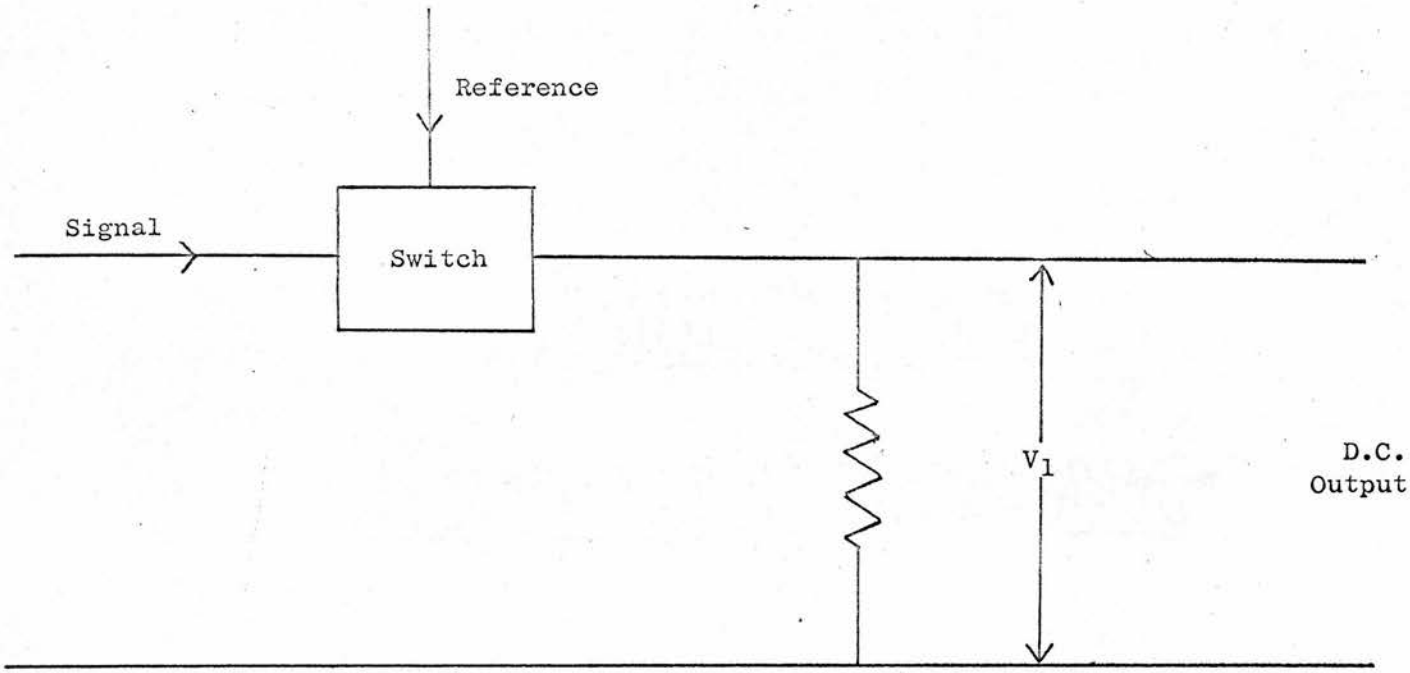

detector. The voltage supplied to the bridge, and hence the power developed in the thermistors, can be varied by the resistance R_2. The frequency of the voltage was optimised at approximately 1kcps. Higher frequencies lead to a shunting effect by the various capacitances in the circuit, while lower frequencies give rise to a large amount of flicker noise. C_v consists of a decade capacitance box and a 1000pF air spaced variable in parallel, and a balance position is obtained by varying C_v and R_s. The switch enables the thermistor T_3 to be replaced by a variable resistance R_1 so that the combined resistance of T_1 and T_2 can be measured. All electrical connections in the system are made with low noise coaxial cable.

The amplifier (LA 365) is manufactured by Brookdeal Electronics and has been developed for use in conjunction with the Brookdeal phase sensitive detector (PD 629). It has low hum and noise levels and there is no phase shift for amplification between 10 cps and 10 kcps. The voltage amplification is performed by three ECC 83 double triodes connected in cascade to give a six stage amplifier with a variable gain from 20 dB to 95 dB.

An essential requirement for the efficient operation of the phase sensitive detector is that the reference and signal voltages are in phase. The reference voltage is taken straight from the oscillator and the phase is altered to that of the signal voltage by means of the capacitor C_1 in conjunction with the input impedance of the phase sensitive detector.

The phase sensitive detector acts on the principle of the synchronous switch as shown in figure 14. The signal and reference voltages are periodically switched into a lead resistor, the frequency and phase of the switching determined by the reference voltage. The switch acts as a half-wave rectifier for signals of the same phase and frequency as the

Figure 15

ELECTRICAL CALIBRATION CIRCUIT

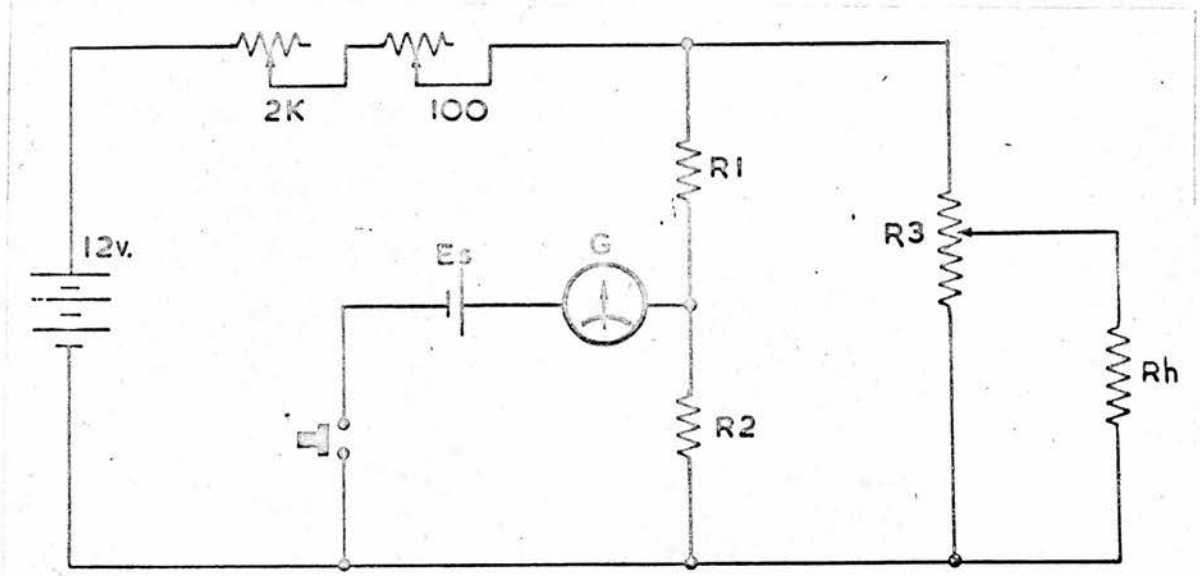

Es – WESTON STANDARD CELL 1·018v.
R1 – 8·981K ± 0·1%
R2 – 1·018K ± 0·1%
R3 – 10K DECADE BOX ±0·1%
Rh – HEATER RESISTANCE
G — GALVANOMETER

Figure 16

ELECTRICAL CALIBRATION CIRCUIT IN OPERATION

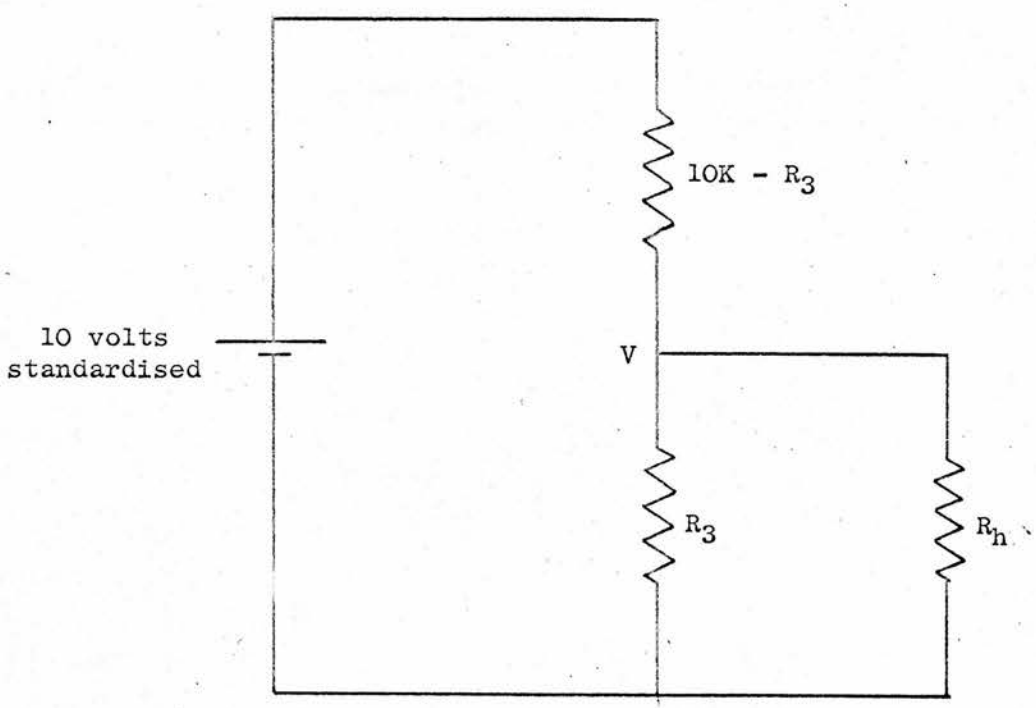

reference. When the signals are in phase half-wave rectification is achieved, and when in quadrature there is no rectification. When they are out of phase the d.c. output is proportional to $V_s \cos \alpha$. The phase-sensitive detector uses a balanced switching circuit, two way switch, two load resistors and hence provides full wave rectification. Noise voltages appear as a.c. voltages across the load resistor and so the response of the system to noise depends on the time constant T of the d.c. measuring device. So the phase sensitive detector acts as a rectifier of bandwidth $\frac{1}{T}$ and enables signals to be picked up from within noise.

The d.c. measuring device used is a Servoscribe potentiometric recorder, with a variable full scale deflection from 20 volts to 800 μvolts. The phase sensitive detector provides a balanced output about earth, so the time constant of the recorder can be increased by connecting capacitors across this output. An oscilloscope is used to look at the signal after it has been amplified. This provides a visual means of balancing the bridge, enables a check to be kept on the hum level in the system, and provides a means of ensuring that the reference and signal voltages are in phase. Since this system has been built and successfully operated it has been noted that a similar system has been described by Quigg (33) for use in calorimetry.

3.3 Electrical calibration circuit

The electrical calibration circuit shown in figure 15 is a simple potentiometer. By adjusting the 2kΩ and 100Ω variable resistors until no current flows through the galvonometer G , ten volts is standardised across the series resistance of R_1 and R_2 and hence across R_3. A voltage can then be tapped from R_3 across the heater resistance R_h, and the voltage across R_3 must be standardised after this tap has been made. The circuit

can then be represented as in figure 16.

The voltage V is given by

$$V = \frac{10\, R_3 // R_h}{(10^4 - R_3) + R_3 // R_h} \quad \text{volts}$$

$$V = \frac{10\, R_3 R_h}{10^4 (R_3 + R_h) - R_3^2} \quad \text{volts}$$

The power W developed in the coil is given by

$$W = \frac{V^2}{R_h} \quad \text{watts}$$

$$W = \frac{R_3^2 R_h^2 \times 10^8}{R_h \left[10^4 (R_3 + R_h) - R_3^2 \right]^2} \quad \mu \text{ watts}$$

$$W = \frac{R_h}{\left[1 + \frac{R_h}{R_3} - \frac{R_3}{10^4} \right]^2} \quad \mu \text{ watts}$$

Hence W can be evaluated for various values of R_h and R_3.

The resistance of the heating coil was measured by using a conventional Wheatstone bridge and found to be $39,830 \pm 2\Omega$. A correction was made for approximately 3cm of wire which lay between the absorber and the supporting brass annulus, and R_h in the above equation taken as $39,700 \pm 100\Omega$ (i.e. $\pm$ 0.25%).

Figure 17

30 KVp X-RAY SPECTRUM

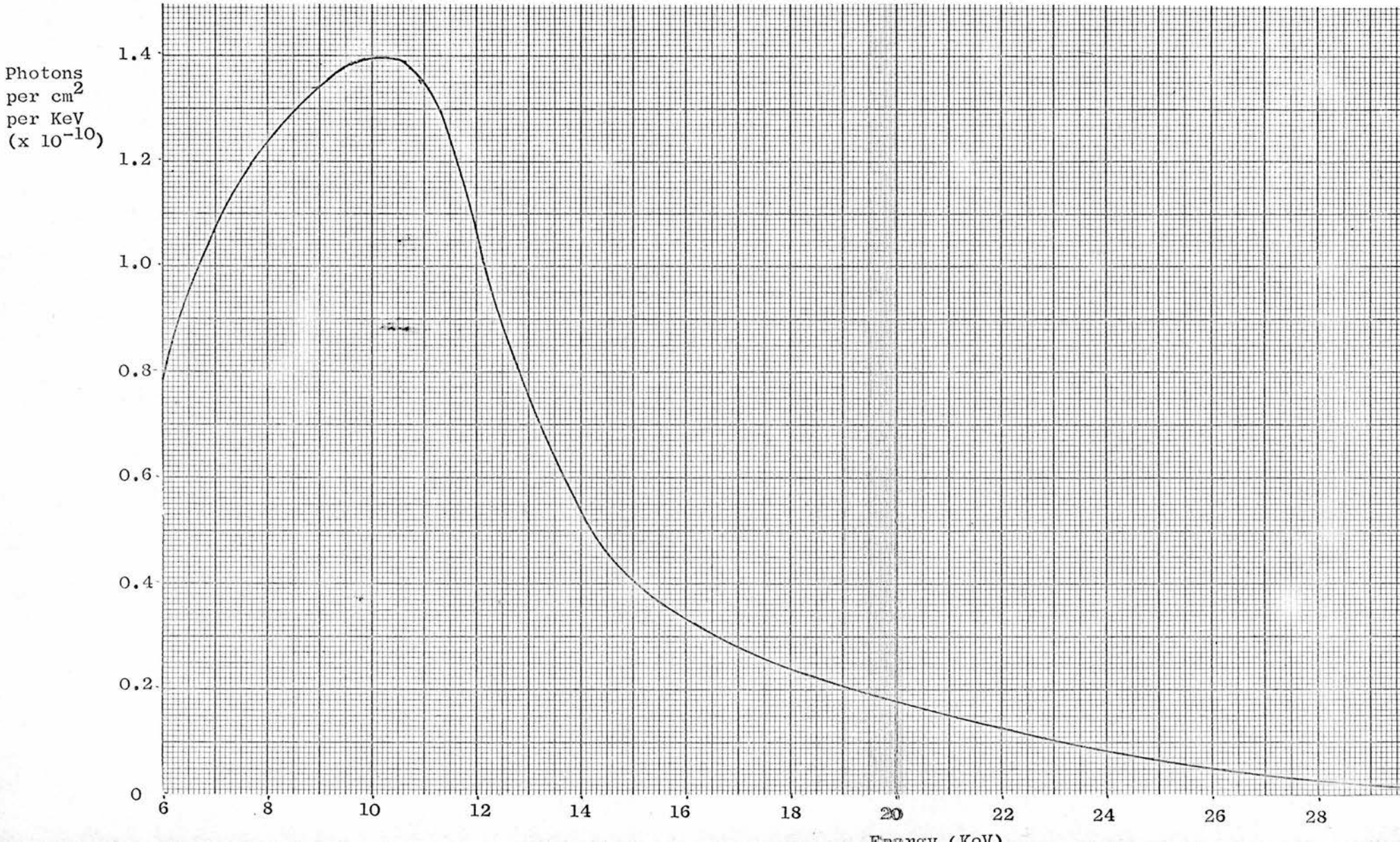

CHAPTER 4

PERFORMANCE OF CALORIMETER

4.1 Total absorption calculations

In any measurements made with the calorimeter it is essential that total absorption is achieved. This is readily calculated for a monochromatic beam of X-rays but not so easily calculated for a heterogenous beam. Total absorption must, in the first instance be defined, and in this work 99.9% absorption will be considered as total absorption. It is essential that the minimum thickness of absorber, consistent with total absorption, is used, so that sensitivity may be maximised.

A typical 30kV spectrum (34) from the tube is shown in figure 17. Let the X-ray spectrum be divided up into n energy intervals dE, with mean energies E_1, E_2, ... E_r .....E_n. In each energy interval dE there are $g_r(E)$ photons per cm^2 per keV at a mean energy E_r. Hence the total energy per cm^2 in the beam is

$$\sum_{E_r = E_1}^{E_n} E_r \; g_r(E)$$

If the above spectrum is incident upon an absorber of thickness t, then

$$\frac{I_t}{I_o} = \frac{\sum_{E_r = E_1}^{E_n} E_r \; g_r(E) \exp\left[- \mu(E_r)t \right]}{\sum_{E_r = E_1}^{E_n} E_r \; g_r(E)}$$

where I_o is the incident intensity

and I_t is the transmitted intensity.

Figure 18

THE VARIATION OF $\frac{\mu}{\rho}$ WITH ENERGY FOR GOLD

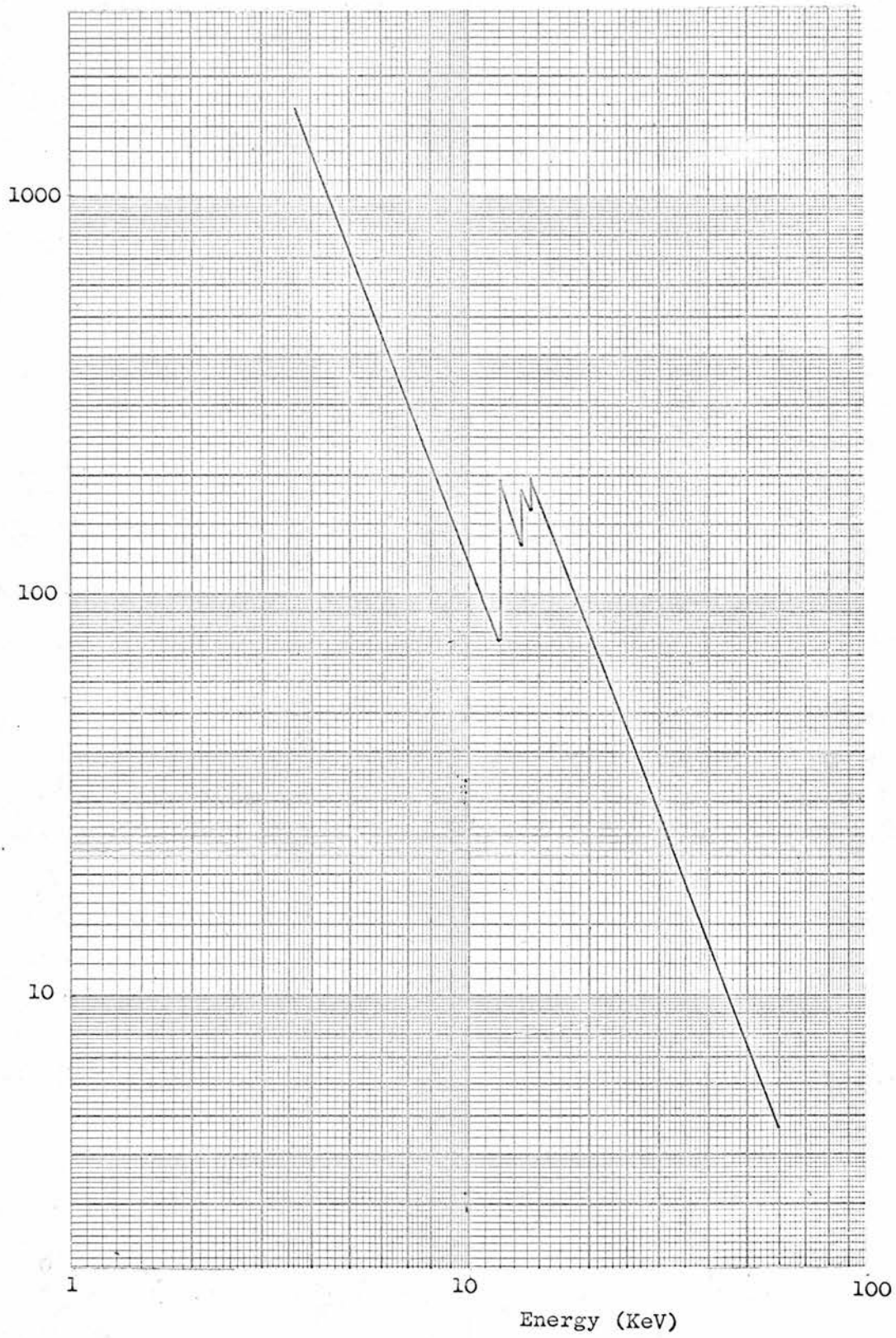

Gold is used as the absorbing element, and figure 18 shows the variation of $\frac{\mu}{\rho}$ with energy for gold (35). The spectrum is divided into 2keV energy intervals and

$$\sum_{E_r = E_1}^{E_n} E_r \; g_r(E) \exp\left[-\mu(E_r)t\right]$$

is evaluated as shown in Table 3.

Table 3

1	2	3	4	5	6
Mean Energy (keV) E_r	Photons per cm^2 per keV $g_r(E)$	Energy per cm^2 $2E_r\, g_r(E)$	Fractional energy per 2 keV interval δE	$\frac{\mu}{\rho}$ gold	$\delta E \times \exp(-\frac{\mu}{\rho})\rho t$
6	0.80×10^{10}	9.60×10^{10}	0.069	455	0.069 exp (- 8800t)
8	1.24	19.84	0.143	215	0.143 exp (- 4150t)
10	1.40	28.00	0.203	122	0.203 exp (- 2350t)
12	1.10	26.40	0.190	188	0.190 exp (- 3620t)
14	0.49	13.72	0.099	170	0.099 exp (- 3280t)
16	0.34	10.88	0.078	150	0.078 exp (- 2890t)
18	0.24	8.64	0.063	105	0.063 exp (- 2130t)
20	0.18	7.20	0.052	80	0.052 exp (- 1540t)
22	0.13	5.72	0.041	62	0.041 exp (- 1200t)
24	0.09	4.32	0.031	50	0.031 exp (- 965t)
26	0.05	2.60	0.019	41	0.019 exp (- 791t)
28	0.02	1.12	0.008	34	0.008 exp (- 656t)
30	0.01	0.60	0.004	28	0.004 exp (- 540t)

Assuming 99.9% absorption then $\frac{I_t}{I_o} = 0.001$, and as the sum of column 6 is $\frac{I_t}{I_o}$, then 0.069 exp (- 8800t) + 0.143 exp (- 4150t) + ...

+ 0.004 exp (- 540t) = 0.001

Figure 19

THE VARIATION OF $\frac{I_t}{I_o}$ WITH THICKNESS OF GOLD FOR 30KVp X-RAYS

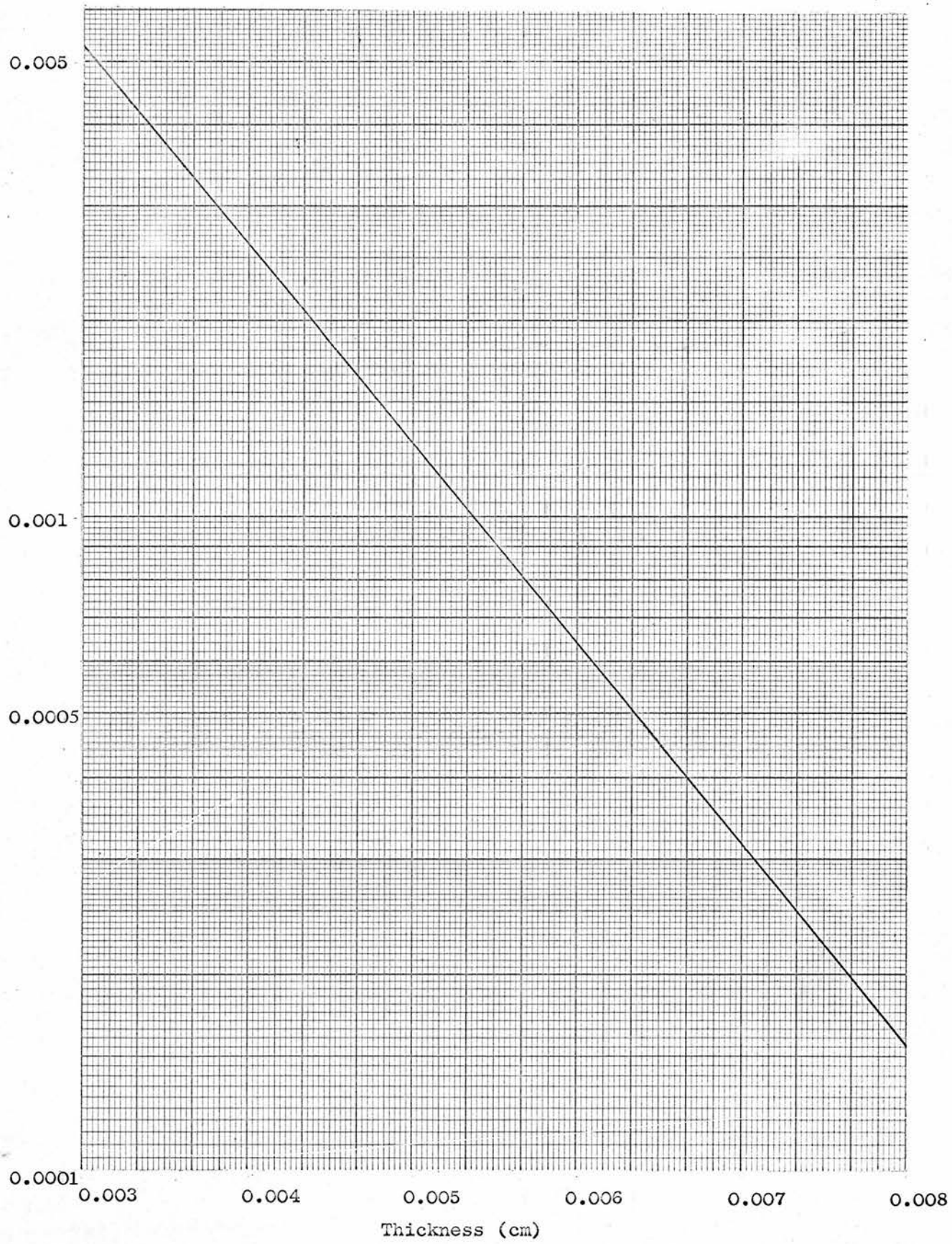

This equation cannot be directly solved, but by evaluating the left hand side for various values of t it can be solved by extrapolation. Results are shown in Table 4 and plotted in figure 19.

Table 4

Thickness (cm)	I_t/I_o
0.00381	0.00309
0.00508	0.00131
0.00635	0.000518
0.00762	0.000197

The thickness of gold used was 0.0075cm and this will stop 99.98% of 30kV X-rays. Thinner absorbers could be used for X-rays produced at lower voltages, but constructional difficulties are then encountered.

4.2 Required sensitivity

It is hoped to measure beams of 10kV to 30kV X-rays with the absorber and calorimeter already described. Assuming that the energy of the beam lies in the 1μW to 1mW input power range, then from equation 1 - 4

$$\frac{d\theta}{dt} = \frac{W}{k}$$

the expected temperature rise over a short period of time can be calculated. The temperature rise produced in the steady state can be evaluated from equation 1 - 6.

$$\theta\infty - \theta_o = \frac{W}{L}$$

and the results so obtained are shown in Table 5.

Figure 20

ESTIMATION OF TIME CONSTANT FROM COOLING CURVE

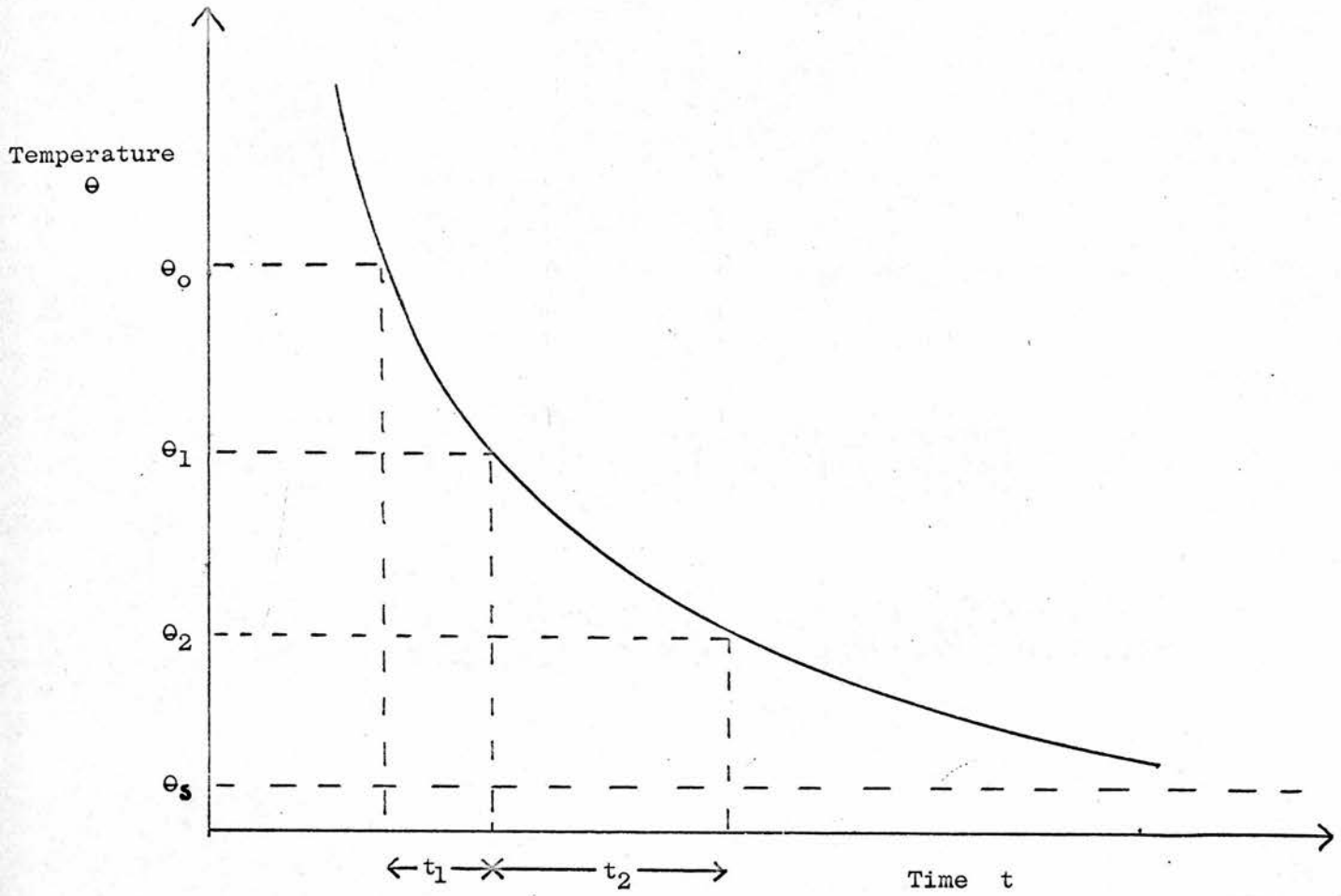

Table 5

Input power (watts)	Initial Slope $\frac{d\theta}{dt}$ (^{o}C/min.)	Steady State Temp. $\theta - \theta_o$ (^{o}C)
10^{-6}	9.54×10^{-4}	4.88×10^{-3}
10^{-5}	9.54×10^{-3}	4.88×10^{-2}
10^{-4}	9.54×10^{-2}	4.88×10^{-1}
10^{-3}	9.54×10^{-1}	4.88

In order to measure an input power of 1μW, a temperature change of 9.54×10^{-4}°C per min. would have to be measured. The background temperature drift rate should be small compared to this temperature change (i.e. about 1% or 10^{-5}°C per min.)

4.3 Estimation of time constant

The time constant of the system is given by $T = \frac{k}{L}$. k is 0.063 joules per °C (3-3), and L is 262μW per °C (2 - 4).

Therefore $$T = \frac{0.063}{262 \times 10^{-6}} \text{ secs}$$

$$T = 240 \text{ secs}$$

This means that in four minutes the temperature rise of the absorber, for any input power, will be 63% of the temperature rise achieved at equilibrium.

The time constant can also be determined experimentally. Figure 20 represents a typical cooling curve for the calorimeter, t_1 is time taken to cool from θ_o to θ_1 and t_2 the time to cool from θ_1 to θ_2 where

$$\theta_1 - \theta_s = \theta_o - \theta_s \exp\left(-\frac{t_1}{T}\right)$$

$$\text{and } \theta_2 - \theta_s = \theta_1 - \theta_s \exp\left(-\frac{t_2}{T}\right)$$

$$\text{Now } \exp\left(\frac{t_1}{T}\right) + \exp\left(-\frac{t_2}{T}\right)$$

$$= \frac{\theta_o - \theta_s}{\theta_1 - \theta_s} + \frac{\theta_2 - \theta_s}{\theta_1 - \theta_s}$$

$$= \frac{\theta_o + \theta_2 - 2\theta_s}{\theta_1 - \theta_s}$$

$$= 2$$

$$\text{Therefore } \left(1 + \frac{t_1}{T} + \frac{t_1^2}{2T^2}\right) + \left(1 - \frac{t_2}{T} + \frac{t_2^2}{2T^2}\right) = 2, \text{ if } \frac{t_1}{T}, \frac{t_2}{T} \ll 1$$

$$t_1 + \frac{t_1^2}{2T} = t_2 - \frac{t_2^2}{2T}$$

$$T = \frac{t_1^2 + t_2^2}{2(t_2 - t_1)}$$

Table 6 gives values of t_1 and t_2 taken from a typical cooling curve.

Table 6

t_1 (mins)	t_2 (mins)	$t_2 - t_1$ (mins)	$t_1^2 + t_2^2$ $(\text{mins})^2$	$T = \frac{t_1^2 + t_2^2}{2(t_2 - t_1)}$ (mins)
0.45	0.50	0.05	0.453	4.53
0.50	0.57	0.07	0.575	4.11
0.57	0.67	1.00	0.774	3.87
0.67	0.80	0.13	1.089	4.19
0.80	1.00	0.20	1.640	4.10
1.00	1.40	0.40	2.960	3.70
1.40	2.02	0.62	6.040	4.87

This gives an average value for T of 4.20 mins (= 252 secs) in excellent agreement with theoretical calculations.

Figure 21

ELECTRICAL ANALOGUE OF HEAT TRANSFER IN THE CALORIMETER

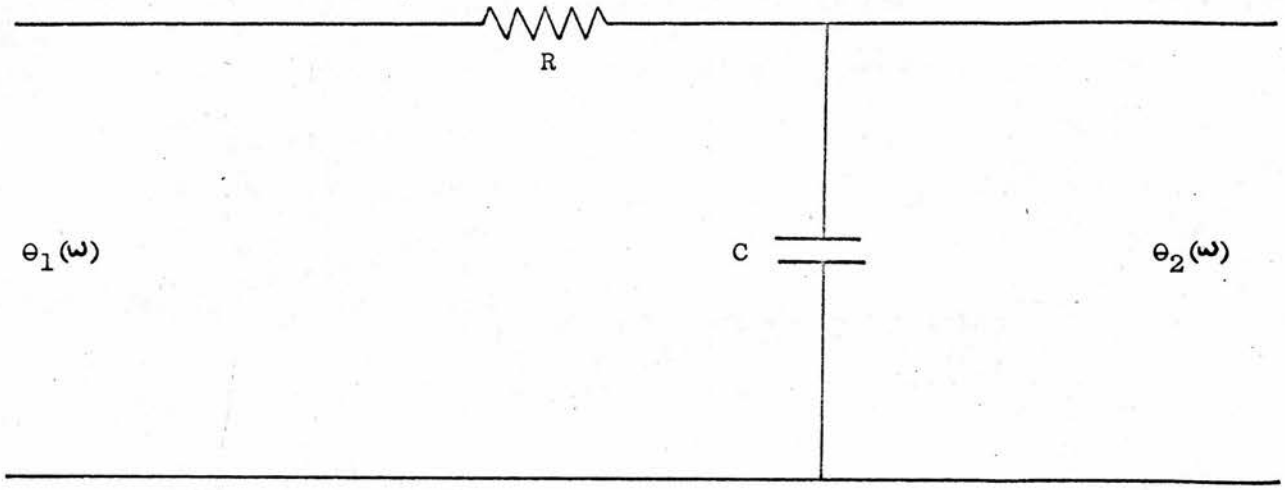

4.4 Effect of vacuum and twin absorbers

The equipment used to evacuate the calorimeter is a combined rotary and diffusion pump manufactured by Edwards High Vacuum Ltd. ("Speedivac"). The rotary pump is capable of producing a vacuum of 5×10^{-3} mm Hg, and the diffusion pump a vacuum of 5×10^{-6} mm Hg. This system stands beneath the table on which the calorimeter, optical bench and X-ray tube are mounted, and is connected to the calorimeter by means of a flexible pipe.

The thermal conductivity of air at atmospheric pressure is 3.5×10^{-4} watts per cm per ^{o}C. If, as in 2.4.3 the air conduction path is taken to be 1cm, then the heat lost Q from the absorber is given by

$$Q = kA \quad (A = 8 \text{ sq.cm.})$$

$$Q = 2.8 \times 10^{-3} \text{ watts per } ^{o}\text{C.}$$

A comparison with the results obtained in 2.4.3 shows that a reduction of the air pressure to 5×10^{-6} mm Hg reduces conduction heat transfer by a factor of 140, and total heat transfer by a factor of 13. With air at atmospheric pressure drift rates of better than 10^{-3o}C per min. were never obtainable. These drift rates were reduced to 10^{-4o}C per min. by evacuation of the calorimeter.

The introduction of a dummy absorber into the calorimeter effectively reduced the background drift rate by a factor of 5, so drift rates of about 2×10^{-5o}C per min. could readily be obtained.

4.5 Sensitivity of the system

Once again it seemed feasible that the majority of heat transfer which took place between the room and the absorber was through the window and the brass surroundings at the front of the calorimeter. Heat transfer in the calorimeter can be represented by a simple electrical analogue as shown in figure 21. A periodic variation of amplitude θ_1 and frequency ω

occurs on the inner surface of the calorimeter jacket. The calorimeter can be represented as an integrating circuit with a time constant $T = RC$, and a similar temperature variation of amplitude Θ_2 appears at the absorber.

From figure 21

$$\Theta_2(\omega) = \frac{1}{j\omega C}\left(\frac{1}{j\omega C} + R\right)^{-1} \Theta_1(\omega)$$

$$\Theta_2(\omega) = \frac{1 - j\omega T}{1 + \omega^2 T^2}\,\Theta_1(\omega)$$

Therefore amplitude $\left(\frac{\Theta_2}{\Theta_1}\right)^2 = \left(\frac{1}{1 + \omega^2 T^2}\right)^2 + \left(\frac{\omega T}{1 + \omega^2 T^2}\right)^2$

$$\frac{\Theta_2}{\Theta_1} = \left(\frac{1}{1 + \omega^2 T^2}\right)^{\frac{1}{2}}$$

If $\omega T \ll 1$, then $\Theta_2 = \Theta_1$, and variations in the temperature of the inner surface of the jacket will eventually appear at the absorber. Diurnal temperature variations are approximately $\pm$ 1°C, and these are reduced by a factor of 100 by the calorimeter jacket, resulting in an average drift rate of approximately 2×10^{-5}°C per min. If $\omega T \gg 1$, then $\Theta_2 = \frac{1}{\omega T}\Theta_1$. A good thermostat would provide a temperature variation of $\pm\ 10^{-2}$°C ($= \Theta_1$), with a time period of 10 secs ($= \frac{1}{\omega}$). As calculated $T = 250$ secs, therefore $\Theta_2 = \pm\ 4 \times 10^{-4}$°C. This corresponds to an average drift rate of 5×10^{-3}°C per min, and thus the drift rate over a short period of time is much worse than that obtained by the use of thermal damping. It is conceivable that thermostatic control of the air surrounding the calorimeter would lead to better temperature control, but this is not readily amenable to calculation. With the obtained drift rates, input powers of 1μW could be measured, and input powers of 0.01μW detected.

The adiabatic expansion caused by evacuating the calorimeter resulted in a drop of temperature of 2 to 3°C, and it was necessary to wait

for about two hours for the calorimeter to be completely operational. The air pressure inside the calorimeter can be exchanged rapidly between backing pressure (5×10^{-3} mm) and diffusion pressure (5×10^{-6} mm), and this is used to aid cooling of the absorber.

The room in which the calorimeter was operated had no temperature control and hence diurnal temperature variations also varied from day to day.

CHAPTER 5

ESTIMATION OF ENERGY LOSS DUE TO SCATTERED RADIATION

5.1 Introduction.

The X-ray linear attenuation coefficient μ of any material can be considered as being made up of three parts - one due to photoelectric absorption τ, one due to all types of scattering σ and one due to pair production k.

$$\mu = \tau + \sigma + k$$

Photoelectric absorption occurs when a photon imparts all its energy to an electron in an atom, thus ionizing the atom and resulting in complete annihilation of the photon. The atom may deionise by an electron falling from an outer shell into a vacancy in an inner shell, with the consequent release of a characteristic photon of lower energy.

Scattering may be inelastic (known as incoherent or Compton scattering), or elastic (known as coherent or Rayleigh scattering). Compton scattering occurs when a photon strikes a free electron. The free electron recoils with a particular energy, and the photon is scattered with a corresponding reduction in energy. A quantum mechanical treatment of this leads to the Klein-Nishina formula. Rayleigh scattering occurs when the photon is deflected with no loss in energy. Pair production does not occur for photons with energies of less than 1.022 MeV.

In the low energy X-ray region, photoelectric absorption is considerably larger than the absorption due to scattering, although Rayleigh scattering can become important at very low energies. Although this work essentially consists of totally absorbing a particular X-ray beam, the

characteristic and scattered photons produced by the above events may not be reabsorbed by the medium. Thus a fraction of the total incident energy will not be recorded. It is necessary to estimate this fraction for every X-ray beam and for every absorbing medium used in this work.

This problem may be approached experimentally or theoretically. It appears however, that an experimental determination would in itself be a major problem. Such a determination will only be necessary if theoretical results indicate that a large correction has to be applied. To simplify theoretical calculations it is assumed that a monochromatic pencil beam of X-rays is incident upon a cylinder of thickness T and radius a. The thickness T of the absorbing medium is sufficiently large to absorb at least 99.9% of the energy in the primary beam. The scatter losses can be divided into five parts each of which will be considered in turn.

a) Photoelectric backscatter through the front face of the cylinder, having an isotropic distribution.

b) Photoelectric sidescatter through the cylinder walls.

c) Compton and Rayleigh backscatter. In the energy range up to 30 keV, the energy lost by a photon involved in a Compton interaction is small (e.g. a 10 keV photon when scattered through 180° has an energy of 9.5 keV). Thus the Compton process is very similar to classical scattering, and the angular distribution of scattered photons is also very similar to the classical $1 + \cos^2 \phi$ distribution.

d) Compton and Rayleigh sidescatter.

e) Forward scatter due to the above processes, which, because T is sufficiently large, is negligible.

Figure 22

SCHEMATIC REPRESENTATION OF BACKSCATTER FROM A CYLINDER

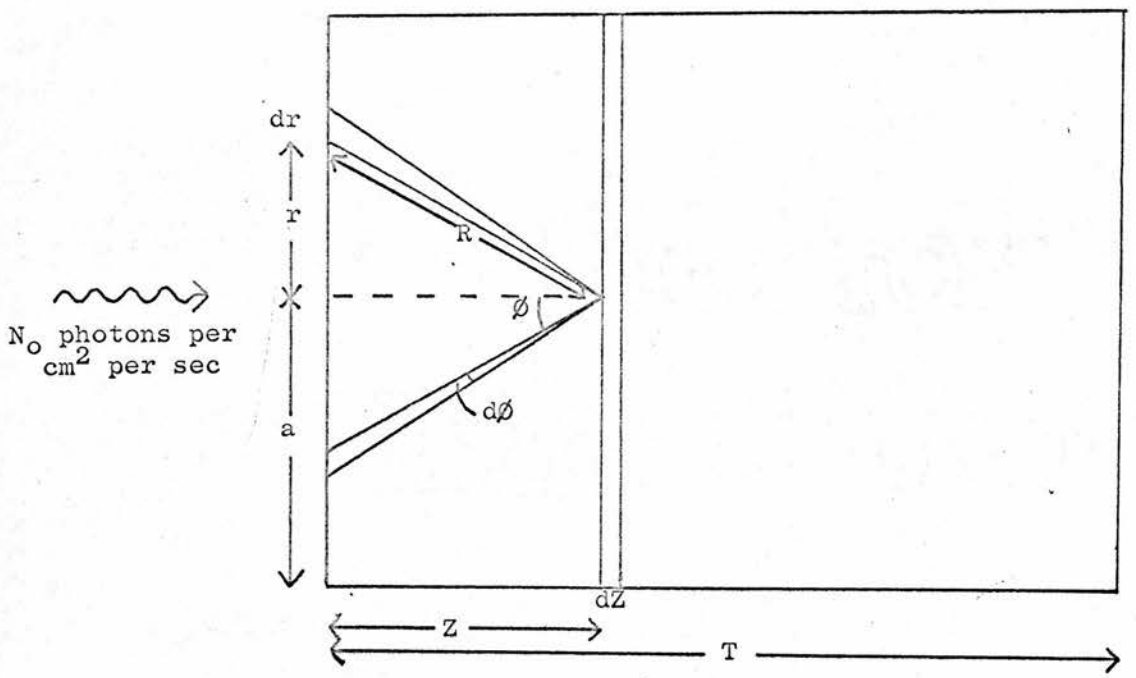

5.2 Photoelectric backscatter

A monoenergetic beam of N_o photons per cm^2 per sec. is incident upon the cylinder as shown in figure 22. At a depth z inside the cylinder ($z < T$), there are N photons per cm^2 per sec., and if the linear attenuation coefficient for the primary beam is μ, then

$$N = N_o \exp(-\mu z) \qquad \ldots\ldots\ldots 5 - 1$$

$\tau(\phi)$ is the photoelectric cross section at this energy in cm^2 per unit solid angle for scattering of the incident photon at an angle ϕ. The fluorescent yield of the shell in question is ω and the number of characteristic photons per cm^2 per sec. (dN'), emitted by a volume of unit area and thickness dz, between ϕ and $\phi + d\phi$ is then

$$dN' = N_o \exp(-\mu z)\, dz \;\; \omega \;\; \tau(\phi) \;\; \frac{2\pi r\, dr}{R^2} \qquad \ldots\ldots\ldots 5 - 2$$

As $dr = R\, d\phi$ and $R^2 = r^2 + z^2$

then $$\frac{2\pi r\, dr}{R^2} = 2\pi \sin\phi\, d\phi$$

Assuming an isotropic distribution $\tau(\phi) = \frac{\tau}{4\pi}$, and equation 5 - 2 gives

$$dN' = \frac{N_o}{2} \exp(-\mu z)\, dz \;\; \omega \;\; \tau \sin\phi\, d\phi$$

If μ' is the linear absorption coefficient for the characteristic radiation, then the number of photons per cm^2 per sec. which escape from the absorber between ϕ and $\phi + d\phi$ is dN" where

$$dN'' = dN' \exp\left(\frac{-\mu' z}{\cos\phi}\right) \qquad \ldots\ldots\ldots 5 - 4$$

$$dN'' = \frac{1}{2} N_o \omega\tau \exp -z\left(\mu + \frac{\mu'}{\cos\phi}\right) \sin\phi\, d\phi\, dz \qquad \ldots\ldots 5 - 5$$

This equation has to be integrated over the limits of $\phi = 0$ to $\phi = \tan^{-1}\frac{a}{z}$, which presents difficulties.

As most of the backscatter occurs from the volume very near to the front face,

Figure 23

VARIATION OF $1 - \frac{\mu'}{\mu} \ln(1 + \frac{\mu}{\mu'})$ WITH $\frac{\mu'}{\mu}$

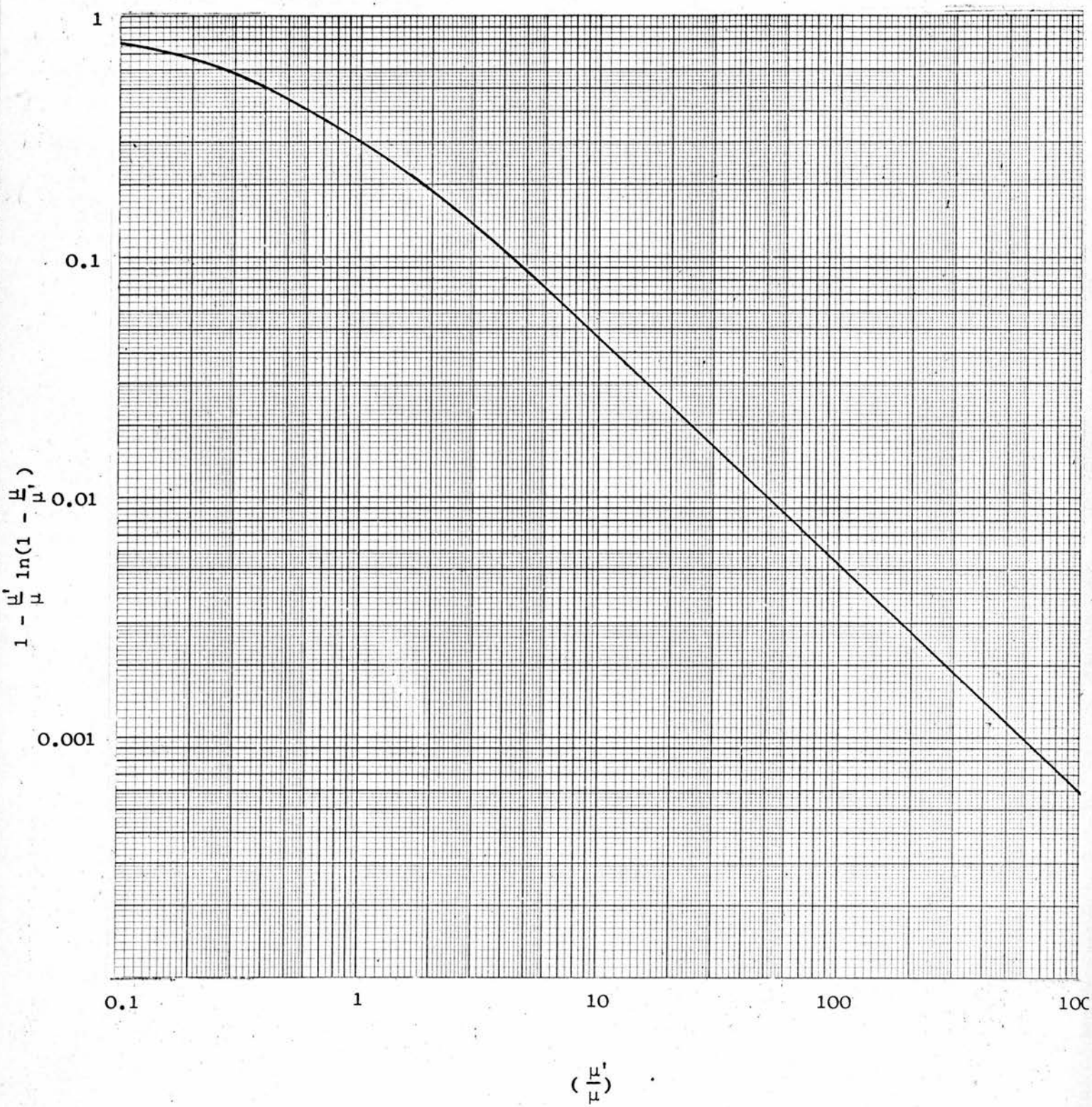

Figure 24

SCHEMATIC REPRESENTATION OF SIDESCATTER FROM A CYLINDER

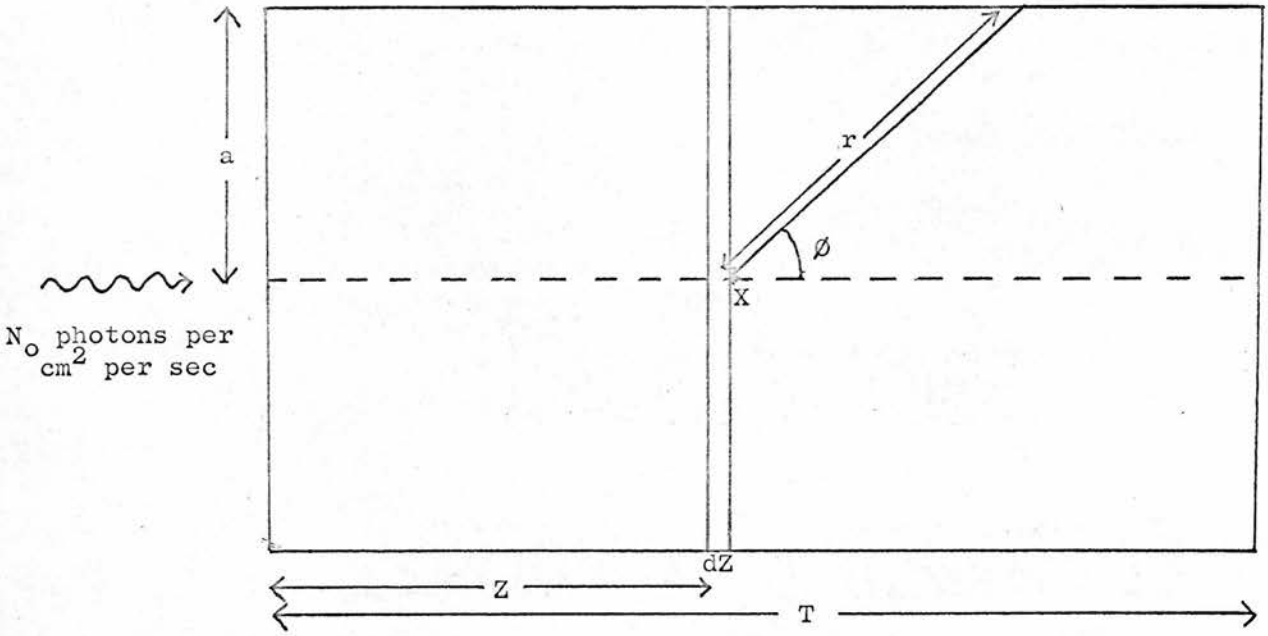

it is reasonable to assume that the surface appears infinite, and integrate over $\phi = 0$ to $\phi = \frac{\pi}{2}$

$$N'' = \frac{1}{2} N_o \tau \omega \int_{z=0}^{T} \int_{\phi=0}^{\frac{\pi}{2}} \exp -z \left(\mu + \frac{\mu'}{\cos \phi} \right) \sin \phi \, d\phi \, dz \quad \ldots\ldots 5-6$$

Integrating with respect to z gives

$$N'' = \frac{1}{2} N_o \tau \omega \left\{ \int_{\phi=0}^{\frac{\pi}{2}} \frac{\sin \phi \, d\phi}{\mu + \frac{\mu'}{\cos \phi}} - \exp(-\mu T) \int_{\phi=0}^{\frac{\pi}{2}} \frac{\sin \phi \exp\left(\frac{-\mu' T}{\cos \phi}\right) d\phi}{\mu + \frac{\mu'}{\cos \phi}} \right\}$$

As $\exp(-\mu T) = 0.001$, the second term in this integration can be disregarded

$$N'' = \frac{1}{2} N_o \tau \omega \int_{\phi=0}^{\frac{\pi}{2}} \frac{\sin \phi \, d\phi}{\mu + \frac{\mu'}{\cos \phi}}$$

Substituting $\cos \phi = x$, and integrating

$$N'' = \frac{1}{2} N_o \omega \frac{\tau}{\mu} \left\{ 1 - \frac{\mu'}{\mu} \ln \left(1 + \frac{\mu}{\mu'} \right) \right\} \quad \ldots\ldots 5-7$$

The percentage energy lost $\delta\varepsilon$ is required, so photon flux must be converted to energy flux. As τ is approximately equal to μ in this energy region then

$$\delta\varepsilon = \frac{50 \omega (h\nu)}{(h\nu_o)} \left\{ 1 - \frac{\mu'}{\mu} \ln \left(1 + \frac{\mu}{\mu'} \right) \right\} \% \quad \ldots\ldots 5-8$$

$h\nu_o$ is the energy of the incident radiation

$h\nu$ is the energy of the characteristic radiation

The variation of $1 - \frac{\mu'}{\mu} \ln \left(1 + \frac{\mu}{\mu'} \right)$ with $\frac{\mu'}{\mu}$ is shown in figure 23.

5.3 Photoelectric sidescatter

This is shown schematically in figure 24. A characteristic photon produced at the point X will then have to travel a distance $r = \frac{a}{\sin \phi}$ in

Figure 25

VARIATION OF $\int_0^{\pi/2} \sin \phi \, e^{-\frac{\mu' a}{\sin \phi}} \, d\phi$ WITH $\mu' a$

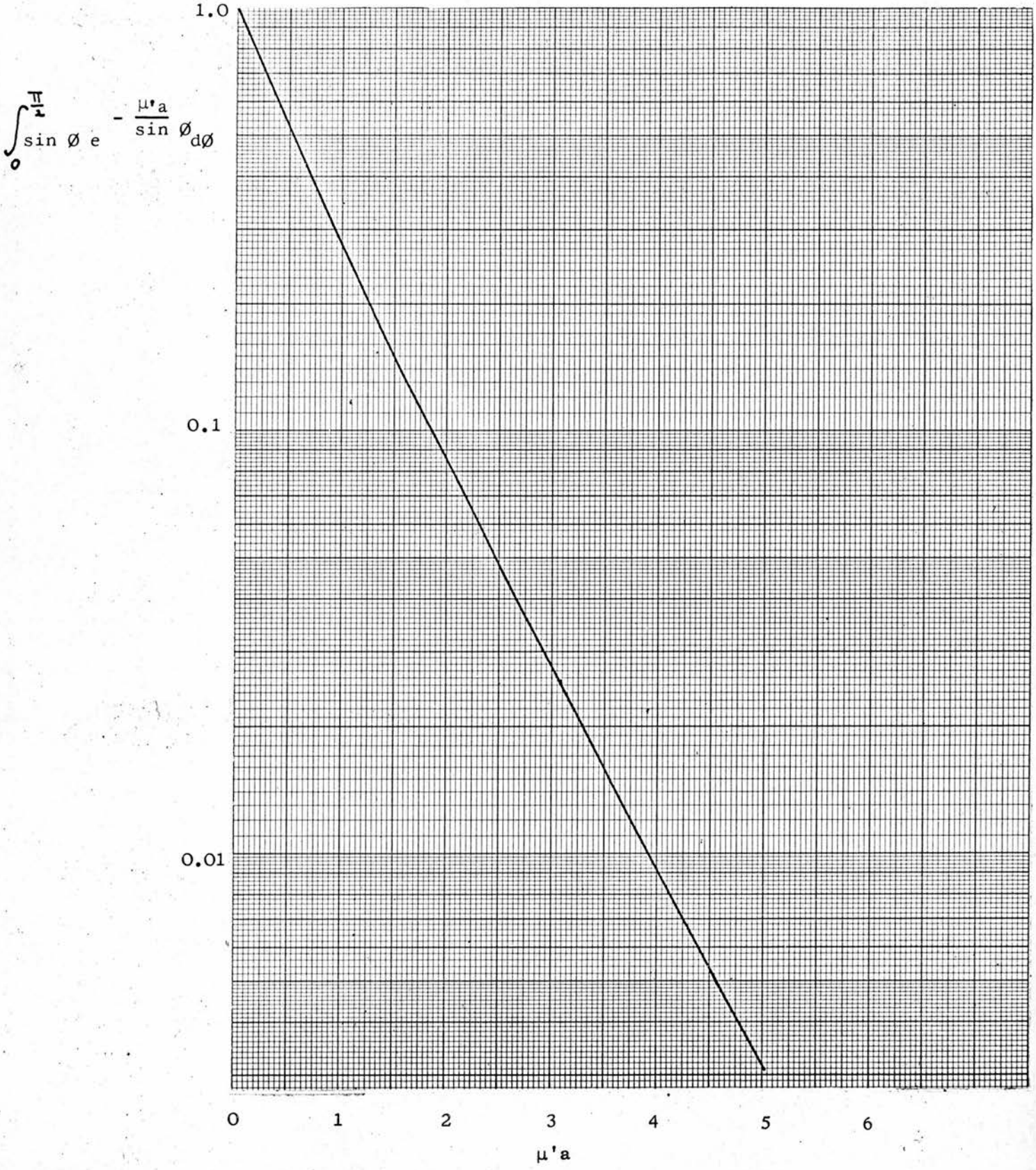

order to escape detection. The limits of integration again cause a problem, and there are two methods of looking at the limits over which Ø should be integrated. Assuming an infinite cylindrical surface, then

1. $\int_{\emptyset = 0}^{\frac{\pi}{2}}$ will underestimate the energy loss due to sidescatter and also underestimate the total energy loss.
2. $\int_{\emptyset = 0}^{\pi}$ will overestimate the energy loss due to sidescatter and similarly overestimate the total energy loss.

The two results obtained will simply differ by a factor of two in the estimation of the sidescatter energy loss, and the true result will lie between these two results.

If sidescatter can be neglected (as will be shown to be the case with the calorimeter), then no problem arises. However, with other dosimeters both of these integrations must be considered, and their respective merits discussed. In the following theory $\int_{\emptyset = 0}^{\pi}$ has been used, and equation 5 - 5 now gives

$$N'' = \frac{1}{2} N_o \tau \omega \int_{z=0}^{T} \int_{\emptyset = 0}^{\pi} \exp\left(-\mu z - \frac{\mu' a}{\sin \emptyset} \right) \sin \emptyset \, d\emptyset \, dz \quad \ldots\ldots 5-9$$

Integrating with respect to z gives

$$N'' = \frac{1}{2} N_o \omega \frac{\tau}{\mu} \left\{ 1 - \exp(-\mu T) \right\} \int_{\emptyset = 0}^{\pi} \sin \emptyset \exp\left(-\frac{\mu' a}{\sin \emptyset} \right) d\emptyset$$

Again $\tau = \mu$, and $\exp(-\mu T) = 0.001$, therefore

$$\delta\varepsilon = \frac{100 \, \omega \, (h\nu)}{(h\nu_o)} \int_{\emptyset = 0}^{\frac{\pi}{2}} \sin \emptyset \exp\left(-\frac{\mu' a}{\sin \emptyset} \right) d\emptyset \quad \% \quad \ldots\ldots\ldots 5 - 10$$

This integral is evaluated for various values of $\mu' a$ in figure 25.

5.4 Compton and Rayleigh Backscatter

Assume no energy change in scattering, that is $\mu' = \mu$ and $h\nu_o = h\nu$. $\sigma(\phi)$ is the coherent + incoherent cross section per unit solid angle for the incident radiation. Equation 5 - 2 gives

$$dN' = N_o \exp(-\mu z)\, dz \quad \sigma(\phi) \quad \frac{2\pi r\, dr}{R^2} \qquad \ldots\ldots\ldots 5 - 11$$

Assuming a $1 + \cos^2 \phi$ distribution, then $\frac{d\sigma}{d\Omega} = \sigma(\phi) = \text{const.} \times (1 + \cos^2 \phi)$

Therefore $\sigma(1 + \cos^2 \phi) = \sigma(\phi) \int_o^{\pi} 2\pi \sin \phi\, (1 + \cos^2 \phi)\, d\phi$

and $\sigma(\phi) = \frac{3\sigma}{16\pi} (1 + \cos^2 \phi)$

{ c.f. Isotropic distribution $\tau = \tau(\phi) \int_o^{\pi} 2\pi \sin \phi \cdot 1 \cdot d\phi$

$\tau(\phi) = \frac{\tau}{4\pi}$ }

Equation 5 - 11 now gives

$$dN' = N_o \exp(-\mu z)\, dz \frac{3\sigma}{16\pi} (1 + \cos^2 \phi)\, 2\pi \sin \phi\, d\phi \qquad \ldots\ldots 5 - 12$$

Combining equations 5 - 4 and 5 - 12 gives

$$dN'' = \frac{3}{8} N_o \sigma \exp\left\{-\mu z \left(1 + \frac{1}{\cos \phi}\right)\right\} \sin \phi\, (1 + \cos^2 \phi)\, d\phi\, dz$$

and integrating over the same limits gives

$$N'' = \frac{3}{8} N_o \sigma \int_{\phi = 0}^{\frac{\pi}{2}} \sin \phi\, (1 + \cos^2 \phi) \int_{z = 0}^{T} \exp\left\{-\mu z \left(1 + \frac{1}{\cos \phi}\right)\right\} dz\, d\phi$$

$\ldots\ldots\ldots 5 - 13$

Integrating with respect to z

$$N'' = \frac{3}{8} N_o \sigma \int_{\phi = 0}^{\frac{\pi}{2}} \sin \phi\, (1 + \cos^2 \phi) \frac{1}{\mu\left(1 + \frac{1}{\cos\phi}\right)} \left\{1 - \exp - \mu T \left(1 + \frac{1}{\cos\phi}\right)\right\} d\phi$$

Figure 26

VARIATION OF $\int_0^{\frac{\pi}{2}} (2 \sin \phi - \sin^3 \phi)\, e^{-\frac{\mu' a}{\sin \phi}} d\phi$ WITH $\mu' a$

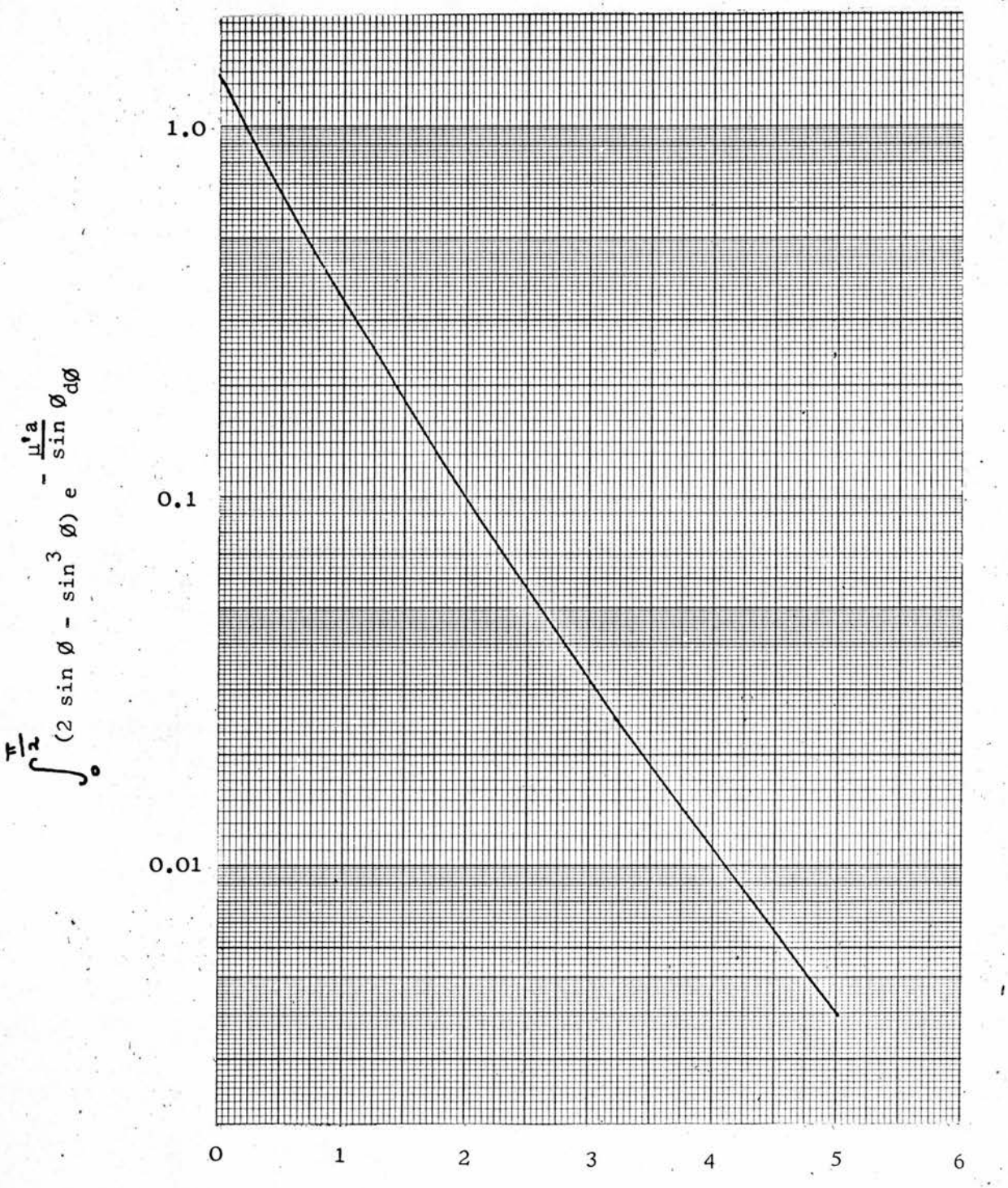

Again $\exp - \mu T \left(1 + \frac{1}{\cos \phi}\right)$ can be neglected

Therefore

$$N'' = \frac{3}{8} N_o \frac{\sigma}{\mu} \int_{\phi = 0}^{\frac{\pi}{2}} \frac{\cos \phi \sin \phi (1 + \cos^2 \phi)}{1 + \cos \phi} d \phi \quad \ldots\ldots\ldots 5 - 14$$

Substituting $\cos \theta = x$ and integrating by parts gives

$$N'' = N_o \times 0.168 \frac{\sigma}{\mu} \quad \ldots\ldots\ldots 5 - 15$$

As there is no energy change on scattering, then

$$\delta \varepsilon = 16.8 \left(\frac{\sigma}{\mu}\right) \% \quad \ldots\ldots\ldots 5 - 16$$

5.5 Compton and Rayleigh sidescatter

In this calculation a $1 + \cos^2 \phi$ distribution is again assumed. The geometrical assumptions are the same as in 5 - 3, and equation 5 - 9 now gives

$$N'' = N_o \int_{z = 0}^{T} \int_{\phi = 0}^{\pi} \exp \left(-\mu z - \frac{\mu' a}{\sin \phi}\right) \sigma(\phi) 2\pi \sin \phi \, d \phi \, dz \quad \ldots\ldots 5 - 17$$

Substituting for $\sigma(\phi)$ gives

$$N'' = \frac{3}{8} N_o \sigma \int_{z = 0}^{T} \exp (-\mu z) \, dz \int_{\phi = 0}^{\pi} \sin \phi (1 + \cos^2 \phi) \exp\left(\frac{-\mu' a}{\sin \phi}\right) d \phi$$

Integrating with respect to z

$$N'' = \frac{3}{8} N_o \frac{\sigma}{\mu} \left\{1 - \exp (-\mu T)\right\} \int_{\phi = 0}^{\pi} \sin \phi (1 + \cos^2 \phi) \exp \left(\frac{-\mu' a}{\sin \phi}\right) d \phi$$

Once again $\exp (-\mu T)$ can be neglected, therefore the percentage energy loss is given by

$$\delta \varepsilon = 75 \left(\frac{\sigma}{\mu}\right) \int_{\phi = 0}^{\frac{\pi}{2}} (2 \sin \phi - \sin^3 \phi) \exp \left(\frac{-\mu' a}{\sin \phi}\right) d \phi \quad \ldots\ldots\ldots 5 - 18$$

This integral is evaluated for various values of $\mu' a$ in figure 26.

Figure 27

VARIATION OF $\Delta\varepsilon$ % WITH ENERGY FOR PHOTOELECTRIC BACKSCATTER FROM GOLD

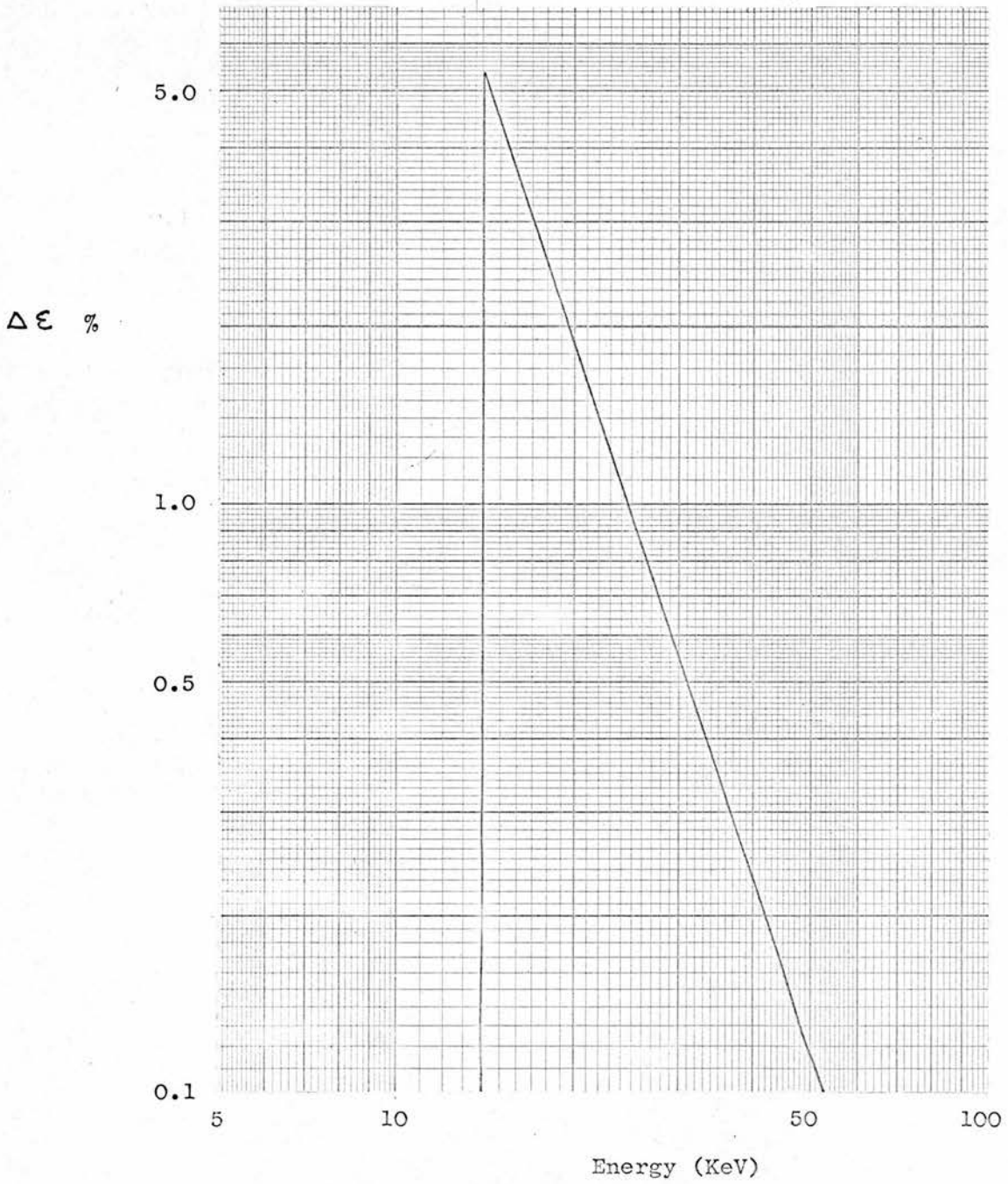

Figure 28

VARIATION OF σ (COHERENT + INCOHERENT) AGAINST ENERGY FOR GOLD

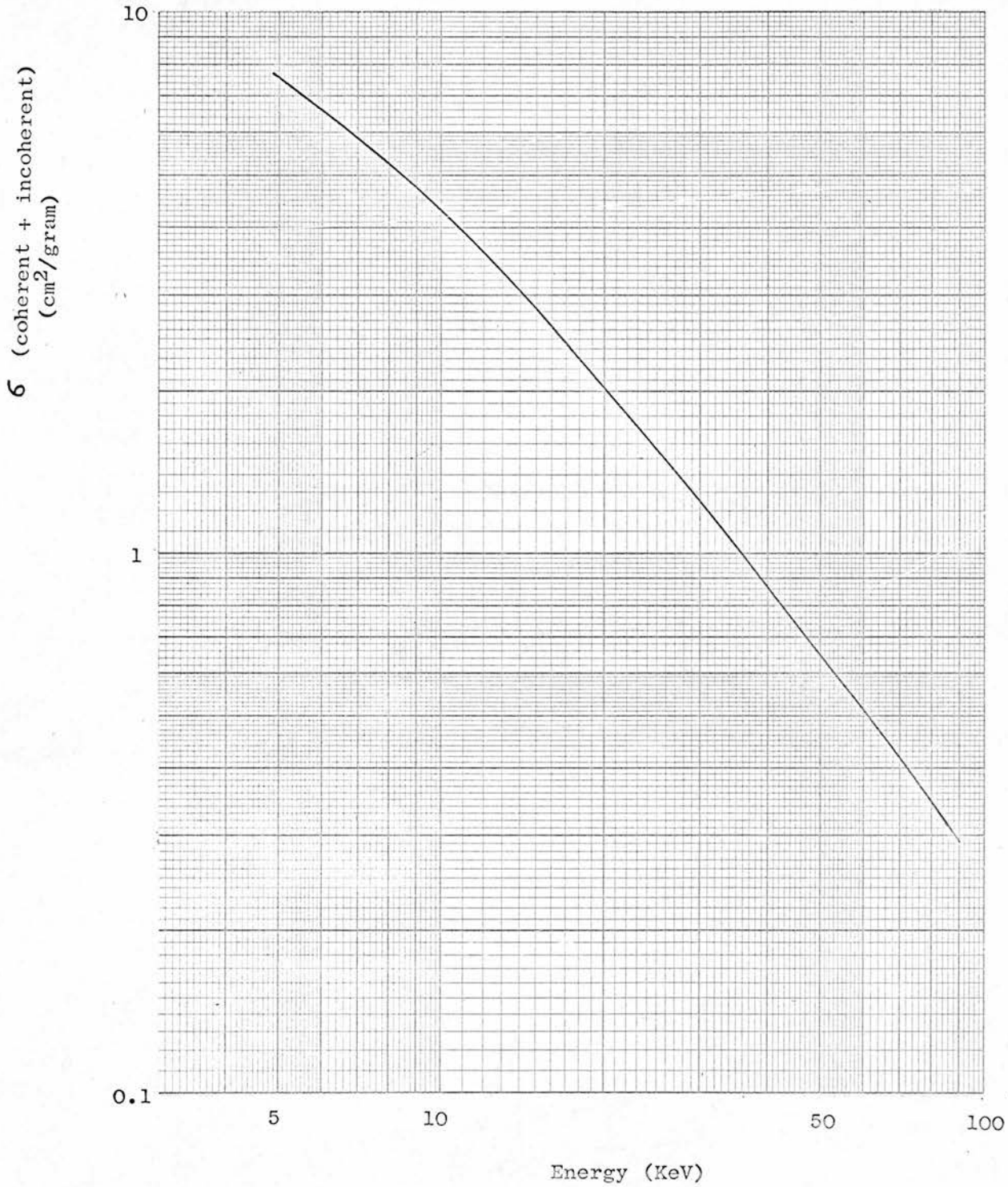

Figure 29

VARIATION OF $\Delta\varepsilon$ % WITH ENERGY FOR COMPTON + RAYLEIGH BACKSCATTER FROM GOLD

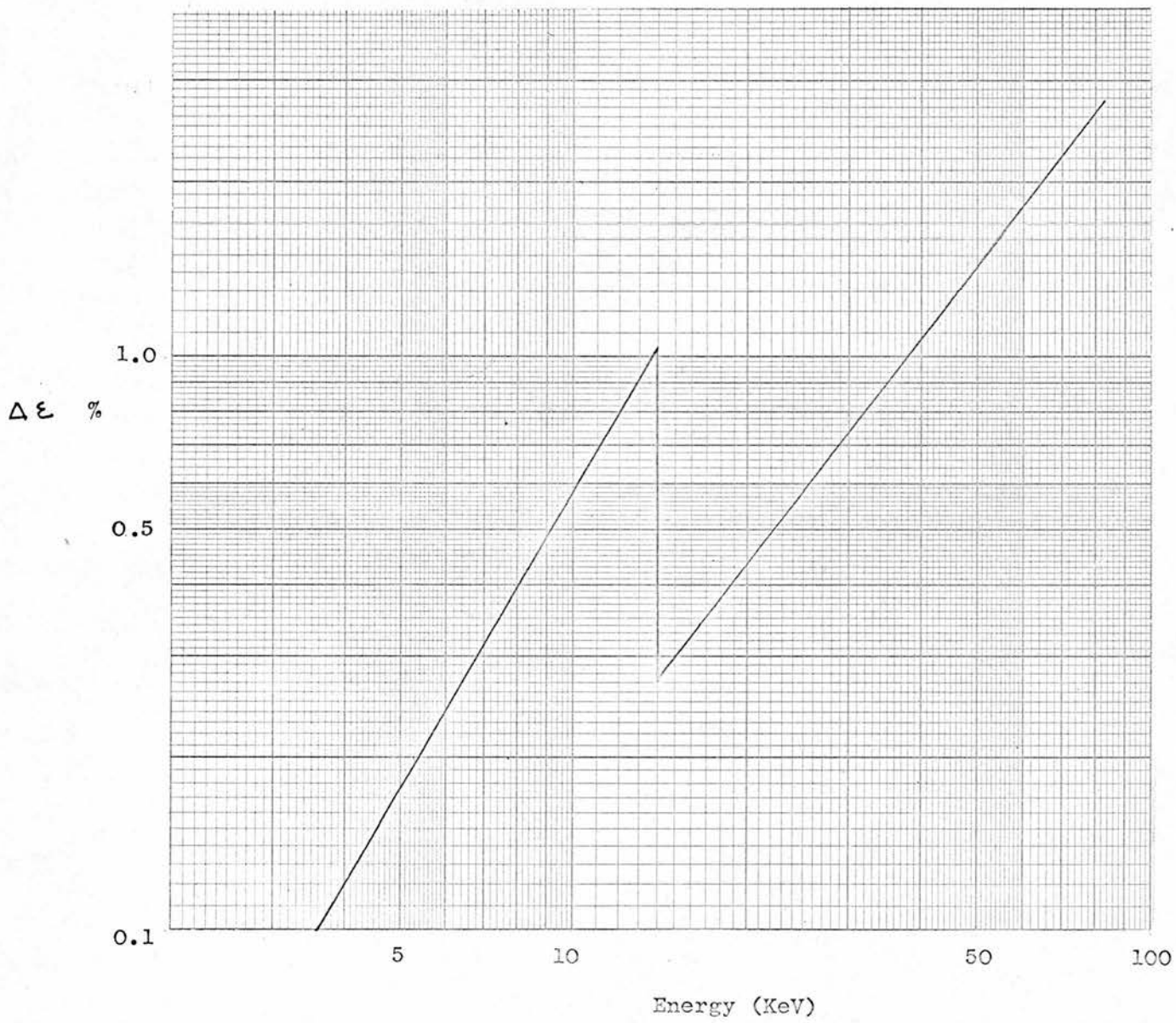

Figure 30

VARIATION OF $\Delta\varepsilon$ % WITH ENERGY FOR TOTAL BACKSCATTER FROM GOLD

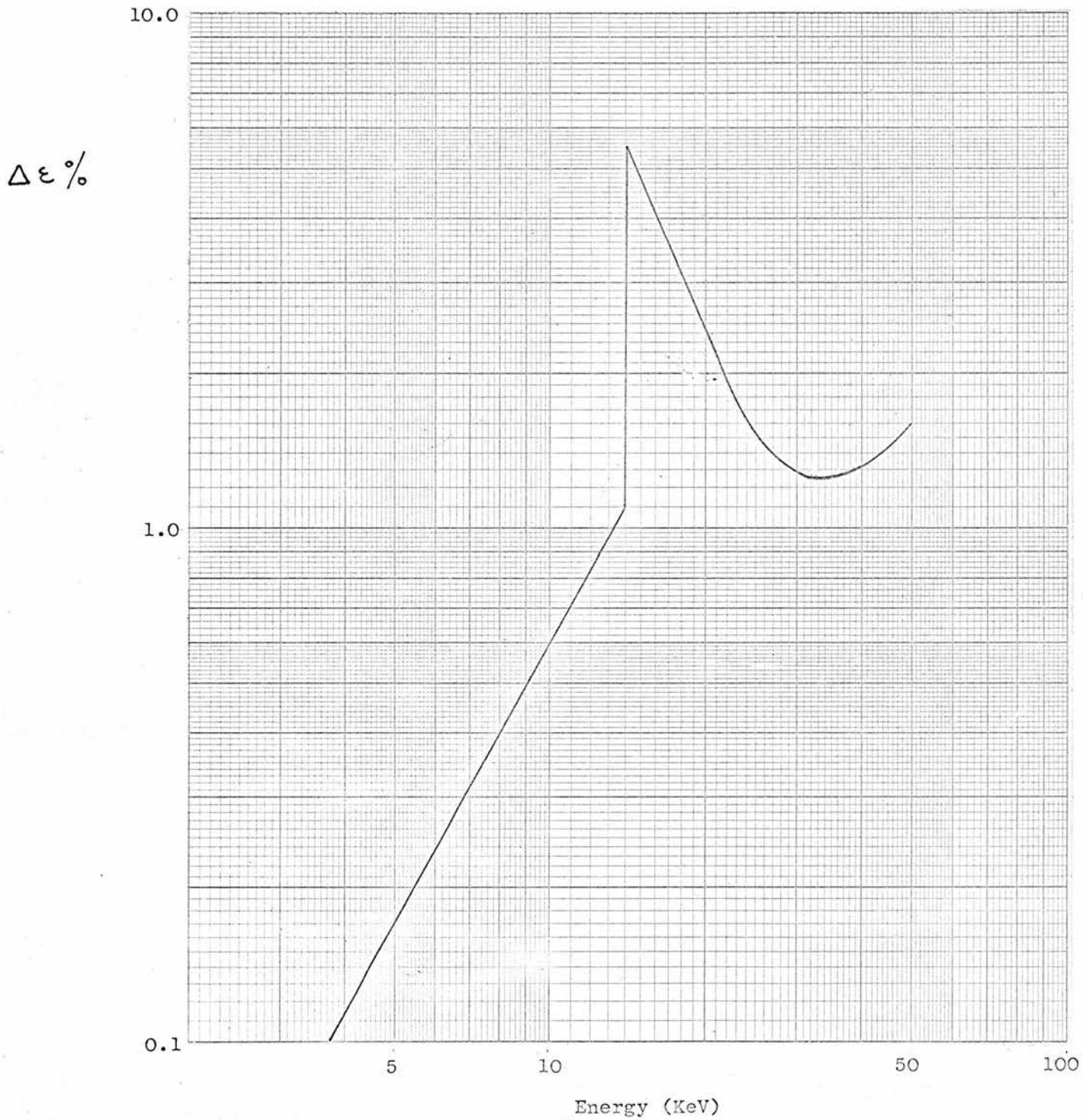

5.6 Conclusions and results

Combining equations 5 - 8, 5 - 10, 5 - 16 and 5 - 18 gives the total percentage energy lost from the absorber as

$$\delta\varepsilon = 50\omega \left(\frac{h\nu}{h\nu_o}\right)\left[\left\{1 - \frac{\mu'}{\mu}\ln\left(1 + \frac{\mu}{\mu'}\right)\right\} + 2\int_{\phi=0}^{\frac{\pi}{2}} \sin\phi \exp\left(\frac{-\mu' a}{\sin\phi}\right) d\phi\right]$$
$$+ \frac{\sigma}{\mu}\left[16.8 + 75\int_{\phi=0}^{\frac{\pi}{2}} (2\sin\phi - \sin^3\phi) \exp\left(\frac{-\mu' a}{\sin\phi}\right) d\phi\right] \% \quad \ldots\ldots 5 - 19$$

In calculating the energy lost from the gold absorber in the calorimeter sidescatter can be completely neglected. However this has been evaluated here for the sake of completeness and will be used later (Chapter 8).

Figure 27 shows the variation of the percentage energy lost with incident energy for gold due to photoelectric backscatter (calculated from equation 5 - 8). This increased with decreasing energy until the L absorption edge of gold is reached, however at lower energies it is negligible. In this calculation ω_L was taken as 0.38 (35), and $\frac{\mu'}{\rho}$ for L α radiation as 133 cm^2/gram (9.71 keV)(37). Photoelectric sidescatter is negligible for large values of $\mu'a$ (figure 25). In this particular example $\frac{\mu'}{\rho}$ = 133 cm^2/gram, ρ = 19.3 grams/cm^3 and a = 1 cm, therefore $\mu'a$ = 2570, and is certainly negligible. For the same reason Compton and Rayleigh sidescatter can be neglected.

Figure 28 shows the variation of the coherent + incoherent cross-section with energy (38). This was used in conjunction with figure 18 to evaluate the energy loss due to Compton and Rayleigh backscatter, and the result is shown in figure 29. By combining figures 27 and 29, the solution to equation 5 - 19 is obtained and is shown in figure 30.

Table 7 shows the calculation of the energy lost by a heterogenous beam of X-rays. Columns 1 and 2 represent the 30 kVp spectrum used in 4.1. Column 3 represents the percentage energy lost $\delta\varepsilon$ at the various mean energies of the spectrum. $\sum \delta E \delta\varepsilon$ over all mean energies gives the total energy loss due to scatter, which is 1.73% for 30 kVp X-rays.

Table 7

1	2	3	4
Mean Energy	Fractional energy per 2 keV interval δE	% energy lost due to scatter (from fig.30) $\delta\varepsilon$	$\delta E\ \delta\varepsilon$
6	0.069	0.232	0.016
8	0.143	0.395	0.056
10	0.203	0.600	0.122
12	0.190	0.830	0.158
14	0.099	5.60	0.554
16	0.078	4.15	0.324
18	0.063	3.10	0.195
20	0.052	2.45	0.127
22	0.041	1.97	0.081
24	0.031	1.65	0.051
26	0.019	1.45	0.028
28	0.008	1.36	0.011
30	0.004	1.29	0.005

Similar calculations were carried out for beams generated at peak voltages of 10, 15, 20 and 25 kV, using typical spectra obtained (34). The results with their estimated uncertainties are given in table 8.

Table 8

Peak kilovoltage of X-ray beam	% energy lost due to backscatter
10	negligible
15	0.5 ± 0.1
20	1.4 ± 0.3
25	1.6 ± 0.3
30	1.7 ± 0.4

Figure 31

MONITOR CHAMBER

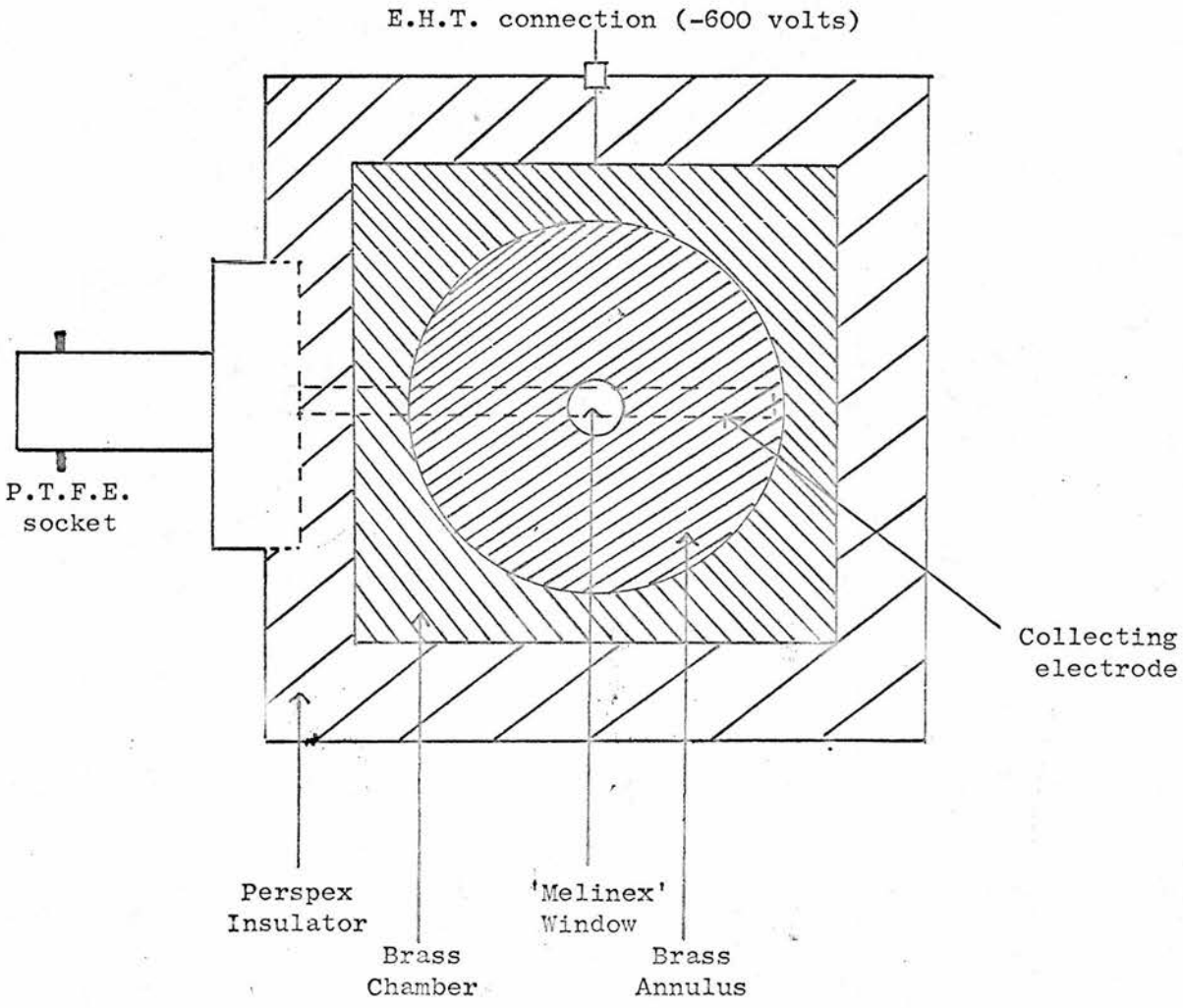

Figure 32

MONITOR CHAMBER ASSEMBLY

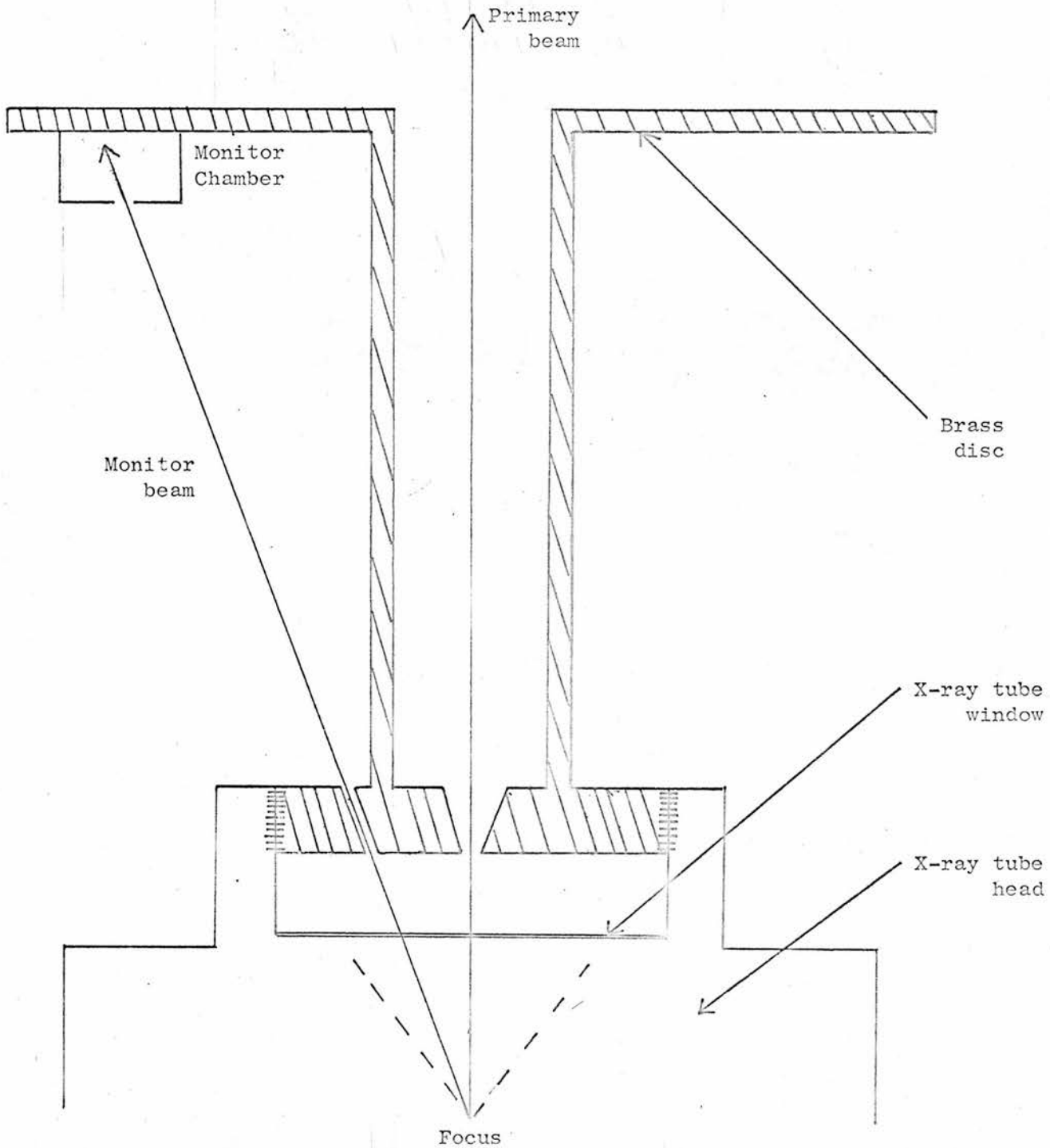

Figure 33

INTEGRATING CIRCUIT FOR MONITOR CHAMBER

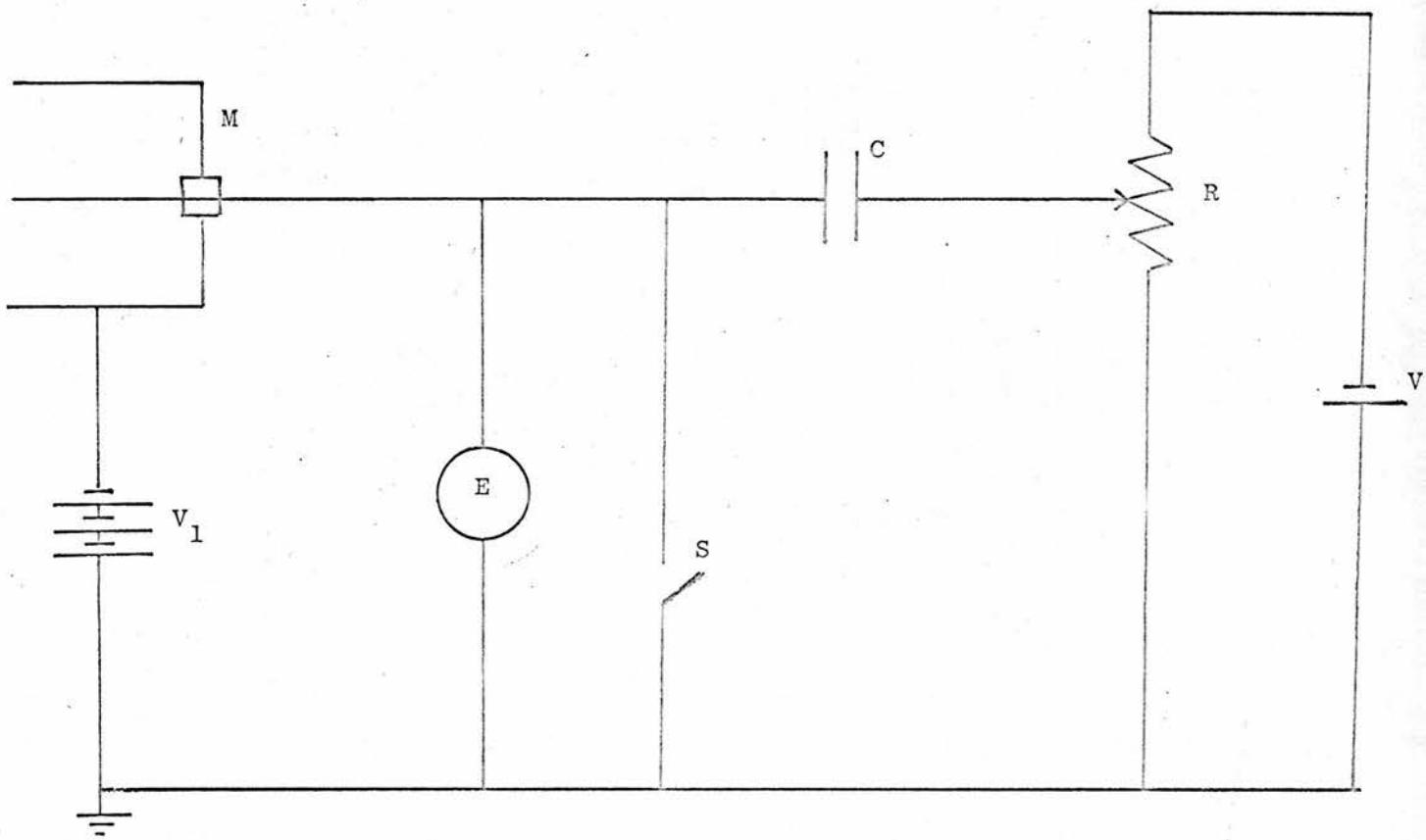

V_1 - (-600 volts)

M - Monitor Chamber

E - Electrometer

S - Discharge Switch

C - Integrating Capacitor

R - 10KΩ Decade Box

V_2 - Standardised voltage source (10 volts)

CHAPTER 6

ENERGY FLUENCE MEASUREMENTS WITH THE CALORIMETER

6.1 Monitoring of X-ray beam

A continual variation of X-ray tube output occurs due to kilovoltage and milliamperage drifts, and on any day the output appears to decrease with operational time. These produce random scatter in the calorimeter results, and in order to reduce this scatter an independent but simultaneous measurement must be made of the X-ray tube output. It is essential that as far as possible the same quality beam is monitored as that which the calorimeter is measuring. This is even more critical with low energy X-rays because of the rapid variation of interaction cross-sections with energy.

The monitor used in this work is a small ionization chamber shown in figure 31. It consists of a small brass chamber with a 'Melinex' entrance window. A potential difference of - 600 volts (sufficient to achieve saturation) is applied between this chamber and a central electrode. Perspex insulation surrounds the chamber, and connection is made by means of a P.T.F.E. socket. The monitor chamber is then mounted on the rear of a brass disc, and the whole assembly screwed into the X-ray tube head as shown in figure 32. The total spread of the X-ray beam is 44°, hence it is possible to produce a secondary beam for monitoring provided it is taken at an angle of less than 22° to the primary beam.

The current from the monitor chamber is integrated by means of the circuit shown in figure 33. The current from the chamber is allowed to charge up a $0.5\mu F$ capacitor. The voltage produced is backed off by the standard voltage source described in 3.4, the electrometer being used as a null detector. This measuring system has an accuracy of better than 0.1%.

The voltage developed across the capacitor is a measure of the total X-ray output, and when divided by the time of integration, will from now on be referred to as the 'monitor unit'.

6.2 Experimental procedure

Assuming that heat losses in the calorimeter system remain constant, then the temperature rise produced by a particular input power will always be constant. However results, when obtained in the kinetic, semi-adiabatic and 'temperature rise after a measured time' methods, are initially expressed in divisions of recorder scale. It is therefore necessary to calibrate the recorder scale, that is, convert divisions of recorder scale to ^{o}C. This is done in the following manner.

$$D\ \left(\frac{\text{div}}{\text{min}}\right) \times \frac{1}{L}\ \left(\frac{\Omega}{\text{div}}\right) \times M\ \left(\frac{^{o}C}{\Omega}\right) = N\ \left(\frac{^{o}C}{\text{min}}\right)$$

The sensitivity L is obtained by determining the response of the recorder to a resistance switch in the variable arm of the bridge. M is governed by the non-linearity of the thermistor resistance over variations in the operation temperature of the system. Equation 3 - 5 gives

$$\delta S = -\frac{BS}{\theta^2}\,\delta\theta$$

Therefore

$$M = \frac{\delta\theta}{\delta S} = -\frac{\theta^2}{BS}$$

i.e. $M \propto \frac{\theta^2}{S}$ and each result has to be normalized by multiplying by the absolute temperature squared, and dividing by the resistance of the thermistors in the irradiated absorber; the former of these introduces a relatively small correction and has not been carried out in practice.

Figure 34

KINETIC METHOD OF OPERATION

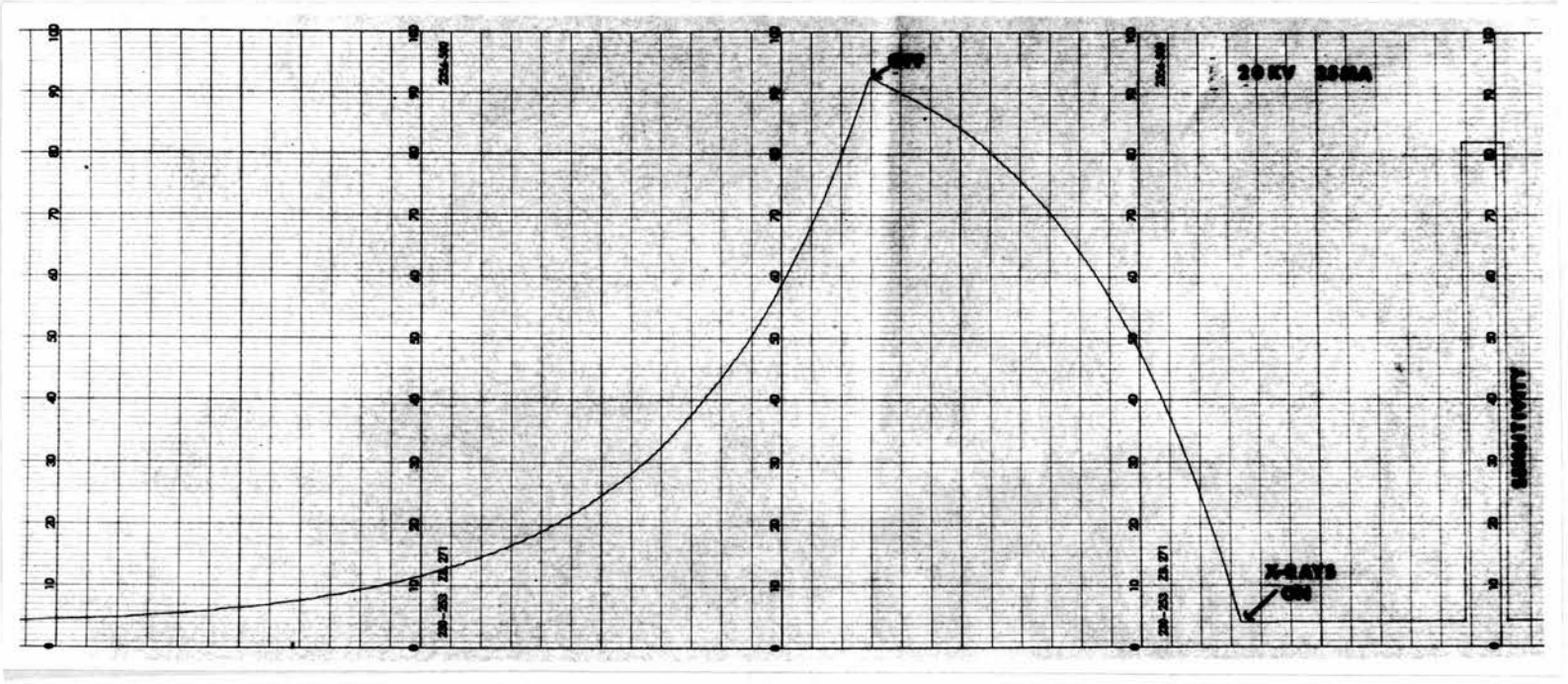

Table 9

Calorimeter results using kinetic method

Run Type	Resistance S (Ω)	Sensitivity L (div/Ω)	Initial Slope D (div/min)	Response $N = D/LS$ ($\alpha\,^{\circ}C$)/min	Monitor M (volts)	Time T (secs)	Monitor Unit x 10^2 (volts/sec)
Calibration 231.8μW	19,684	9.50	20.96	11.21			
X-ray	19,684	9.50	20.93	11.19	6.765	300	2.255
Calibration 231.8μW	19,680	9.50	20.44	10.93			
X-ray	19,680	9.53	20.62	10.99	6.751	300	2.250
Calibration 231.8μW	19,678	9.53	20.76	11.07			
X-ray	19,674	9.54	20.70	11.03	6.681	300	2.227
Calibration 231.8μW	19,674	9.54	20.93	11.15			
X-ray	19,670	9.55	20.28	10.80	6.707	300	2.238

Average calibration response $C = 11.09 \pm 0.06$ ($\alpha\,^{\circ}C$/min)

Average X-ray response $X = 11.00 \pm 0.08$ ($\alpha\,^{\circ}C$/min)

Ratio $\frac{X}{C} = 0.9919 \pm 0.0091$

Input power $P = 231.8\ \mu W$

Average X-ray power $\frac{XP}{C} = 230.0 \pm 2.1\ \mu W$

Average X-ray energy per monitor unit $\frac{XPT}{CM} = (10.26 \pm 0.07) \times 10^4$ ergs.

Therefore

$$N = \frac{D}{LS} \qquad \ldots\ldots\ldots 6 - 1$$

where L is expressed in divisions per ohm.

Electrical calibration responses so obtained are divided by the input power to give a calibration constant. The X-ray responses are normalised by the monitor unit to give a constant for a particular X-ray beam. A procedure of alternating calibration and X-ray exposures is adopted, and the beam energy in ergs per monitor unit evaluated from the mean of these calibration and X-ray runs.

6.3 Comparison of various methods

The X-ray beam used in this comparison was generated at 30kV and 25mA, although typical recorder traces illustrating the various methods were taken at 20kV and 25mA. The aperture used was nominally 0.178 sq.cm. ($^3/16$ ins diameter).

6.3.1 Kinetic method

A typical experimental heating and cooling curve for the calorimeter is shown in figure 34. $\frac{d\theta}{dt}$ is obtained at known values of $\theta - \theta_o$ by drawing tangents to the curve, and $(\frac{d\theta}{dt})_{\theta = \theta_o}$ extrapolated by the method of least squares. This is carried out for each individual result. The sensitivity is obtained from the 10Ω switch at the beginning of the recorder trace, and the resistance of the thermistors is determined as described in 3.2. Results are shown in Table 9.

The irradiation times were measured by a stopwatch. After a five minute heating run, the time taken to cool to equilibrium temperature is approximately twenty minutes. This can be reduced to about five minutes by switching off the diffusion pump. However it is improbable that an

Figure 35

SEMI ADIABATIC METHOD OF OPERATION

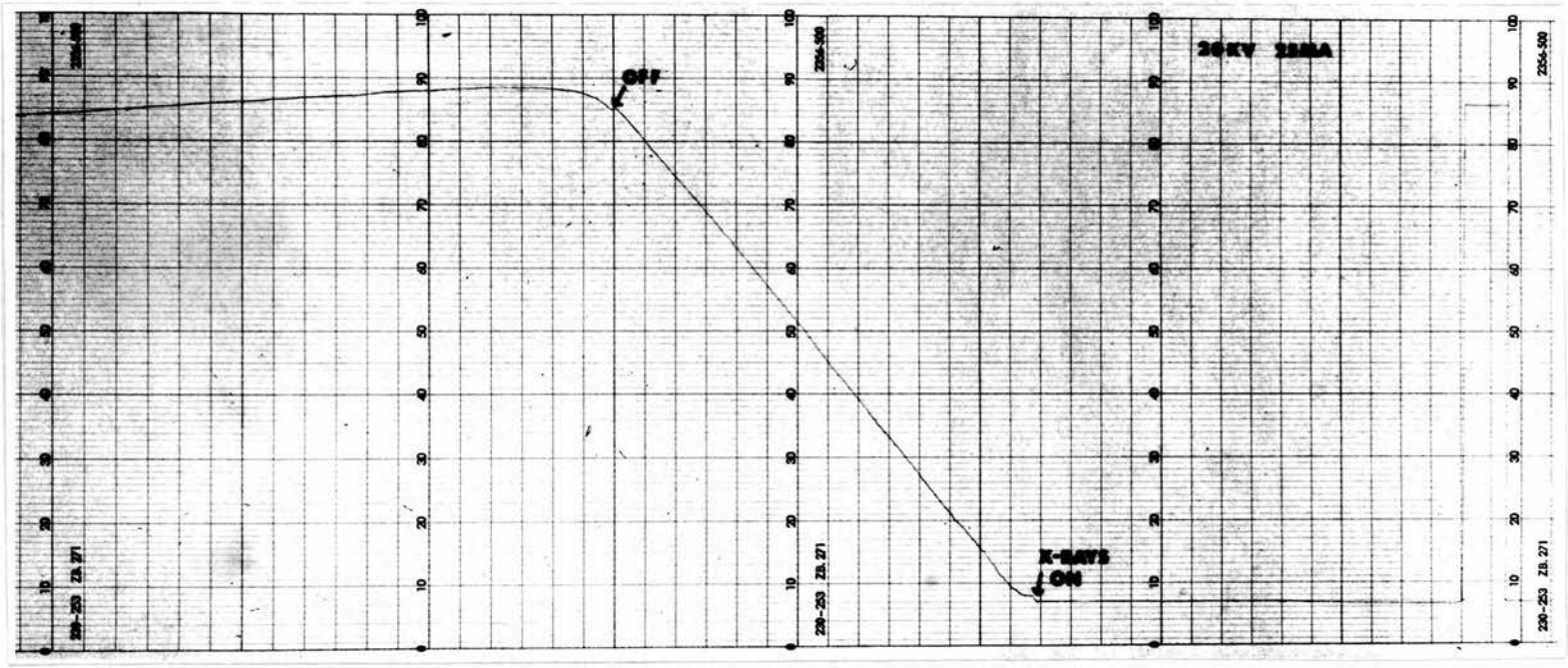

Table 10

Calorimeter results using semi adiabatic method

Run Type	Resistance S (Ω)	Sensitivity L (div/Ω)	Heating Slope (div/min)	Cooling Slope (div/min)	Corrected Slope D (div/min)	Response $N = D/LS$ (α °C/min)	Monitor M (volts)	Time T (secs)	Monitor Unit x 10^2 (volts/sec)
Calibration	20,524	79.8	51.90	5.08	49.36	3.014			
X-ray	20,530	79.8	52.63	5.06	50.10	3.058	0.4675	20.6	2.269
Calibration	20,524	79.5	51.64	5.02	49.13	3.011			
X-ray	20,516	79.5	52.76	4.98	50.27	3.082	0.4567	20.2	2.261
Calibration	20,510	79.5	52.04	4.98	49.55	3.039			
X-ray	20,500	79.7	53.00	5.06	50.47	3.089	0.4264	18.65	2.287
Calibration	20,486	80.0	52.41	5.14	49.84	3.041			
X-ray	20,466	80.0	52.84	5.12	50.28	3.071	0.4433	19.4	2.285

Average calibration response $C = 3.026 \pm 0.008$ (α °C/min)

Average X-ray response $X = 3.070 \pm 0.007$ (α °C/min)

Ratio $\frac{X}{C} = 1.015 \pm 0.003$

Input Power $P = 231.8$ μW

Average X-ray Power $\frac{XP}{C} = 235.2 \pm 0.8$ μW

Average X-ray energy per monitor unit $\frac{XPT}{M} = (10.35 \pm 0.04) \times 10^4$ ergs.

Figure 36

TEMPERATURE RISE AFTER A FIXED TIME

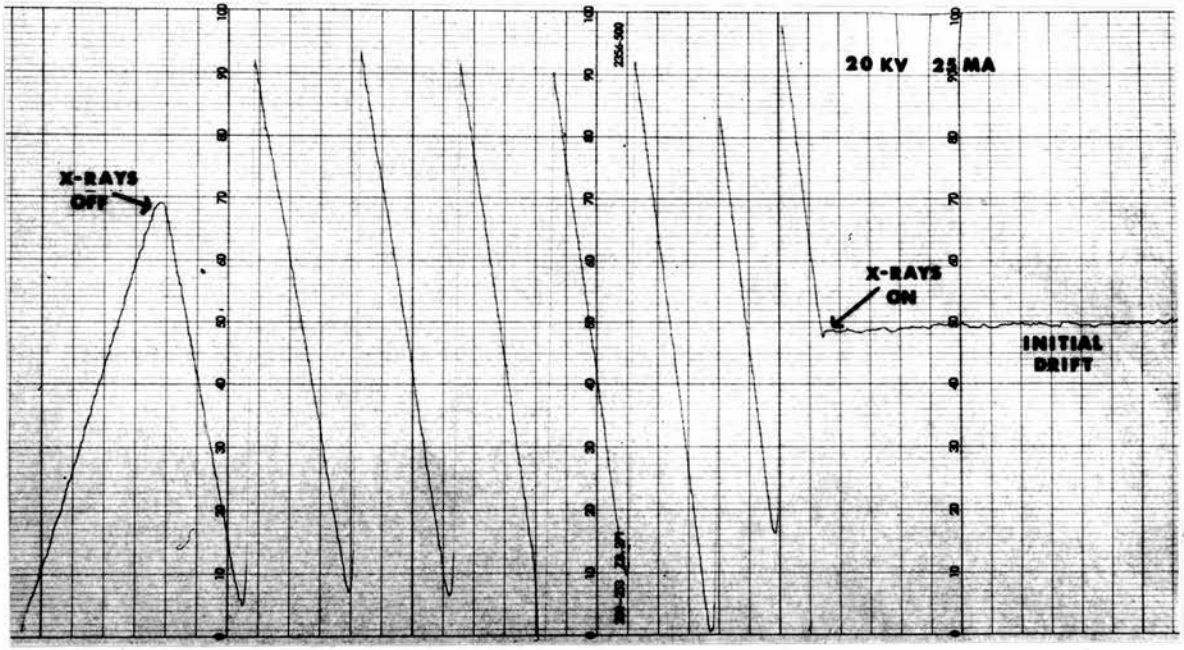

Table 11

Calorimeter results using temperature rise after fixed time

Run Type	Resistance S (Ω)	Sensitivity L (m.v./Ω)	Deflection after 2 min D (m.v.)	Response $N = D/LS$ ($\propto {}^{o}C$)	Monitor M (volts)	Time T (secs)	Monitor Unit x 10^2 (volts/sec)
Calibration	20,152	155.3	274.5	8.770			
X-ray	20,074	156.0	278.0	8.875	2.716	120	2.263
Calibration	20,042	157.2	276.1	8.766			
X-ray	19,970	157.5	276.2	8.783	2.691	120	2.243
Calibration	19,912	158.0	275.9	8.771			
X-ray	19,862	158.3	277.0	8.809	2.693	120	2.244
Calibration	19,820	158.5	278.0	8.850			
X-ray	19,788	159.0	276.3	8.783	2.707	120	2.259

Average calibration response $C = 8.789 \pm 0.022$ ($\propto {}^{o}C$)

Average X-ray response $X = 8.813 \pm 0.024$ ($\propto {}^{o}C$)

Ratio $\frac{X}{C} = 1.003 \pm 0.003$

Input Power $P = 231.8$ μW

Average X-ray power $\frac{XP}{C} = 232.4 \pm 0.6$ μW

Average X-ray energy per monitor unit $\frac{XPT}{CM} = (10.32 \pm 0.03) \times 10^4$ ergs.

individual run can be carried out in less than fifteen minutes, and a further fifteen minutes are required to evaluate the result.

Time per run = 30 mins.

Total time to obtain result = 4 hours.

6.3.2 Semi-adiabatic method

The recorder trace obtained in a semi-adiabatic run is shown in figure 35. The correction to be applied from the initial drift rate was always small enough to be neglected. Heating and cooling slopes were measured by drawing the best straight line. Results are shown in Table 10. As heating periods are short there is no advantage in assisting cooling by switching off the diffusion pump. The results are calculated quickly, but normalisation and calibration readings have to be taken. Irradiation times were again measured by a stopwatch.

Time per run = 15 mins.

Total time to obtain result = 2 hours.

6.3.3 Temperature rise after a measured time

The time chosen for the heating period was two minutes. The temperature rise obtained is effectively measured by backing off the recorded out of balance voltage with a standardised voltage (3 - 4). A sensitivity measurement can be made in the same way. The sensitivity of the recorder can be increased near to switching off the input power, and so greater accuracy in the determination of this critical point can be obtained. A typical response is shown in figure 36. The initial recorded drift is extrapolated over the heating period, and an estimation of the background temperature at the time of switching off the input power so obtained. Results are shown in Table 11. Cooling was assisted by switching off the diffusion pump, and again results could be rapidly evaluated.

Figure 37

RECORDER ATTACHMENT USED IN THERMAL CYCLING METHOD

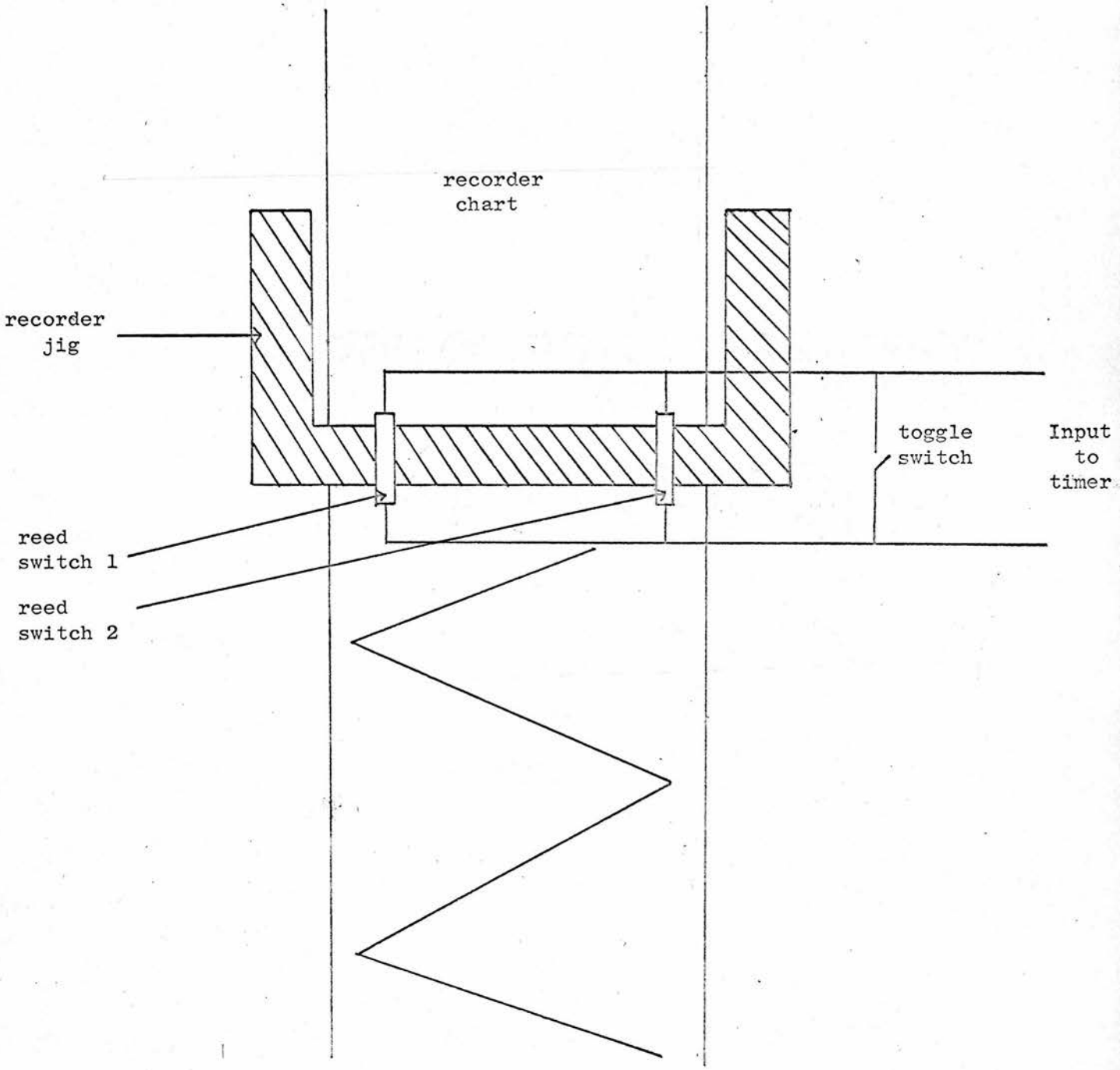

Table 12

Calorimeter results using thermal cycling

Run Type	Heating Time t_1 (secs)	Cooling Time t_2 (secs)	Response $\frac{1}{t_1} + \frac{1}{t_2}$ ($\alpha^{\circ}C$)	Monitor M (volts)	Time T (secs)	Monitor Unit x 10^2 (volts/sec.)
Calibration	19.68	21.99	9.627			
X-ray	19.83	21.97	9.594	0.4345	19.2	2.263
Calibration	19.70	22.15	9.591			
X-ray	19.97	22.21	9.510	0.4407	19.7	2.237
Calibration	19.56	22.15	9.627			
X-ray	19.45	22.09	9.669	0.4157	18.5	2.247
Calibration	19.46	22.05	9.676			
X-ray	19.24	21.96	9.750	0.4165	18.3	2.276

Average calibration response $C = 9.630 \pm 0.017$ ($\alpha^{\circ}C$)

Average X-ray response $X = 9.631 \pm 0.051$ ($\alpha^{\circ}C$)

Ratio $\frac{X}{C} = 1.000 \pm 0.005$

Input Power $P = 231.8$ μW

Average X-ray power $\frac{XP}{C} = 231.8 \pm 1.2$ μW

Average X-ray energy per monitor unit $\frac{XPT}{CM} = (10.28 \pm 0.03) \times 10^4$ ergs.

Time per run = 15 mins.

Total time to obtain result = 2 hours

6.3.4 Thermal cycling

The absorber was heated to a temperature above the surroundings where the heating and cooling rates were approximately equal. The recorder sensitivity was then adjusted until the pen travelled full scale deflection in approximately 20 secs (less than 0.1T).

A jig held two reed switches near the extremities of the recorder trace above the recorder pen, and a magnet was fixed to the pen. The reed switches were connected in parallel with a toggle switch and a timer input, as shown in figure 37. The timer was a Panax type T.300 mains frequency controlled, and was switched on when the input was short-circuited. The reed switches close for about 2 secs when the magnet passes beneath.

When the pen passed beneath the first reed, the timer switched on and the toggle was manually closed. Hence when the first reed opened again the timer stayed on. When the pen was directly under the second reed, (i.e. second reed closed), the toggle was opened, and the timer switched off by the second reed opening. The reverse procedure was carried out in cooling. Although this system is only semi-automatic, it is 100% reliable and completely flexible.

Heating and cooling times can thus be measured to $\pm$ 0.01 secs. There is no need to wait for the absorber to attain equilibrium, alternate heating and cooling slopes can be measured at will. Neither is there any need for sensitivity measurement or normalisation. Results are shown in Table 12.

Time to obtain result = 20 mins.

Table 13 summarises the above results.

Table 13

Date 28.6.67.

Method	Beam Power (μW)	Beam energy (ergs per monitor unit x 10^4)	Time to obtain result (mins)
Kinetic	230.0 ± 2.1	10.26 ± 0.07	240
Semi-adiabatic	235.2 ± 0.8	10.35 ± 0.04	120
Temperature rise after a fixed time	232.4 ± 0.6	10.32 ± 0.03	120
Thermal cycling	231.8 ± 1.2	10.28 ± 0.03	20

The error quoted above is the standard deviation on the arithmetical mean. When the results obtained in μW are normalised by the monitor the divergence of the result using the semi-adiabatic method is removed. The method of thermal cycling is considered to be the best for the following reasons.

1. The standard deviation obtained on the mean is comparable with other methods.
2. The time taken to record and analyse results is much shorter.
3. There is no subjective error introduced by this particular method of measuring heating and cooling times, a digital output is obtained.

The limitation of this method, as it was used, is that monitor integration times had to be measured by a stopwatch. A facility allowing the monitor to be integrated over the actual measured time of the X-ray heating, should reduce random errors in the system.

Table 14

Powers of various X-ray beams in microwatts

Date	10kV 30mA	15kV 30mA	20kV 25mA	25kV 15mA	30kV 10mA	30kV 25mA
12.6.67	7.024	41.18	85.59	93.77	89.72	238.8
13.6.67	7.007	41.39	85.45	94.49	90.23	237.8
27.6.67	6.768	38.69	83.22	92.80	86.48	233.7
6.7.67	6.767	39.53	84.73	93.98	88.94	235.8
12.7.67	6.815	39.65	84.00	91.73	88.17	235.3
Average	6.876 ± 0.058 (± 0.84%)	40.09 ± 0.52 (± 1.30%)	84.60 ± 0.46 (± 0.54%)	93.35 ± 0.49 (± 0.52%)	88.71 ± 0.66 (± 0.74%)	236.3 ± 0.9 (± 0.38%)

Table 15

Measurements of various X-ray beams in ergs per monitor unit (x 10^{-4})

Date	10kV 30mA	15kV 30mA	20kV 25mA	25kV 15mA	30kV 10mA	30kV 25mA
12.6.67	3.117	5.742	7.431	8.842	10.07	10.26
13.6.67	3.097	5.777	7.564	8.965	10.21	10.28
27.6.67	3.095	5.698	7.550	8.943	10.17	10.32
6.7.67	3.079	5.786	7.597	9.028	10.20	10.30
12.7.67	3.125	5.755	7.536	8.881	10.13	10.23
Average	3.103 ± 0.008 (± 0.26%)	5.752 ± 0.016 (± 0.28%)	7.546 ± 0.019 (± 0.25%)	8.932 ± 0.033 (± 0.37%)	10.16 ± 0.03 (± 0.30%)	10.28 ± 0.02 (± 0.19%)

6.4 Energy fluence measurements of various X-ray beams

Tables 14 and 15 show the reproducibility of calorimetric measurements on different days obtained by the method of thermal cycling. The defining aperture ($^3/16$ ins. diameter) and the calorimeter were removed between each observation. The X-ray tube was moved and the monitor chamber fixing device was screwed out of the tube head on various occasions. Comparison of these two tables shows the reduction in scatter produced by normalisation by the monitor unit. The standard deviation on the mean of the five observations is about $\pm$ 0.25% in each case.

Systematic errors arise from two sources. Firstly the error involved in the backscatter correction is estimated in 5 - 6, and secondly the error in the electrical calibration is given in 3.3 as $\pm$ 0.25%. Table 16 shows the average response for each of the above beams with the estimated fraction of energy backscattered included in the results. The root mean square error of random and systematic errors has been quoted with these results.

Table 16

kV mA	Response in ergs per monitor unit (x 10^{-4})	% error
10kV 30mA	3.103 $\pm$ 0.011	0.36
15kV 30mA	5.781 $\pm$ 0.023	0.39
20kV 25mA	7.652 $\pm$ 0.035	0.46
25kV 15mA	9.075 $\pm$ 0.049	0.54
30kV 10mA	10.33 $\pm$ 0.06	0.56
30kV 25mA	10.45 $\pm$ 0.05	0.51

6.5 Limitations and possible improvements

The largest source of error in the above results is due to uncertainties in the spectral distributions. Various distributions peaking at different energies were used to estimate these errors. A programme of work is at present being carried out to estimate these spectra more accurately.

The two factors which can limit the sensitivity of a calorimeter are noise and thermal drift, and the latter is the dominant factor in this system. The smallest power measured corresponds to an intensity of 1.75 μ watts per cm^2 at the absorber. A temperature drift rate of $10^{-4}{}^{o}C$ per min was always obtainable. This is equivalent to an input power of 0.1 μW, corresponding to an intensity of 0.025 μW per cm^2 at the absorber. Therefore intensities of less than 1 μW per cm^2 could probably be measured with this system. By using a liquid nitrogen bath, radiation heat losses could be greatly reduced as shown (2.4.4), and the thermal time constant would increase. Thermal matching of the absorbers is difficult due to their small size, and a double window calorimeter may provide a better matched thermal environment for the two absorbers.

CHAPTER 7

IONIZATION DOSIMETRY

7.1 Introduction

When X-rays interact with a gas their energy is transformed into the kinetic energy of moving electrons, and it is these electrons which ionize the gas. The number of ions produced by the direct action of X-rays is small compared with those produced by these secondary electrons.

In photoelectric interactions the X-ray energy goes into the kinetic energy of ejected photoelectrons, and into the potential energy of the excited atoms remaining. These excited states are short lived, anddecay with the emission of Auger electrons or X-rays characteristic of the gas. A Compton interaction in the low energy X-ray region, results in only a small fraction of the incident photon energy being transferred to the recoil electron. However these recoil electrons, together with photoelectrons and Auger electrons may subsequently lose their energy in the formation of ions, or in the excitation of atoms. Classically scattered X-rays are eventually absorbed by one of the above processes, assuming that the dimensions of the absorbing volume of gas are sufficiently large.

There is a minimum energy that an electron must have in order to ionize an atom. This is the ionization potential I of the atom in question, and equal to the binding energy of the outermost electron shell. Electrons with energy less than I, lose their energy in processes other than ionization. This energy, together with energy going into the excitation of atoms, constitute 'wasted' energy from the point of view of ion yield. Hence $\bar{W}$ (the average energy required to produce an ion pair) is always greater than I.

7.2 The choice of argon

Non-electronegative gases are those in which the probability of electron attachment to form a heavy negative ion is small. Argon is such a gas, and thus the chances of columnar recombination are small and saturation is usually achieved very quickly. Argon has a relatively high photoelectric cross-section in the low energy X-ray region, and thus total absorption may be possible. This together with its inertness, cheapness and availability make it ideal for this ionization chamber work.

It has long been known (39) that small amounts of impurities can appreciably lower the $\bar{W}$ value of a gas, and in argon this is due to metastable levels in the atom at 11.6 eV and 14 eV. These have sufficient lifetime to allow collisions to occur between them and the contaminating gas, resulting in possible ionization of the contaminating gas. Table 17, reproduced in part from Hurst, Bortner and Glick (39) shows that the most likely contaminants have little effect on the $\bar{W}$ values for α particles in argon.

Table 17

Gas	MIN $\bar{W}$ for mixture of argon and gas (eV)	$\bar{W}$ for pure gas (eV)
Argon	26.4	26.4
Carbon dioxide	26.0	34.5
Hydrogen	No effect	37.0
Nitrogen	No effect	36.6
Oxygen	26.0	32.2
Water	25.2	37.7

The argon used was commercially produced by British Oxygen, and quoted as

99.995% pure. No elaborate purification was undertaken, but the argon was passed through silica gel to remove any water vapour. Various cylinders of gas were used to see if consistent results were obtained.

7.3 Theoretical evaluations of $\bar{W}$

Theoretical evaluation of $\bar{W}$ has been carried out for hydrogen and helium. Initial calculations predicted a correlation between $\bar{W}$ and I which was not supported by experimental results. Fano (40), by evaluating an effective atomic number of hydrogen and helium (by considering electron screening), removed this correlation, and by using Fano's data Erskine (41) carried out an adequate theoretical evaluation of $\bar{W}$ for the case of pure helium. Theoretical analysis of higher atomic number gases, or gases which are not pure, is not possible at present. Valentine and Curran (42) have reviewed theoretical and experimental work on the evaluation of $\bar{W}$.

7.4 $\bar{W}$ values for argon by other workers

One of the first measurements of $\bar{W}$ argon was carried out by Lehmann (43) in 1927. Very low energy electron beams were used (less than 1 keV), and the difficulties of working with such radiation must have been considerable. A measurement was made of the electron current by using a Faraday cup, and the saturation ionization current by a total absorption ionization chamber. His result (33eV) was high compared with the more or less accepted value today.

The ratio of the $\bar{W}$ values of various gases can be found without the need to determine absolutely the energy in a radiation beam. Argon has often been used as a standard in these measurements. Gaertner (44, 45) used two ionization chambers in series, the second was filled with argon and the first with the gas under observation. Saturation measurements

were made in both chambers for various pressures in the first chamber, and by extrapolation the ratio $\frac{\bar{W}\ \text{gas}}{\bar{W}\ \text{argon}}$ was obtained. ($\frac{\bar{W}\ \text{air}}{\bar{W}\ \text{argon}} = 1.232$ for 9keV X-rays). The pressure in the chambers was kept low to ensure complete saturation in the current measurements. Gaertner (46) finally carried out an absolute measurement by using a thermocouple to determine the energy in the beam. His result was $\bar{W}$ argon = 28.4 $\pm$ 0.5eV.

Similar work was carried out by Crowther and Orton (47) and by Wilhelmy (48). Crowther and Orton used a high pressure ionization chamber irradiated with copper K_α X-rays obtained by crystal diffraction. This was almost complete absorption, only a small correction had to be applied, and their results gave $\frac{\bar{W}\ \text{air}}{\bar{W}\ \text{argon}} = 1.32$. Wilhelmy used low energy X-rays (2 - 3 keV), a lower energy than the K-edge of argon, so no correction was necessary for escaping energy. However he only used a galvanometer for current measurements. He quoted $\frac{\bar{W}\ \text{air}}{\bar{W}\ \text{argon}} = 1.309$, and found that $\bar{W}$ air varied in the range investigated.

The last of these earlier measurements was by Gerbes (49) in 1937. He measured $\bar{W}$ argon for homogeneous electron beams and his results are

	10 keV	40 keV
$\bar{W}$ argon	27.3	25.2

These show a large variation between the two energies, while most recent results point to the energy independence of $\bar{W}$ argon.

The determination of $\bar{W}$ values in general seemed to lapse until 1952. The tendency then was to determine $\bar{W}$ values for radiation other than electron or X-ray beams, and an interest was shown in the effect of impurities in gases. $\bar{W}$ argon had not been fixed, and the remarkable decrease in $\bar{W}$ values for small amounts of impurities cast doubt on earlier measurements.

Good agreement was found by various workers for the ionization of argon by α particles. These are summarised in Table 18.

Table 18

Workers	Year	$\bar{W}$ argon for α particles
Sharpe	1952	26.3
Valentine and Curran (50)	1952	25.9
Jesse and Sadauskis (51)	1953	26.4
Haeberli, Huber and Baldinger (52)	1953	26.25
Bortner and Hurst (53)	1954	26.4
		Average 26.25 ± 0.1

The method used by Bortner and Hurst (53) is typical. An α particle source was electroplated on platinum and enclosed in a high pressure ionization chamber, so that the range of the α's was completely inside the chamber (this was even possible with hydrogen and helium). The source was calibrated by pulse height discrimination with a methane proportional counter. The Jaffe theory (8 - 1) was used to evaluate the extrapolation saturation current.

Due to the uncertainty in $\bar{W}$ air values up to 1962 (I.C.R.U. report 1962), calorimetric measurements were concerned with determining $\bar{W}$ air. Goodwin (12), and Reid and Johns (54) carried out two such determinations for Cs^{137} radiation. Earlier Laughlin, in similar work, did a parallel experiment with argon, and found $\bar{W}$ argon = 23.0eV (private communication

to Binks (55) in 1954). A large correction had to be applied for energy lost from the ionization chamber, and may account for this low value. Binks reports that $\bar{W}$ is constant in the range 1 keV to 1 MeV and equal to 27.0 $\pm$ 10% eV.

7.5 Other methods of determining $\bar{W}$

7.5.1 Proportional counter

The count rate of a particular source can be determined by using a proportional counter. If the applied voltage is then reduced below a value at which gas multiplication occurs, the saturation ionization current can be measured. Curran, Cockcroft and Insch (56) first described the above technique. This was improved by Valentine (57) who experimented with A^{37} X-rays and tritium β-rays, and found $\bar{W}$ argon = 27.0 eV.

A similar technique was used by Phipps, Boring and Lowry (58), who measured $\bar{W}$ argon for heavy ions in the energy range 8 to 100 keV. Heavy ions showed a distinct variation of $\bar{W}$ with energy, while $\bar{W}$ for the lighter ions seemed to approach (at high velocities) a common value in the region of 26.4 eV.

The main advantage of this technique is that the geometry is the same in determining the count rate and the saturation ionization current, so there is no correction to apply for energy loss due to scatter.

7.5.2 Scintillation counters

Bunde, Lang, Pohlit and Sewkor (59) described a total absorption ionization chamber which was capable of totally absorbing 9 keV X-rays in air. This chamber was two metres in length and initially used to determine μ for air in the low energy X-ray region. The monochromatic X-ray beam was

Figure 38

EXTERNAL VIEW OF IONIZATION CHAMBER

(brass construction)

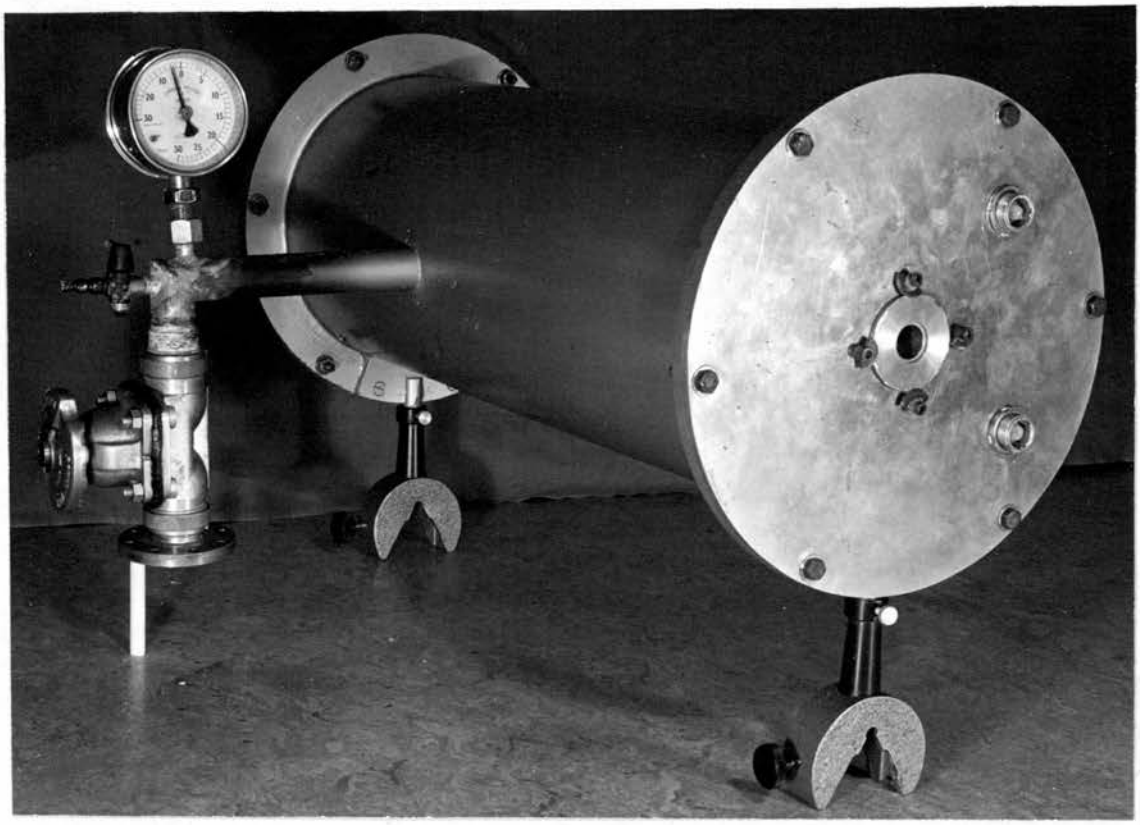

produced by a filter difference method. Rajewsky and Lang (60) then used a totally absorbing caesium iodide scintillation counter to determine the number of monochromatic X-ray photons, and compared this result with that of the total absorbing ionization chamber, hence determining $\bar{W}$ values for air.

7.5.3 $FeSO_4$ dosimetry

$\bar{W}$ values for 2 MeV X-rays from a Van der Graaff generator using $FeSO_4$ and ionization chamber dosimetry were determined by Weiss and Bernstein (61). Using a previously determined G value for the $FeSO_4$ solution of 15.45 $\pm$ 0.15, $\bar{W}$ argon was found to be 25.5 eV. They however, stated that argon was highly subject to impurities and repeated their experiment with purified argon. $\bar{W}$ argon was then quoted as 25.8 eV (62).

It appears that $\bar{W}$ argon for α particles is well established at 26.25 eV per ion pair, as shown by Table 18. Valentine and Curran (50) concluded that the value of $\bar{W}$ for electrons was identical - within experimental error - to that for polonium α particles. This conclusion, which is supported by Jesse and Sadauskis, probably gives the most reliable $\bar{W}$ value for electrons in argon.

7.6 Design of the ionization chamber

7.6.1 Chamber

The chamber is cylindrical in shape, approximately 60 cm in length and 23 cm in diameter. An external view is shown in figure 38. The ends of the chamber are flanged, and end plates are 'O' ring sealed and bolted to these flanges. Windows are centrally mounted in these end plates, and consist of 0.025 mm aluminized 'Melinex'. The rear window is flush with

Figure 39

ELECTRODE ASSEMBLY

(aluminium construction)

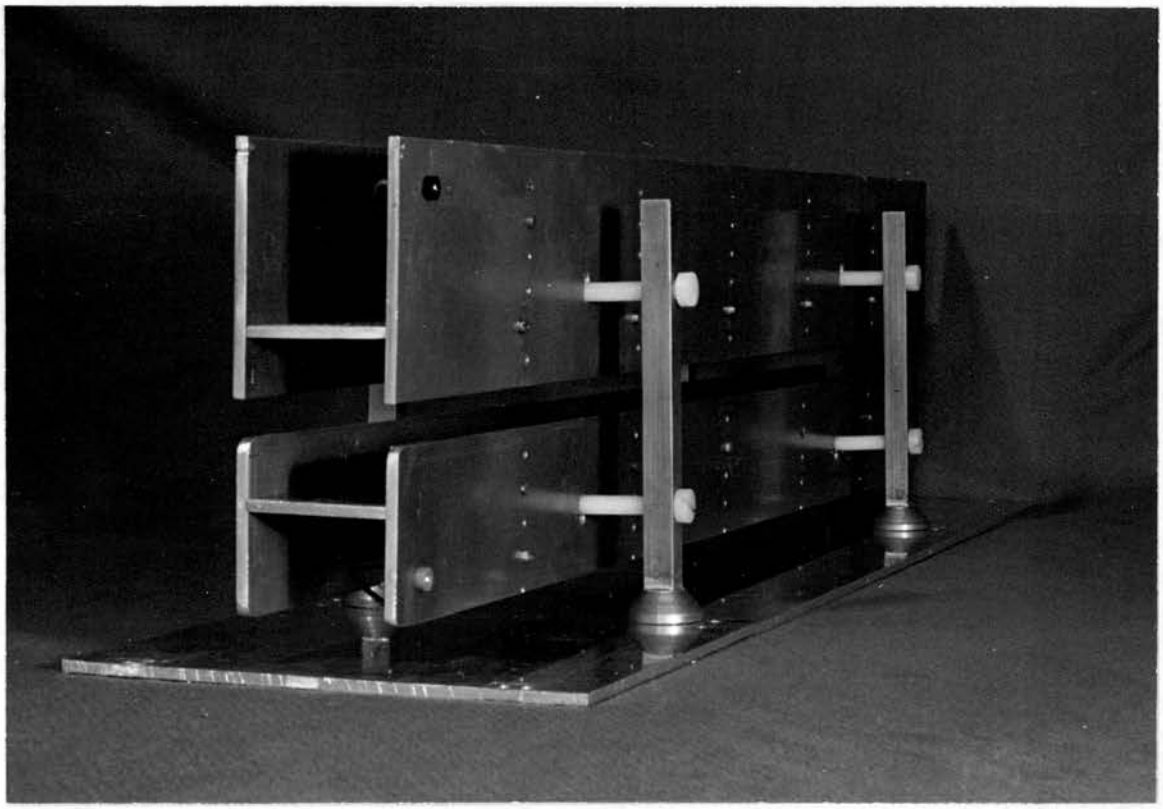

Figure 40

WINDOW INSERT

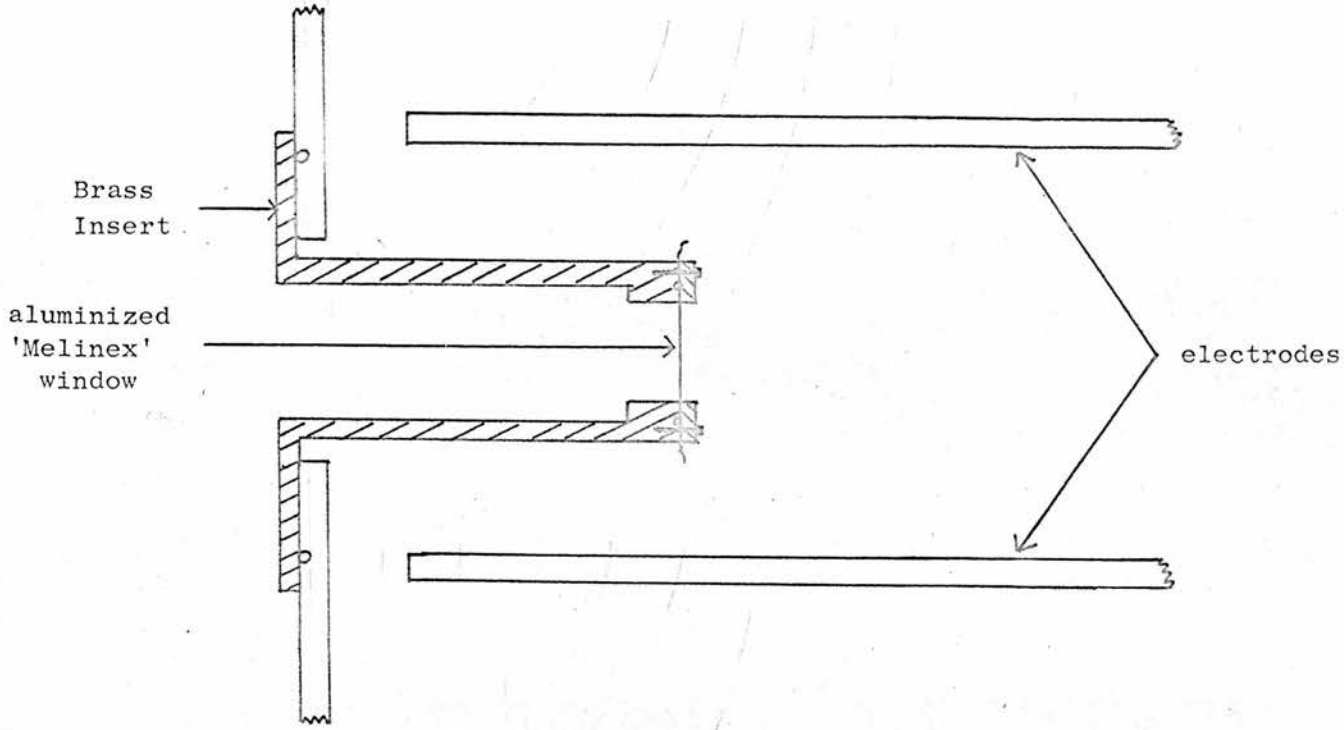

Figure 41

FIELD CONFIGURATION IN THE FRONT REGION OF THE IONIZATION CHAMBER

(a) Without window insert

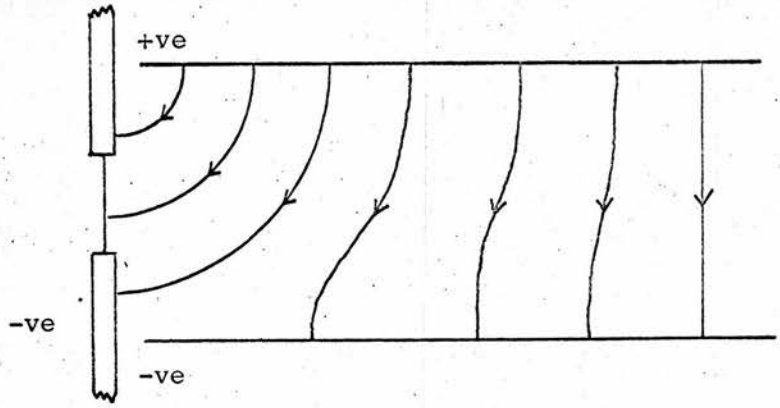

(b) With window insert

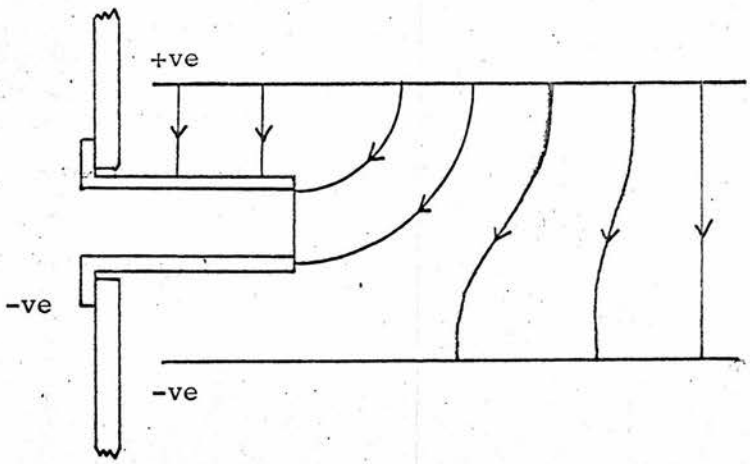

the end plate, and again sealed with a conventional 'O' ring.

Evacuation of the chamber is possible through the connection shown, and this connection may be sealed by a vacuum valve. Argon is admitted through a gas tap which has been ground to provide a vacuum and pressure seal. Electrical connections are made through the front plate by pressurised 'Plessey' connections, and then to the electrodes.

7.6.2 Electrode assembly

The electrodes are H shaped and mounted vertically one above the other as shown in figure 39. The vertical separation can thus be easily varied, but lateral separation can only be varied by replacing the horizontal plate. Throughout the following measurements the plate separation was kept to a minimum so that a maximum field strength would be obtained. This was 4 cm in both directions.

The base plate shown slides into the chamber on two rails and is secured into position. The four stands fixed to this base plate have nylon screws passing through holes in them, and screwing into the electrodes. Thus there is a four point support for each electrode, and a lateral movement of the electrodes can be obtained by these screws.

7.6.3 Front window

A high percentage of the ionization produced in the chamber will occur in the front region, and thus the field configuration in this region is very critical. For this reason the front window was set back inside the chamber by means of the insert shown in figure 40. The insert is 'O' ring sealed to the front end plate, and the window also sealed by means of an 'O' ring as shown.

The change in the field configuration in the front region is shown

FIGURE 42

COMBINED INTEGRATING CIRCUIT FOR MONITOR AND IONIZATION CHAMBERS

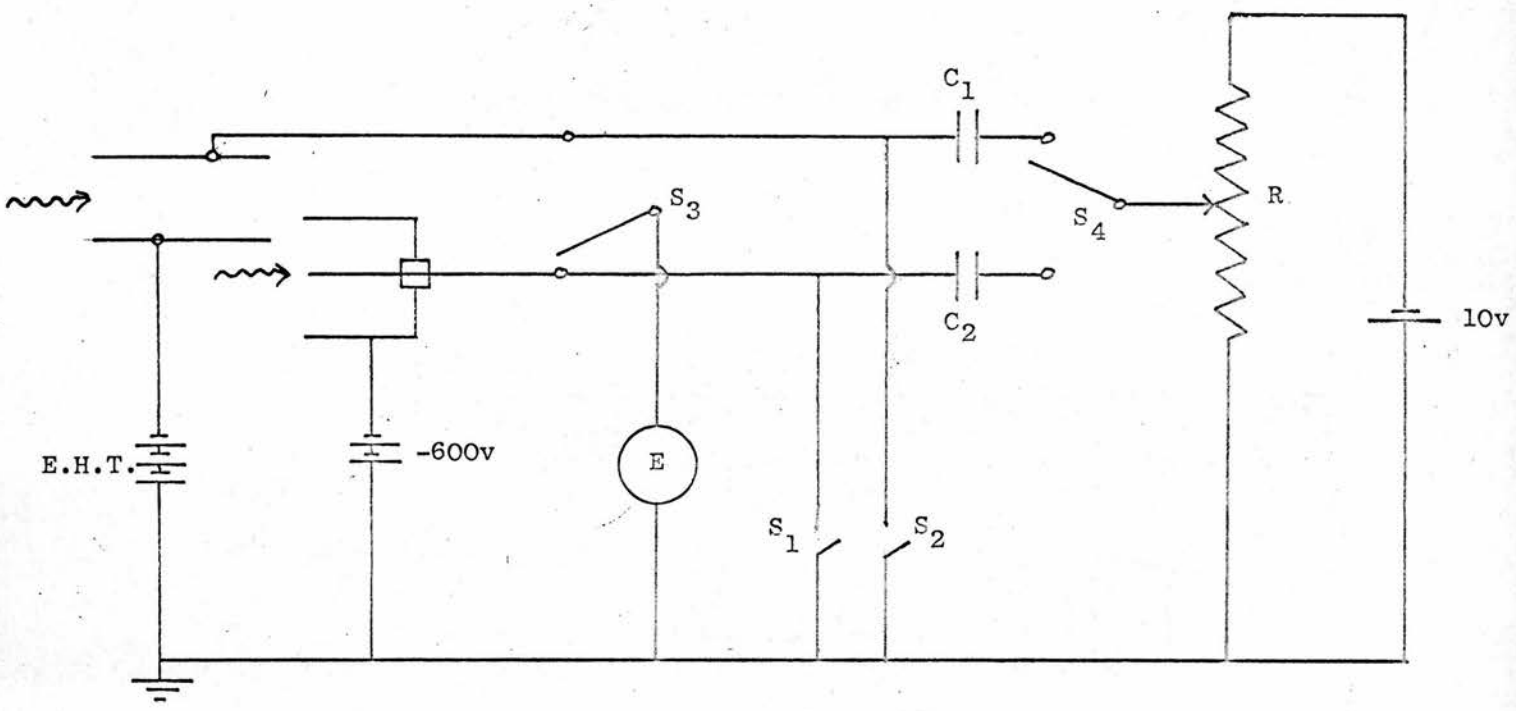

E - electrometer

R - 10KΩ decade box

C_1 - integrating capacitor for ionization chamber

C_2 - integrating capacitor for monitor chamber

S_1 and S_2 - discharging switches

S_3 - connects electrometer to either capacitor

S_4 - supplies standardised voltage to either capacitor

in figures 41(a) and (b). Figure (a) shows the field without the insert, and figure (b) the field with the insert. A higher field has thus been produced in the region close to the window.

7.7 Experimental situation

The ionization chamber is positioned in a similar manner to the calorimeter as described in 2 - 6. It rests on the optical bench by means of two saddles, and as the chamber is mainly operated with the case at E.H.T., these saddles are insulated from the bench by 'Melinex'. Trouble was experienced from time to time due to breakdown of the E.H.T. (up to 4000 volts) both outside and inside the chamber. Positioning of the electrodes and of the chamber was therefore very critical.

The chamber is evacuated by a rotary pump, filled with argon, re-evacuated and again filled with argon to the required pressure. A fluorescent screen is placed in the rear window, and the chamber adjusted until the transmitted beam is central on the window. The currents measured were of the order of 10^{-7} amps, and no need was found to screen any of the leads to the chamber.

7.8 Measuring circuit

The current obtained from the ionization chamber was integrated by the same circuit as used for the monitor (figure 33). The monitor and ionization chamber circuits were actually built into one as shown in figure 42, and are designed so that only one backing off voltage and one electrometer are required. The electrometer can look at the voltage build up on either capacitor by means of switch 3. Integration takes place on capacitors C_1 and C_2, and switches 1 and 2 respectively allow them to be discharged. The

monitor and the ionization chamber currents can thus be integrated for the same arbitrary time. Chamber readings are immediately normalised by the monitor readings, and a response in $\frac{\text{volts}}{\text{m.r.}}$ obtained.

Figure 43

RELATIONSHIP BETWEEN IONIZATION CURRENT AND APPLIED VOLTAGE

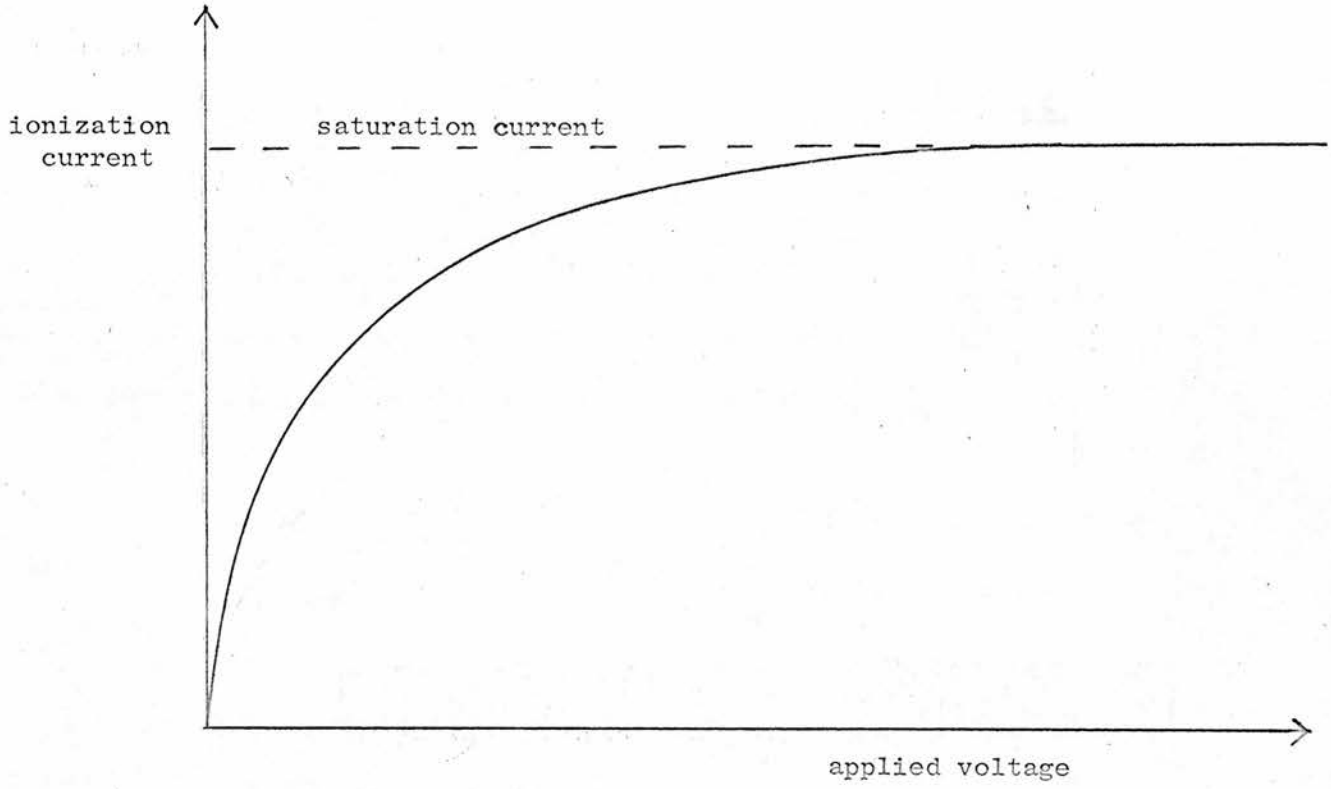

Figure 44

EFFECT OF SPACE CHARGE

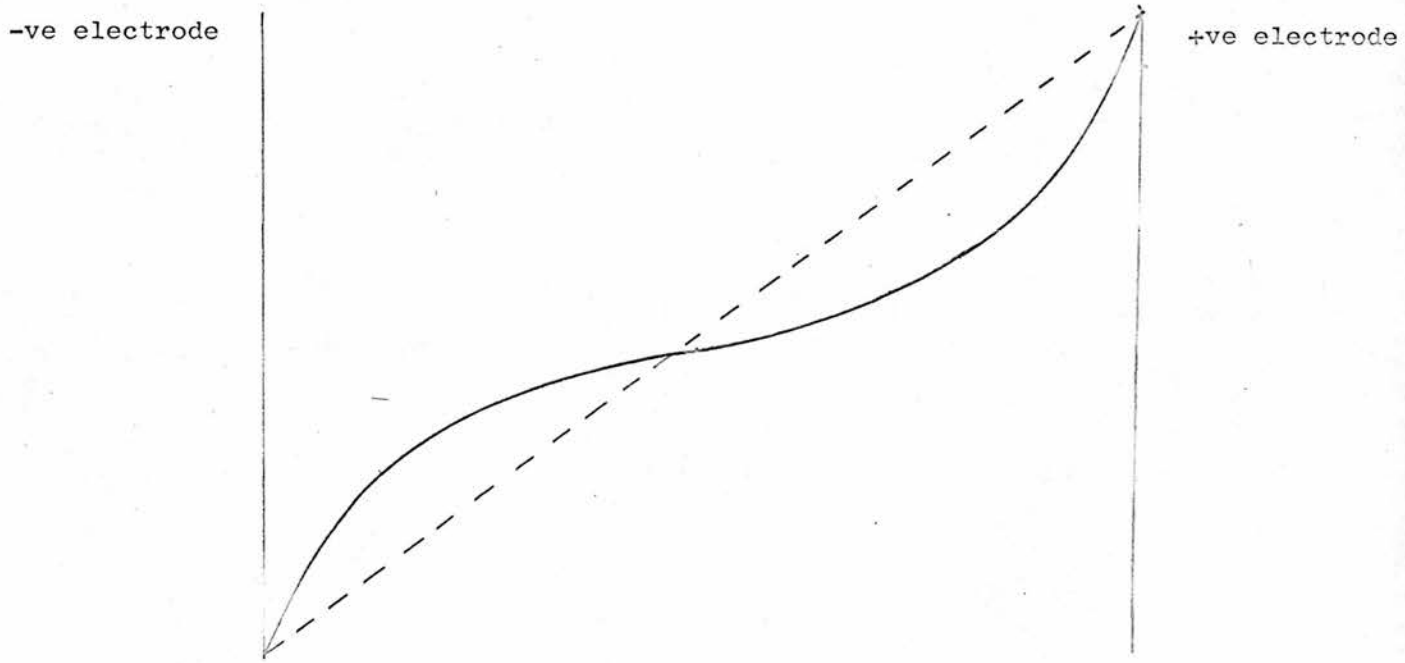

CHAPTER 8

SATURATION OF THE IONIZATION CHAMBER

8.1 Processes which prevent saturation

The relationship between the ionization current and the applied voltage in an ionization chamber is shown in figure 43. The current increases with applied voltage until at large voltages it becomes constant. The applied voltage is then large enough to collect all the ions formed, and the saturation current is obtained. There are three effects which result in the lack of saturation at lower voltages.

8.1.1 Diffusion

Ions, when present in a gas, exhibit the random Brownian motion of the gas molecules. They may diffuse to and be collected by the electrode of opposite charge, inspite of the electric field present. However diffusion losses will rarely need to be taken into account in practical ionization chambers (Boag (28)).

8.1.2 Space-charge effects

The movement of ions to their respective electrodes may alter the distribution of the field near to these electrodes. Near to the positive electrode there will be a surplus of negative charge; and near the negative electrode a surplus of positive charge. If the ions have different mobilities then these twospace charge effects will differ. The potential gradient will change rapidly close to the electrodes, and may be as shown in figure 44. Thus space charge effects effectively lower the applied voltage to the chamber.

8.1.3 Recombination

This is the process by which ions of opposite sign recombine with

each other, and is by far the major problem in the loss of ion collection. There are two types of recombination.

8.1.3.1 Initial Recombination

This takes place when the recombining ions are formed in the same electron track, and depends on the density of ionization along this track. It is thus independent of dose rate. The magnitude of this process, apart from depending on the field strength, will depend on the type and energy of the radiation. Thus ionization by α particles would produce more initial recombination than would ionization by X or γ-rays.

Two theories explaining initial recombination have been put forward. Jaffe (63), when working with α particles in 1913, postulated a columnar theory, which assumed that the ion distribution was cylindrically symmetrical about the particle track. Experimental results agreed with theory for α particles, but did not agree when the theory was applied to X and γ-rays. However Lea (64) in 1934 put forward a cluster theory in which the ions are considered to be localised along the tracks of the secondary electrons. The cluster theory is applicable until adjacent clusters overlap when the columnar theory can be applied.

A mathematical analysis put forward by Kara-Michailova and Lea (65) in 1940, states that when initial recombination is present the saturation current can be obtained by extrapolation. The equation they give is

$$i_{sat} = i + (\text{const} \times i_{sat}) \times \frac{i}{E} \qquad \ldots\ldots\ldots 8 - 1$$

where i is the measured ionization current at a field strength E ($^{\text{volts}}/_{\text{cm}}$). For large values of E, a plot of i against $\frac{i}{E}$ can be extrapolated to $\frac{i}{E} = 0$ to give i_{sat}.

8.1.3.2 Volume Recombination

Volume recombination takes place between ions which do not originate in the same electron track, and hence occurs when the ions have diffused apart. It is therefore dependent on dose rate which will determine the number of electron tracks per unit volume. At high dose rates it is by far the major process of recombination. Two theories of note explaining volume recombination have been put forward. From the work of Mie (66) in 1904, the following expression may be deduced,

$$i_{sat} = i + \text{const} \times \frac{i}{E^2} \qquad \ldots\ldots\ldots 8 - 2$$

and a plot of i against $\frac{i}{E^2}$ should give a straight line, from which i_{sat} is obtained.

From the work of Boag and Wilson (67) a similar expression is obtained, from which it can be shown that

$$i_{sat} = i + \frac{\text{const}}{i_{sat}} \times \frac{i^2}{E^2} \qquad \ldots\ldots\ldots 8 - 3$$

and now a plot of i against $\frac{i^2}{E^2}$ gives i_{sat}.

Greening (68) reviews these theories and compares them with extensive experimental data for the case where air is the ionized gas. He concludes that Mie's theory is valid when ionization currents in excess of 0.7 of the saturation current are obtained, but that Boag and Wilson's theory is valid only very near to saturation.

Mie's equation (8 - 2) differs in form from that of Kara-Michailova and Lea (8 - 1) for initial recombination, only in the power of E. However, initial recombination will play an exceedingly small part in any recombination occurring in this experiment. It will be present, but its effect will be masked by general recombination due to the high dose rates

Table 19

Ionization chamber response to various
electrical modes of operation (in volts per monitor reading)

E.H.T. (volts)	1 (a)	1 (b)	2 (a)	2 (b)	3 (a)	3 (b)	4 (a)	4 (b)
1500	2.616	2.623	2.190	2.197	2.383	2.370	2.618	2.620
2000	2.612	2.613	2.356	2.363	2.477	2.471	2.618	2.622
2500	2.617	2.622	2.451	2.455	2.521	2.523	2.620	2.621
3000	2.621	2.623	2.497	2.504	2.550	2.554	2.619	2.615
3500	2.614	2.615	2.530	2.538	2.544	2.549	2.613	2.619
4000	2.614	2.612	2.541	2.548	2.529	2.531	2.617	2.616
Response	2.616	2.618					2.618	2.619

Figure 45

SCHEMATIC REPRESENTATION OF THE VARIOUS ELECTRICAL MODES OF OPERATION OF THE IONIZATION CHAMBER.

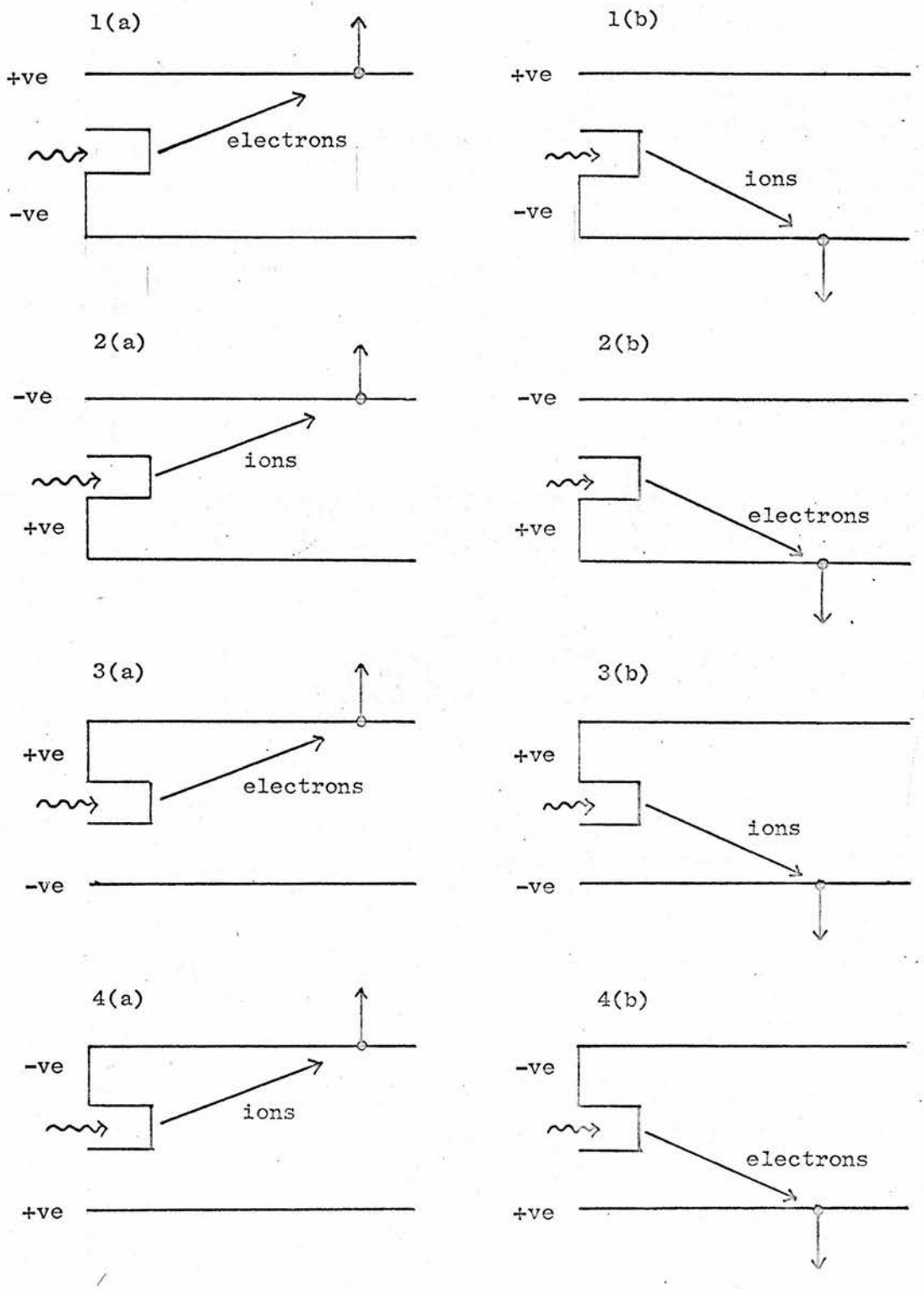

involved. Mie's equation (8 - 2) is also to be preferred to that of Boag and Wilson (8 - 3), because of the greater range of ionization currents over which extrapolation can be performed.

The above theories were developed for ionization of air, where molecular ions are produced. Argon is different in the fact that conduction is by positive ions and electrons. However, if extrapolation is required the validity of equation 8 - 2 for ionization in argon will be tested.

8.2 Different modes of operation of the chamber

8.2.1 Electrical

There are eight different modes of electrical operation of the ionization chamber, these are shown schematically in figure 45. In situation 1(a), the field removing the electrons to the upper plate is high, and as the electrons have a relatively high mobility (approximately 1000 x that of positive argon ions) saturation will be relatively easy. Assuming that the chamber is geometrically symmetric, then 4(a) would be expected to give the same result for ion collection. In situation 2(a) the field removing the electrons and the field removing the ions have been interchanged. Because of the relative low mobility of argon ions, saturation will not be as easy as in 1(a) and 4(a). Again assuming geometrical symmetry, 3(a) should give the same result for electron collection. Situations 1(b) to 4(b) are the exact complements of 1(a) to 4(a), and should yield identical results, that is 1(a) = 1(b) and so on.

Results are shown of the response from these various situations in Table 19. These are obtained with 20kV 25mA X-rays, and with a pressure of two atmospheres of argon in the chamber. Results are expressed in $\frac{\text{volts}}{\text{m.r.}}$ as explained in 7 - 8.

Figure 46

EXTRAPOLATION OF i AGAINST $\frac{i}{E^2}$ ACCORDING TO MIE'S THEORY

(DIFFERENT ELECTRICAL CONFIGURATIONS)

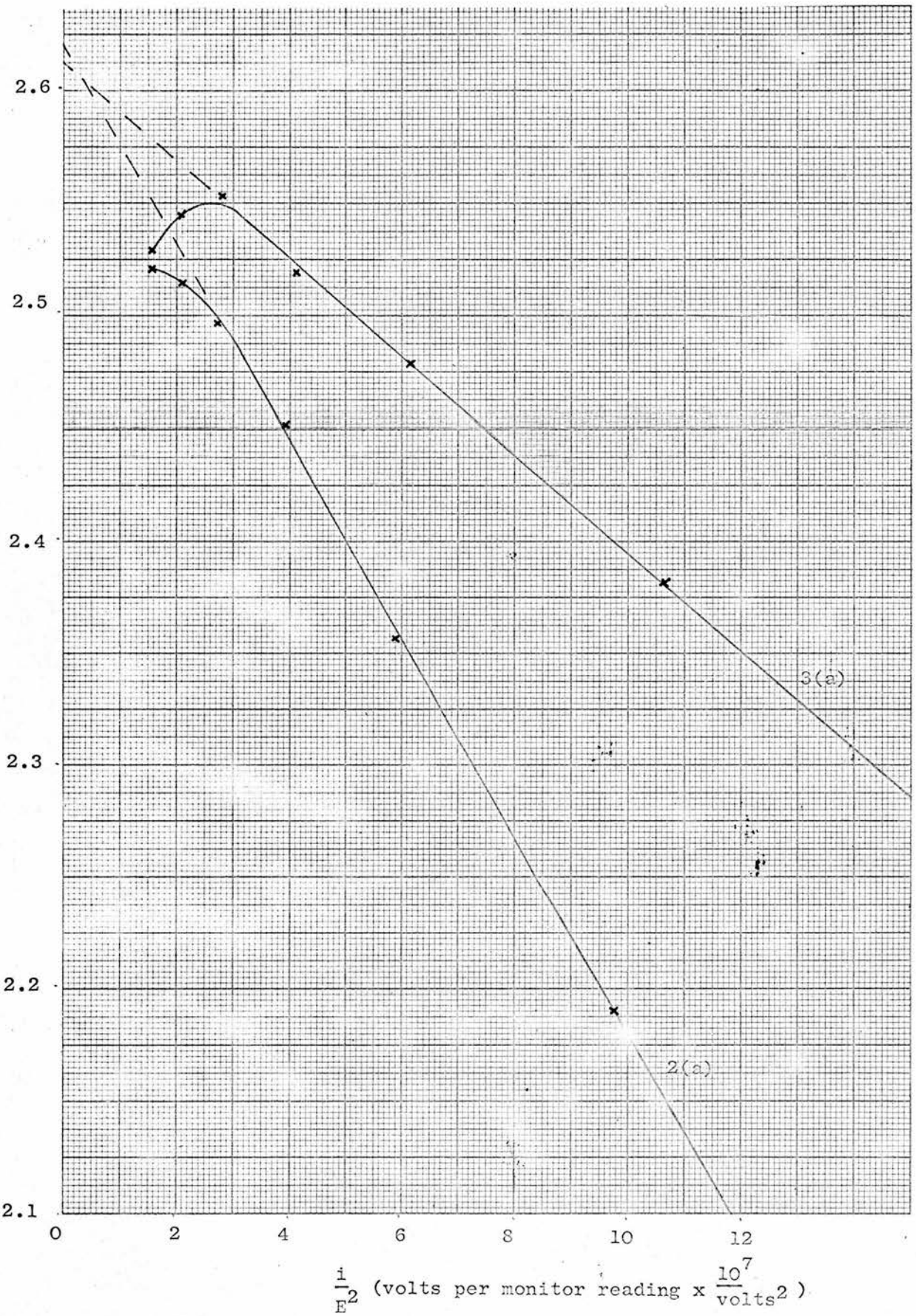

In situations 1(a), 1(b), 4(a) and 4(b) it appears that saturation has been achieved, and the same result is obtained in all cases. There is no evidence of a residual slope in the saturation plateau for a change from 1500 volts to 4000 volts in the applied voltage. In each of these situations electrons are removed by a high field.

In situations 2(a), 2(b), 3(a) and 3(b) saturation is never achieved. In all of these situations it is the ions which are being removed by the high field. A plot of i against $\frac{i}{E^2}$ according to Mie's equation (8 - 2) has been carried out. Results are plotted in figure 46 and shown in Table 20, for situations 2(a) and 3(a).

Table 20
(i in volts per monitor reading)

		2(a)		3(a)	
E.H.T. (volts)	$\frac{1}{E^2} \times 10^7$	i	$\frac{i}{E^2} \times 10^7$	i	$\frac{i}{E^2} \times 10^7$
1500	4.44	2.190	9.72	2.383	10.58
2000	2.50	2.356	5.89	2.477	6.19
2500	1.60	2.451	3.92	2.521	4.03
3000	1.11	2.497	2.77	2.550	2.83
3500	0.816	2.515	2.06	2.544	2.06
4000	0.625	2.521	1.59	2.529	1.58
	Extrapolated Response	2.620		2.613	

The plots of i against $\frac{i}{E^2}$ are linear between 1500 volts and 3000 volts, and the extrapolated results agree well with those obtained in Table 19. These results were obtained by drawing the best straight lines through the first four points; a more accurate method was not used because voltage settings were

not accurately determined, nor were they reproducible.

Situation 1(a) gave the same result as situation 1(b), and this was true for the remainder of the situations. However the results obtained in 2(a) and 2(b) are not the same as those in 3(a) and 3(b), a higher field must be present, that is the window is nearer the lower plate. On measurement this was found to be true.

Above 3000 volts a peculiar effect is observed. The current-voltage curve which was tending towards a saturation value, drops off in cases 2(a) and 2(b), and in 3(a) and 3(b) actually turns over. In all these cases ions are being removed by a high field. A satisfactory explanation of this effect has not been obtained.

The above procedure was carried out with all X-ray beams used, and it was similarly proved that the same result could be obtained no matter how the chamber was operated. However no results in $\bar{W}$ calculations were taken from extrapolated values. In situations 4(a) and 4(b) the outside of the chamber is used as a collecting electrode, and for this reason neither of these two methods were used. As situation 1(a) is electron collection, as opposed to ion collection in 1(b), the chamber was always operated in this manner in day to day comparisons with the calorimeter.

8.2.2 Geometrical

A different form of geometry was used in the critical window region, once again to see if the same saturation current was obtained. The window insert was replaced with a window flush with the front end of the chamber. Results obtained at 20 kV 25 mA (electrical conditions as in 1(a)) are shown in Table 21 and plotted in figure 47.

Figure 47

EXTRAPOLATION OF i AGAINST $\frac{i}{E^2}$ ACCORDING TO MIE'S THEORY

(DIFFERENT GEOMETRICAL CONFIGURATION)

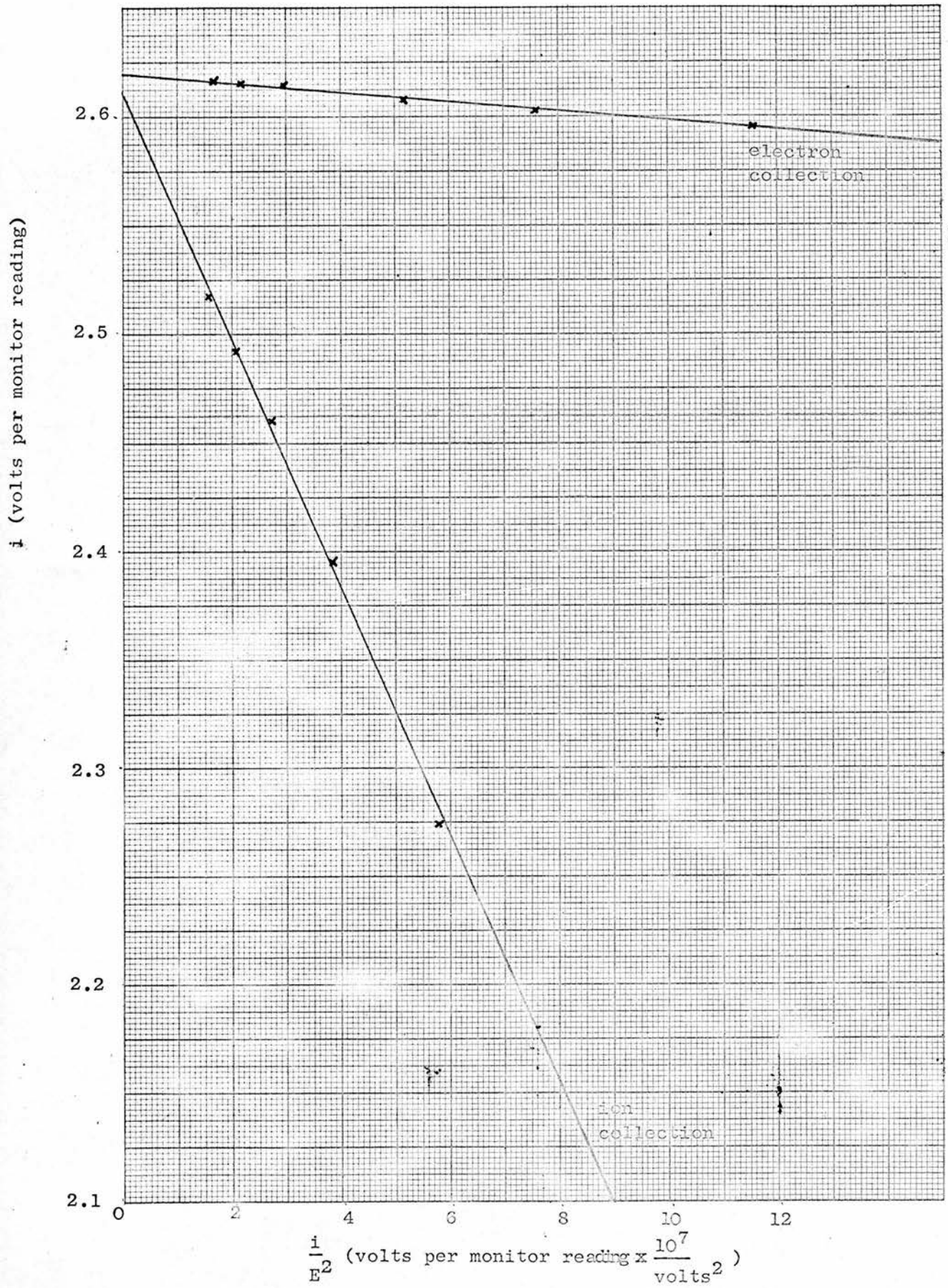

Table 21

(i in volts per monitor reading)

E.H.T. (volts)	$\frac{1}{E^2} \times 10^7$	Electron collection		Ion collection	
		i	$i/E^2 \times 10^7$	i	$i/E^2 \times 10^7$
1500	4.44	2.596	11.53	-	-
2000	2.50	2.606	6.52	2.274	5.69
2500	1.60	2.611	4.18	2.393	3.83
3000	1.11	2.614	2.90	2.459	2.73
3500	0.816	2.616	2.13	2.492	2.03
4000	0.625	2.617	1.64	2.519	1.57
	Extrapolated Values	2.619		2.610	

Saturation is not achieved in this case but extrapolated values agree with results previously obtained.

8.3 Scatter corrections for various chamber pressures

Scatter corrections were discussed in detail in Chapter 5. In these calculations the chamber was assumed to be 60 cm in length and having a 2 cm radial escape path. Sidescatter has been calculated by $\int_{\phi=0}^{\pi}$ (5 - 3). The effect of $\int_{\phi=0}^{\frac{\pi}{2}}$ will be discussed in 9 - 5. Equations 5 - 8, 5 - 10, 5 - 16 and 5 - 18 were used to calculate the individual energy losses. Allowance was then made for lack of total absorption (scatter losses would appear too large if total absorption was wrongly assumed). $\frac{\mu}{\rho}$ values for argon were by Stainer (35); σ (coherent + incoherent) were by McGinnies (38).

Figure 48

VARIATION OF $\Delta\mathcal{E}$ % WITH CHAMBER PRESSURE FOR VARIOUS INCIDENT X-RAY ENERGIES

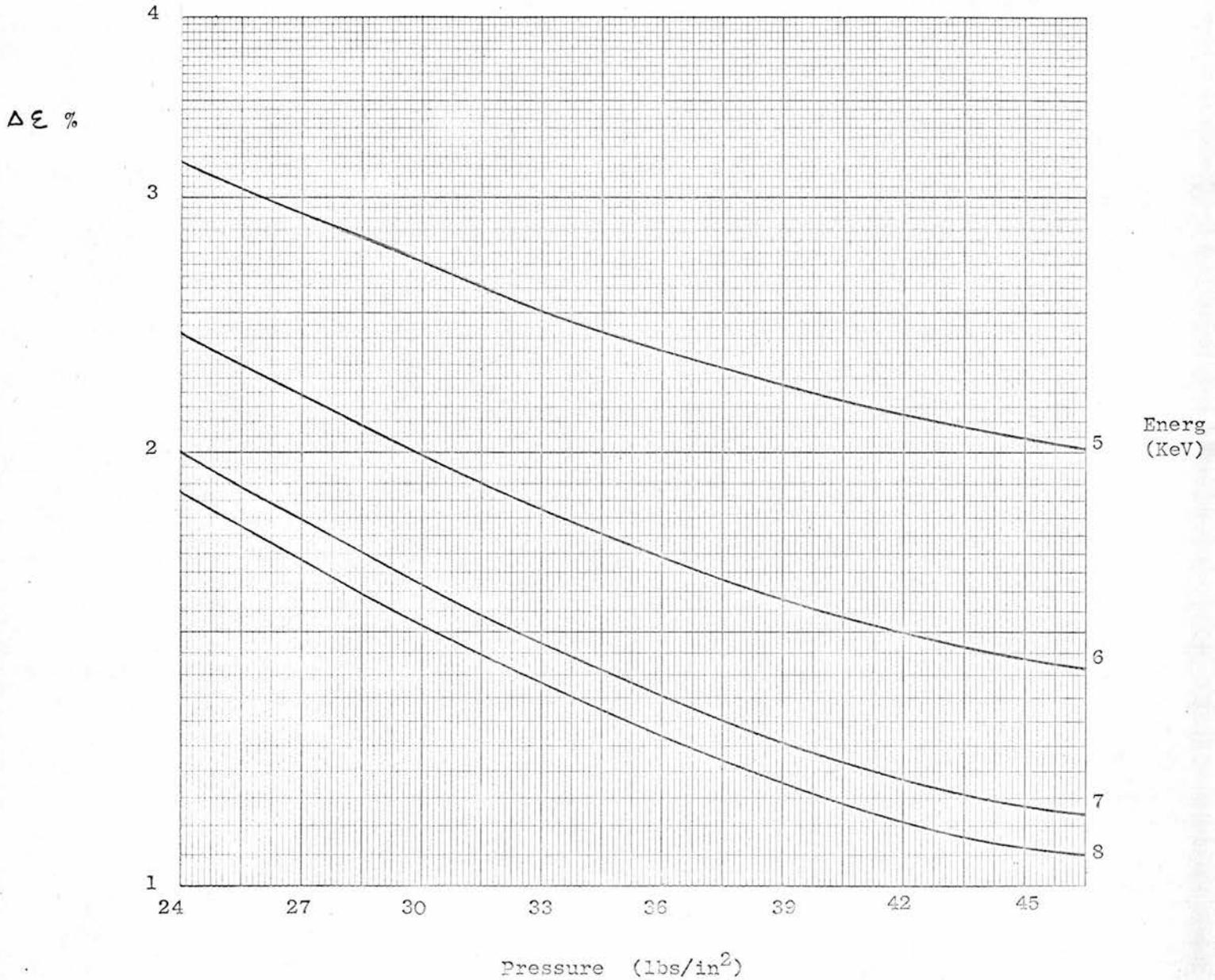

Figure 49

VARIATION OF $\Delta\varepsilon\%$ WITH CHAMBER PRESSURE FOR VARIOUS INCIDENT X-RAY ENERGIES

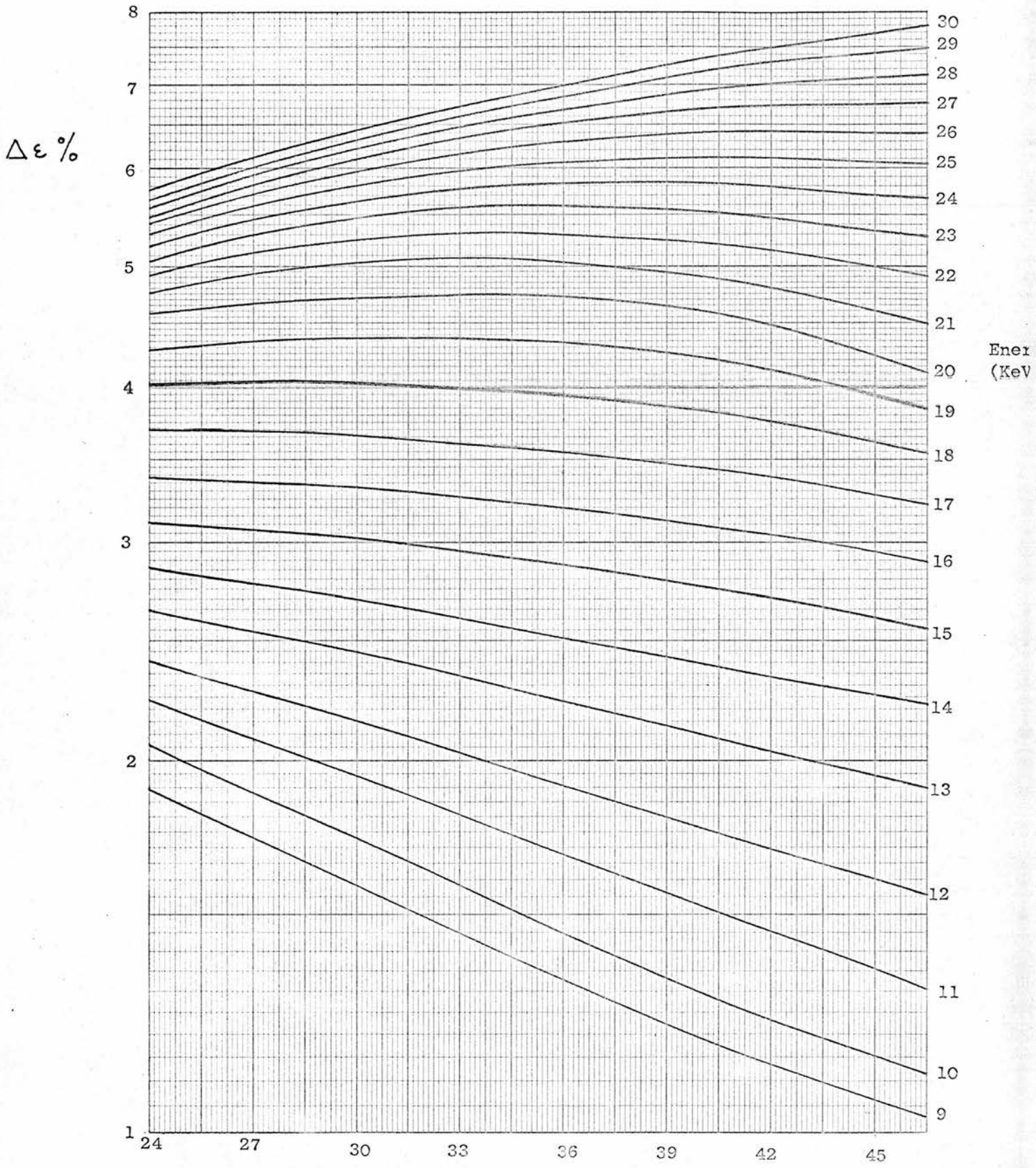

Other assumptions were

$\frac{\mu'}{\rho}$ for argon k_α radiation = 180 cm^2/gram.

$k\alpha$ radiation for argon = 3 keV.

ω_k for argon = 0.1

The total percentage energy lost ($\delta\varepsilon$) was evaluatedfor incident energies between 5 and 30 keV, and chamber pressures of 24 to 45 lb/in^2 (9 - 30 lb/in^2 above atmospheric). The results are summarised in figures 48 and 49. A calculation similar to that in 5 - 6 was now carried out for the 20 kV spectrum at various chamber pressures. Experimental results were also taken at these pressures and the corrections applied to see if the same result was obtained in each case. Results are shown in Table 22.

Table 22

(Response in volts per monitor reading)

Chamber Pressure lbs/in²	Response	% energy lost	Corrected Response
29	2.616	2.57	2.685
31	2.625	2.39	2.689
33	2.629	2.22	2.689
35	2.636	2.09	2.692
37	2.638	1.95	2.690

As expected, the response increases with pressure as scatter losses decrease. When the scatter correction is applied this increase disappears.

The ionization chamber has thus been shown to give the same value for the saturation current when operated at different argon pressures, and different electrical and geometrical configurations.

CHAPTER 9

$\bar{W}$ VALUES FOR ARGON FOR LOW ENERGY X-RAYS

9.1 Total absorption calculations

The method of ascertaining if a particular X-ray beam is totally absorbed in a medium was explained in 4 - 1. This calculation has to be repeated for the various beams used with the ionization chamber as it is by no means certain that total absorption will be achieved in argon. Measurements at 10kV, 15kV and 20kV were all taken at a pressure of 2 atmospheres of argon (29 lb/in^2); those at 25kV and 30kV at 3 atmospheres (45 lb/in^2). Calculations gave the results shown in Table 23.

Table 23

X-ray beam peak energy (kV)	Chamber Pressure (lb/in^2)	% energy lost by transmission
10	29	< 0.1%
15	29	< 0.1%
20	29	0.18
25	45	0.37
30	45	1.57

These corrections must be applied to each of the individual beams measured. No effort was made to fill the chamber to more than 3 atmospheres, as it was unlikely that the 'Melinex' windows would withstand any further increase in pressure. This was also the limit of the pressure gauge. A pressure of 2 atmospheres was used with the lower energy beams for ease of saturation, although total absorption and scatter corrections could be reduced by using a higher pressure.

9.2 Scatter corrections

Using figures 48 and 49 (Chapter 8), and the assumed spectra for the various beams, corrections were made for scattered radiation as explained in 8.3. These are as shown in Table 24.

Table 24

X-ray beam peak energy (kV)	Chamber Pressure (lb/in^2)	% energy lost due to scatter
10	29	2.10
15	29	2.01
20	29	2.57
25	45	2.28
30	45	2.86

Total corrections to be applied with their estimated uncertainties are then as shown in Table 25.

Table 25

X-ray beam peak energy (kV)	% correction	% uncertainty
10	+ 2.10	± 0.5
15	2.01	0.5
20	2.75	0.6
25	2.65	0.7
30	4.43	1.0

Table 26

Reproducibility of ionization chamber measurements on various days
(Response in volts per monitor reading)

Date	10kV 30mA	15kV 30mA	20kV 25mA	25kV 15mA	30kV 10mA	30kV 25mA
16.6.67	11.88	2.009	2.628	3.114	3.482	3.501
17.6.67	11.86	1.988	2.607	3.110	3.473	3.494
18.6.67	11.83	1.989	2.592	3.102	3.467	3.497
29.6.67	11.87	2.008	2.614	3.112	3.471	3.493
30.6.67	11.84	2.001	2.601	3.107	3.478	3.499
Average	11.86 ± 0.01 (± 0.08%)	1.999 ± 0.005 (± 0.25%)	2.608 ± 0.006 (± 0.23%)	3.109 ± 0.002 (± 0.07%)	3.474 ± 0.003 (± 0.09%)	3.497 ± 0.002 (± 0.06%)

9.3 Energy fluence Measurements with the ionization chamber

Table 26 shows the reproducibility of ionization chamber measurements on various days. A similar procedure was carried out to that described for the calorimeter in 6 - 4. Two 0.006 mm sheets of aluminized 'Melinex' have to be inserted as filters in the beam to compensate for those used in the calorimeter. Measurements are in volts per monitor reading as shown in 7 - 6.

Table 27 shows the average responses quoted above when the corrections given in Table 25 have been applied. The errors quoted are again r.m.s. errors for the random errors of measurement and the uncertainties in the systematic error involved.

Table 27

X-ray beam	Response in volts/m.r.	% error
10kV 30mA	12.11 ± 0.06	± 0.50
15kV 30mA	2.040 ± 0.011	0.56
20kV 25mA	2.682 ± 0.017	0.64
25kV 15mA	3.194 ± 0.022	0.70
30kV 10mA	3.635 ± 0.036	1.00
30kV 30mA	3.659 ± 0.037	1.00

The integrating capacitors are nominally 1μF for integrations at 10kV 30mA, and 10μF for all other integrations. The method used to determine the absolute values of these capacitors is shown in Appendix 2. Results correct to ± 0.1% are as follows:-

Nominal value	Measured value (± 0.1%)
1μF	1.008μF
10μF	11.20μF

The aperture used was nominally 1/16 ins. in diameter, and the ratio of the calorimeter aperture (nominally 3/16 ins. diameter) to this aperture was determined by the calorimeter as shown in Appendix 1.2. This ratio was found to be 9.717 $\pm$ 0.019 ($\pm$ 0.2%).

9.4 Calculation of $\bar{W}$ for argon

If the measured saturation current is I amps, and the charge on an electron e coulombs, then $\frac{I}{e}$ is the number of ion pairs produced per second. An energy deposition of $\frac{\bar{W}I}{e}$ eV per second, or $\bar{W}I \times 10^7$ ergs per second is required to produce this number of ion pairs.

The defining aperture of the calorimeter has an area A_1 sq. cm., and that of the ionization chamber A_2 sq. cm., so the energy E as measured by the calorimeter is given by

$$E = \bar{W}I \times 10^7 \times \left(\frac{A_1}{A_2}\right) \text{ ergs per second} \quad \ldots\ldots\ldots 9 - 1$$

The ionization chamber response is a voltage V given by $V = \frac{It}{C}$, where t is the time of irradiation and C is the integrating capacitor. The monitor reading (m.r.) = monitor unit (m.u.) x t. Therefore the normalised response from the ionization chamber $\frac{V}{m.r.} = \frac{I}{C \times m.u.}$

Hence, from equation 9 - 1,

$$\frac{E}{m.u.} = \bar{W}C \left(\frac{V}{m.r.}\right) \times 10^7 \times \frac{A_1}{A_2}$$

and $$\bar{W} = \frac{1}{C} \times \frac{A_2}{A_1} \times \frac{E/m.u.}{V/m.r.} \times 10^{-7} \text{ eV per ion pair} \quad \ldots\ldots\ldots 9 - 2$$

$\bar{W}$ values are calculated using Table 16 and 27. For example, at 20kV 25mA

$$\bar{W}_{20} = \frac{1}{11.20 \times 10^{-6}} \times \frac{1}{9.717} \times \frac{7.652 \times 10^4}{2.682} \times 10^{-7} \text{ eV per ion pair}$$

$$\bar{W}_{20} = 26.21 \text{ eV per ion pair.}$$

The errors in this measurement are shown in Table 28.

Table 28

Error Source	Uncertainty %
Calorimetry	± 0.46
Ionization chamber	0.64
Capacitance	0.10
Aperture ratio	0.20
Total	± 0.82%

Therefore $\bar{W}_{20}$ = 26.21 ± 0.22 eV per ion pair

Similar calculations have been carried out for the other beams used, and the results are shown in Table 29.

Table 29

X-ray beam	$\bar{W}$ values (eV per ion pair)
10kV 30mA	26.18 ± 0.17
15kV 30mA	26.04 ± 0.19
20kV 25mA	26.21 ± 0.22
25kV 15mA	26.10 ± 0.24
30kV 10mA	26.12 ± 0.31
30kV 25mA	26.24 ± 0.30

9.5 Discussion of results

The above results show that there is no variation of $\bar{W}$ for argon in the X-ray region investigated, and the mean of these results gives $\bar{W}$ = 26.14 eV per ion pair. The effect of calculating the energy loss due to sidescatter

by $\int_{\phi=0}^{\frac{\pi}{2}}$ increases $\bar{W}$ by approximately 1% for each X-ray beam used. Again no variation of $\bar{W}$ is found, and the mean value is $\bar{W}$ = 26.43 eV per ion pair. The correct result will lie between these two values. As sidescatter energy losses predominate over backscatter energy losses in the ionization chamber, for both evaluations (5 - 3), it is suggested that $\int_{\phi=0}^{\pi}$ will produce a more correct result. However, a final result of $\bar{W}$ argon = 26.3 $\pm$ 0.25eV per ion pair covers any discrepancy produced by these two methods of evaluating the sidescatter energy loss. This result may be compared with ionization of argon by α particles (mean result 26.25 $\pm$ 0.10 eV per ion pair (table 18, pg 63)), and to that of Binks (55) who gave 27.0 $\pm$ 2.7 eV per ion pair.

The main source of error is again in the assumed spectral distributions, and a large error in the scatter corrections has therefore been quoted. The corrections are large at 30kV, and although $\bar{W}$ values agree well with those at lower energies, more accurate spectral distributions are really required.

The ionization chamber is relatively simple and quick to operate. The accuracy and reproducibility of the measurements, as shown in Table 26, are exceptionally good. As a routine dosimeter it is rather cumbersome, but it could be made smaller even for use with argon. Its present size was in order to allow substantial variations in the electrode spacing. A smaller chamber employing a higher atomic number gas would be a better proposition, and this should also allow higher kV radiation to be measured. It is hoped that such a chamber will be operational in the near future.

Figure 50

MOUNTING OF FERROUS SULPHATE SAMPLES

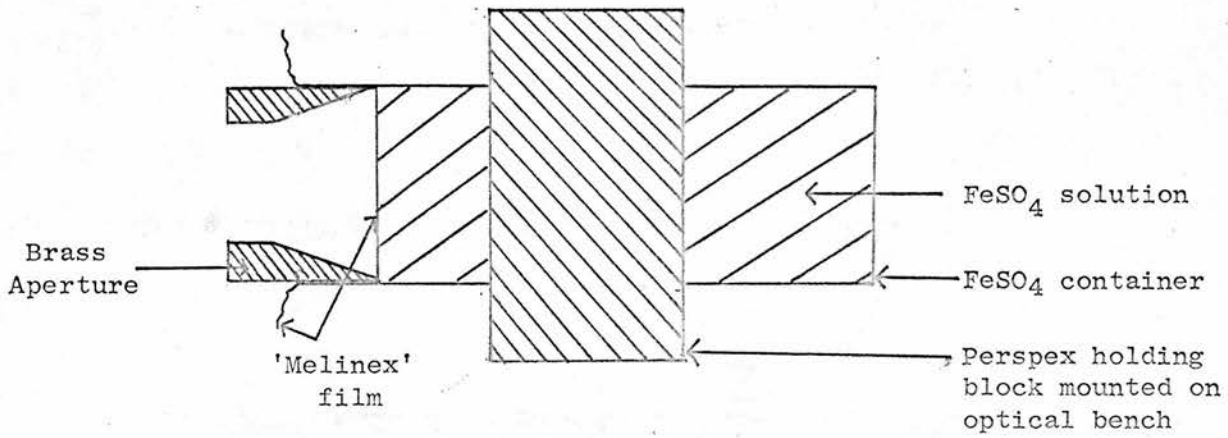

CHAPTER 10

FERROUS SULPHATE AND SOLID STATE DOSIMETRY

FERROUS SULPHATE DOSIMETRY

10.1 Introduction

One of the most widely used of chemical dosimeters is the ferrous sulphate or Fricke dosimeter. If the G value (ferric ion yield per 100 eV of absorbed energy) of ferrous sulphate is known, then absorbed dose in the dosimeter solution can be readily calculated. Ferrous sulphate G values have been extensively reviewed by Shalek, Sinclair and Calkins (69) and by Law (70), and a definite decrease in G value with decrease in energy is shown. Results at high energies are consistent, but relatively few determinations have been made at low energies, and uncertainties in published values are mainly about $\pm$ 5%. A comparison has therefore been carried out between the calorimeter and ferrous sulphate dosimetry.

10.2 Experimental conditions

Polythene vessels 2.25 cm in diameter and varying in length between 3 and 7 cm were used for irradiations. No noticeable error was found by allowing dosimeter solutions to stand in these vessels for a considerable length of time (71); nor did varying the surface to volume ratio produce any effect on the dosimeter response, and at Co^{60} qualities these vessels have been found to give the same response as glass vessels (72).

The ferrous sulphate vessels were mounted as shown in Figure 50. The entrance window which consisted of 0.006mm of 'Melinex' was held in place by a brass aperture. This aperture was again the same depth as that

used in the calorimeter, and positioning of the ferrous sulphate vessels was carried out as described in 2 - 6. No chemical contamination was produced by the 'Melinex'. The length of each individual sample so produced varied, and the volume of the ferrous sulphate in these samples was determined by measuring this length after each irradiation. 'Melinex' filtration also had to be added to balance that used in the calorimeter.

Theoretical and experimental verification of total absorption was carried out for each X-ray beam used. Detection of the transmitted beam through the samples was made by the calorimeter and this was shown to be much less than 0.1% for the experimental conditions used. Dosimeters of different lengths also gave the same ferric ion yield for a given radiation dose. Estimations of sidescatter and backscatter were calculated as in Chapter 5, and the results are shown in Table 32. The width of the margin of ferrous sulphate solution surrounding the incident beam was 0.69 cm for 20 kVp irradiations, and 0.49 cm for 15 kVp and 10 kVp irradiations.

10.3 Preparation of ferrous sulphate samples

These were made up of 10^{-3}M ferrous ammonium sulphate and 10^{-3}M sodium chloride in 0.8N sulphuric acid, as is generally used. All chemicals were 'Analar' grade. The water used was singly distilled, then redistilled from potassium permanganate in a glass apparatus. The method of making up these solutions is described by Law and Redpath (72).

10.4 Measurement of Ferric Ion concentration

Optical densities were measured in a Unicam SP 500 spectrophotometer at 3040 $\mathring{A}$. The spectrophotometer cells were of fused quartz, and any systematic error due to inconsistencies in these was removed by measuring,

in turn, the optical density of the irradiated sample and of a control sample against 0.8N H_2SO_4 in the blank cell. The optical density scale was found to be linear over the range used.

The extinction coefficient ε for Fe^{3+} at 3040 Å on this spectrophotometer was measured by comparing its response to that of a previously calibrated spectrophotometer at the Christie Hospital and Holt Radium Institute, Manchester. The result was 2130 ± 7 litre $mole^{-1}$ at 20°C. Measured optical densities were always normalised to 20°C by applying a correction of 0.7% per °C. Solution temperatures were measured by a thermocouple.

10.5 Dose variation and oxygen depletion

In the absence of oxygen the G value for ferrous sulphate is reduced by about a factor of two. The dosimeter solution used is linear in response up to approximately 40,000 rads, but after such a dose the lower G value applies. In this work the average absorbed dose is approximately 1500 rads, but in a small critical region at the front of the vessel the dose will probably exceed 40,000 rads. A comparison was therefore carried out between the Fe^{3+} yield in aerated (normal) and oxygenated solutions, both with 1mM and 4mM Fe^{2+}. Within experimental error these gave the same result, but all results were included in the calculation of G values. Thus it appears that oxygen diffusion maintains a sufficient oxygen concentration in the critical region, and this is verified by theoretical calculations.

10.6 Results and calculations of G values

Ferrous sulphate irradiations were carried out, over a period of

two months, and the results are shown in Table 30. Irradiations were one hour with 20kV and 15kV beams and two hours with 10kV beams. Optical densities obtained were about 0.1 , and results were normalised by the monitor unit.

Table 30

$FeSO_4$ responses in optical density per sec per cm per monitor unit x 10^6

Dates for	20kV 25mA	15kV 30mA	10kV 30mA
8.9.66	1.205	1.896	3.49
15.9.66	1.227	1.929	3.40
4.10.66	1.190	1.855	3.40
5.10.66	1.183	1.910	3.27
15.10.66	1.182	1.908	3.23
19.10.66	1.176	1.881	3.38
20.10.66	1.195	1.869	3.42
Weighted Means	1.191 ± 0.006	1.894 ± 0.008	3.38 ± 0.03

Calorimetric measurements were carried out over a similar period (Table 31). Experimental conditions were slightly different to those already quoted (Chapter 6), and the kinetic method of operation was used.

Table 31

Calorimeter response in ergs per monitor unit x 10^{-4}

Dates for	20kV 25mA	15kV 30mA	10kV 30mA
27.9.66	8.134	6.216	-
7.10.66	8.184	6.366	-
18.10.66	8.058	6.132	-
1.11.66	7.872	5.982	3.204
8.11.66	8.112	5.982	3.338
11.11.66	7.938	6.168	3.264
16.11.66	7.986	6.120	3.265
Weighted Mean	8.058 ± 0.048	6.138 ± 0.048	3.291 ± 0.021

G values were calculated as follows:-

Calorimeter response in ergs per monitor unit = E

Ferrous sulphate response in optical density per sec per cm per monitor unit = D

Volume of ferrous sulphate bottle = V

Avogadro's number = N

Extinction coefficient = ε

Area of calorimeter aperture = A_1

Area of ferrous sulphate aperture = A_3

Electronic charge = e

then

$$G = \frac{D}{E} \times \frac{VNe}{\varepsilon} \times \frac{A_1}{A_3} \times 10^9 \text{ ions/100eV}$$

For example, at 20kV and 25mA

$$G = \frac{1.191 \times 10^{-6} \times 19.88 \times 6.023 \times 10^{23} \times 1.602 \times 10^{-19} \times 10^9}{8.058 \times 10^4 \times 2130 \times 1.023} \text{ Ions/100eV}$$

$$G = 13.01 \text{ ions/100eV.}$$

Table 32

Corrections and Uncertainties for $FeSO_4$ dosimetry

Error Source	20kV	20kV	15kV	15kV	10kV
	Correction %	Uncertainty %	Correction %	Uncertainty %	Uncertainty %
Calorimetry		± 0.6		± 0.8	± 0.7
Optical density		0.5		0.4	1.0
ε		0.3		0.3	0.3
Backscatter $FeSO_4$	± 1.9	0.2	+ 1.3	0.2	
Sidescatter $FeSO_4$	+ 0.5	0.3			
Backscatter Cal.	- 1.4	0.3	- 0.5	0.1	
Aperture Sizes		0.1		0.2	0.2
$FeSO_4$ temp. correction		0.1		0.1	0.1
$FeSO_4$ sample volume		0.5		0.5	0.5
TOTAL	+ 1.0	± 1.1	+ 0.8	± 1.1	± 1.4

The ratio of the apertures used was 1.023 ($\frac{FeSO_4}{CAL}$) at 20kV and 2.153 at 15kV and 10kVp. This ratio was determined by a travelling microscope.

Table 32 shows the estimated uncertainties in these G values, and the correction which has to be applied for energy lost due to scattered radiation.

Irradiations were also carried out with 20kV X-rays using dosimeter solutions made up in 0.1N H_2SO_4. (Better approximation to tissue equivalence than 0.8N H_2SO_4). The extinction coefficient for Fe^{3+} in 0.1N H_2SO_4 is slightly lower than in 0.8N H_2SO_4, and 0.995 ± 0.001 (mean of six published results) was taken as this ratio. The ratio of G in 0.1N H_2SO_4 to G in 0.8N H_2SO_4 was found to be 0.986 ± 0.005. Table 33 summarises the G values obtained in this work.

Table 33

X-ray beam	$G_{Fe^{3+}}$ in	
	0.8N H_2SO_4	0.1N H_2SO_4
20 kV	13.14 ± 0.14	12.96 ± 0.15
15 kV	13.01 ± 0.14	
10 kV	12.87 ± 0.18	

SILICON SURFACE BARRIER SEMICONDUCTOR DETECTOR

10.7 P-N Junction

A P-N junction can be thought of as a piece of P type and a piece of N type semiconductor brought together and joined. Electrons flow from the N type to the P type material under diffusion, resulting in a negative

charge on the P type and a positive charge on the N type. Thus a potential difference exists across the junction. The region close to this junction is almost carrier free and called the depletion layer. There is a residual diffusion current of about 10^{-9} amps per cm^2.

By applying a reverse bias to the junction, the potential barrier can be increased in height and the width of the depletion layer increased. The effective resistance of the depletion layer is much greater than that of the material on each side of the junction, and therefore almost all of the applied voltage appears across this layer. A relatively high leakage current in the direction of the applied bias is now present, and the dominant component of this current is due to surface leakage. The depletion layer is radiation sensitive and is analogous in operation to an ionization chamber.

A surface barrier detector is formed by exposing N type silicon to the atmosphere, resulting in a very thin layer of P type silicon forming on the surface due to oxidization. Electrodes are made by depositing a very thin layer of gold (80 μgrams per cm^2) on the surface. The detector used is approximately 3mm in thickness and the junction 2 sq. cm. in area.

10.8 Operation of the detector.

The detector is sensitive to light and the leakage current can be reduced by operation in the dark. However this leakage current is still appreciable compared to the ionization currents which have to be measured, and it is therefore backed off with a high impedance current source. The detector is mounted in a chamber similar to that used in the calorimeter, and also aligned on the optical bench in a similar manner. The chamber is evacuated and 'Melinex' filtration added so that the total filtration is the same as that used in the calorimeter.

Table 34

Semiconductor response to various X-ray beams
(in volts per monitor reading)

Date	10kV 30mA	15kV 30mA	20kV 25mA	25kV 15mA	30kV 10mA	30kV 25mA
7.6.67	6.462	12.20	16.11	18.88	20.91	21.12
12.6.67	6.450	12.20	16.10	18.92	21.03	21.30
14.6.67	6.416	12.12	16.09	18.87	20.99	21.27
15.6.67	6.439	12.19	16.07	18.81	20.89	21.13
26.6.67	6.403	12.21	16.08	18.85	20.95	21.20
29.6.67	6.439	12.18	16.07	18.79	20.88	21.09
Average	6.435 ± 0.009 (± 0.14%)	12.18 ± 0.02 (± 0.16%)	16.09 ± 0.01 (± 0.06%)	18.85 ± 0.02 (± 0.11%)	20.94 ± 0.03 (± 0.14%)	21.18 ± 0.03 (± 0.14%)

Saturation of the detector takes place above 10 volts reverse bias. The breakdown potential is quoted as approximately 120 volts, and 96 volts bias has been used throughout this work. The saturation currents were integrated on the same system that was used for the ionization chamber (shown in Figure 42), and a response obtained for various X-rays beams again expressed in volts per monitor reading. By a comparison with the calorimeter, $\bar{W}$ values for silicon were obtained for these various X-ray beams. The same aperture was used for both calorimetric and semiconductor measurements, and the integrating capacitor used for semiconductor measurements was $126.1\mu F \pm 0.1\%$ (Appendix 2).

10.9 Results and $\bar{W}$ calculations

The consistency of the semiconductor detector on various days and for various X-ray beams is shown in Table 34. The corrections to be applied to these results are more involved for this dosimeter. Scatter corrections are mainly due to Compton and Rayleigh backscatter, sidescatter is negligible. However corrections have to be applied for attenuation in the gold electrode at the front of the dosimeter, and transmission corrections now become substantial. Total corrections are shown in Table 35 for the various X-ray beams used.

Table 35

X-ray beam peak energy	% energy loss	Estimated uncertainty %
10kV	3.5	± 1.0
15kV	2.4	0.6
20kV	2.1	0.5
25kV	3.0	1.0
30kV	3.9	1.0

Corresponding calorimetric measurements are given in Table 16, and $\bar{W}$ values were calculated from equation 9 - 2. Results with their uncertainties are shown in Table 36.

Table 36

X-ray beam	$\bar{W}$ value (eV per ion pair)
10kV 30mA	3.695 ± 0.037
15kV 30mA	3.676 ± 0.027
20kV 25mA	3.693 ± 0.025
25kV 15mA	3.706 ± 0.042
30kV 10mA	3.764 ± 0.043
30kV 25mA	3.765 ± 0.043

10.10 Discussion and conclusions

$\bar{W}$ values obtained are consistent for X-rays generated at 25kV and below, and an average of these results gives $\bar{W} = 3.693 \pm 0.020$ eV per ion pair for the detector used. Results for 30kV X-rays are however, approximately 2% high compared to this mean. The reason for this almost certainly lies in the correction applied for lack of total absorption. A monochromatic beam of 30keV X-rays is only 65% absorbed in 3mm of silicon, and thus it is the high energy end of the spectrum which is critical in determining this lack of total absorption. This is however extremely difficult to determine in practice, and it does appear that the spectrum used is weighted too heavily at the low energy end.

In theory it is only the depletion layer which is radiation sensitive. However, because of the intrinsic resistivity of silicon, there will be a potential gradient across the remainder of the detector, and some

ion collection must occur in this region. As saturation occurs with the bias voltage reduced by a factor of 10, it appears that saturation may also have been attained in this region.

Calculations also show that the depletion layer extends well into the N type layer of the detector. The width of the depletion layer X, is given by

$$X = 4.2 \times 10^{-7} (\varepsilon V \rho \mu)^{\frac{1}{2}} \text{ cm}$$

where ε is the dielectric constant of the crystal.

V is the reverse bias.

ρ is the resistivity of the parent crystal.

μ is the mobility of the majority carriers.

Using the appropriate values gives X = 2mm. (This calculation assumes that all of the applied voltage is dropped across the depletion layer).

Of the four dosimeters used there is little doubt that the semiconductor detector is the most versatile in all respects. It is quick to set up, measurements can be made with speed and precision, and it is readily portable. Its drawbacks at the moment are cost, and the difficulty of manufacturing crystals of any appreciable size. These will doubtless be overcome.

APPENDIX 1

A1.1 Lining up of calorimeter

An additional procedure was carried out in the lining up of the calorimeter. The relative areas of various apertures were determined by the response of the solid state detector at a particular X-ray quality (30kV 25mA). A similar experiment was then carried out with the calorimeter under the experimental conditions described in 2 - 6. It is certain that the total X-ray beam transmitted by these apertures is measured by the solid state detector, but not certain in the case of the calorimeter. Results obtained are as follows.

Aperture No.	Nominal Diameter of apertures (ins)	Solid state Response (Volts$_{/m.r.}$)	Calorimeter Response (ergs$_{/m.r.}$ x 10^{-4})	Ratio of Solid State to Calorimeter
1	$^{1}/_{16}$	2.213	1.043	2.122
2	$^{1}/_{8}$	9.121	4.296	2.123
3	$^{5}/_{32}$	15.72	7.418	2.119
4	$^{11}/_{64}$	16.85	7.933	2.124
5	$^{3}/_{16}$	21.05	9.948	2.116
6	$^{13}/_{64}$	24.33	11.50	2.116
7	$^{7}/_{32}$	28.61	13.59	2.105

The ratio of the solid state detector response to the calorimeter response is reasonably constant over the apertures used. However, all calorimeter results have been taken using aperture 5.

A1.2 Determination of aperture ratio

The aperture used in the ionization chamber work was No. 1, and the ratio of this aperture to that used in calorimetry was determined by the calorimeter. The response to 30kV 25mA X-rays, using each aperture, was measured on various days. Results are as follows.

Date	Calorimeter Response to Aperture No.5	Calorimeter Response to Aperture No.1	Aperture ratio No.5/No.1
13.6.67	10.28	1.060	9.698
27.6.67	10.32	1.060	9.736
6.7.67	10.30	1.055	9.763
12.7.67	10.23	1.057	9.678

The mean of the above results gives 9.719 ± 0.019 (0.2%) for the required aperture ratio.

Figure 51

CIRCUIT FOR ABSOLUTE MEASUREMENT OF CAPACITANCE

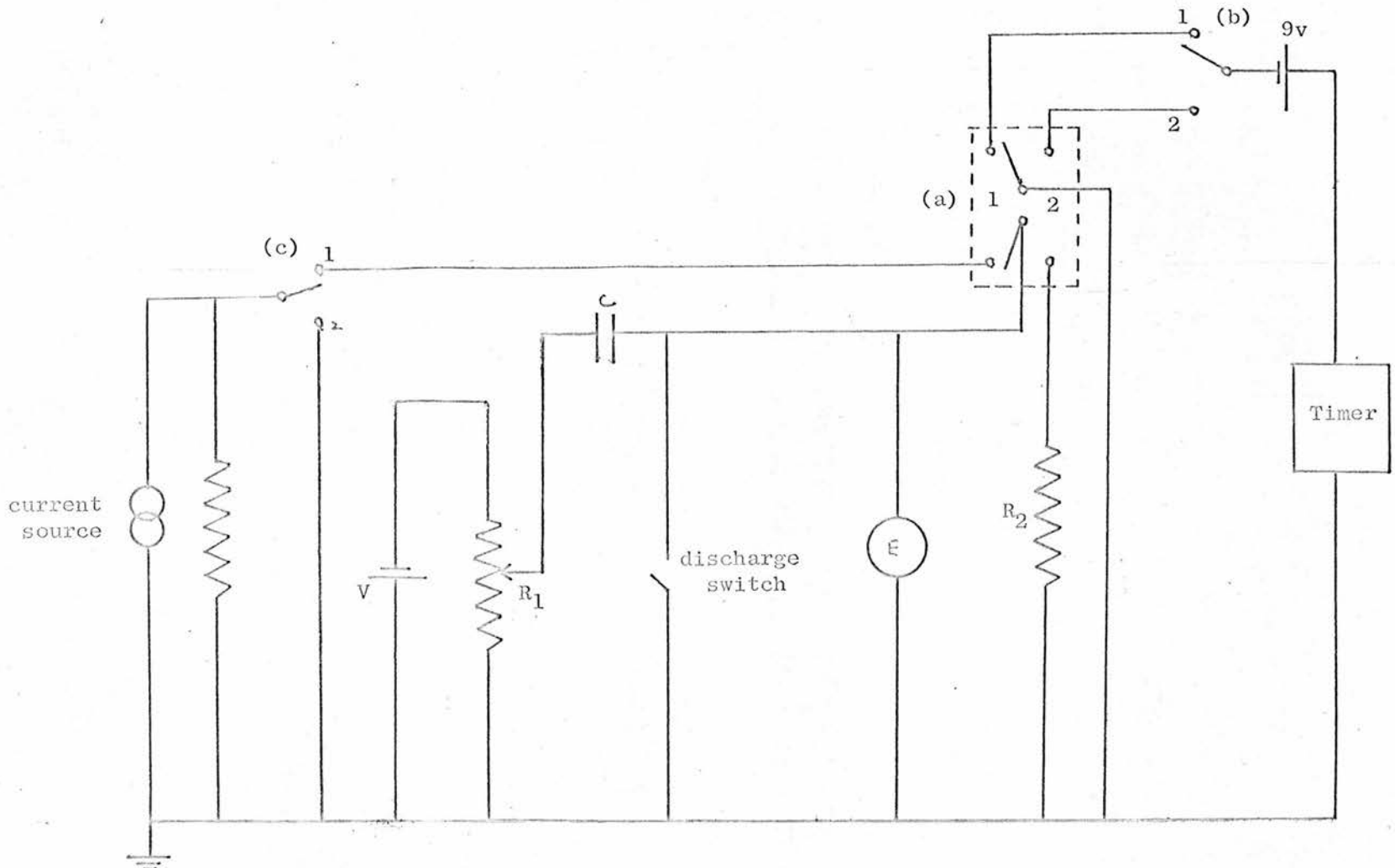

R_1 - 10KΩ decade box

R_2 - 1MΩ decade box ($\pm$ 0.1%)

E - electrometer

V - standardised voltage

C - unknown capacitor

APPENDIX 2

A2.1 Absolute Measurement of Capacitance

Commercial instruments which provide an accurate measurement of capacitance are readily available, but all use an a.c. bridge measuring system. Capacitors usually show an increase in value with a decrease in frequency (this may be as much as 2% between 1kcps and d.c. operation). The integrating capacitors are obviously used in d.c. operation, and figure 51 shows the system developed to obtain absolute values under this condition. The system simply measures the time constant of decay of the capacitor through a resistor of known value.

The procedure is as follows. Start with switch (a) in position 1, switches (b) and (c) in position 2. The capacitor C, to be measured, is charged by switching (c) to position 1 and then back to position 2. The current source must be of high impedance to ensure that charging takes place, so an E.H.T. unit in series with a high resistance was used. The voltage V_o, built up on the capacitor is seen on the electrometer E, and measured by the backing off system previously described (6 - 1).

Switching (a) to position 2 discharges the capacitor through a 1MΩ ($\pm$ 0.1%) resistor R_2, and triggers the timer with a 9V positive pulse. Switch (b) is then returned to position 1. Switching (a) back to position 1 then reverses this procedure, it stops the capacitor discharging and stops the timer with another positive pulse. The voltage V remaining on the capacitor is again measured by backing off.

An oven controlled crystal timer accurate to better than 0.1% is used. The error in switching is unlikely to exceed $\pm$ 5 ms., and as the measured time t is always greater than 10 sec., the error introduced will

be negligible. The natural decay of the capacitor is also much less than 0.1% of the measured decay. As the largest available standard resistor was 1MΩ, the decay time constant of the 1 μF capacitor is only 1 sec, and therefore was not measured on this system.

The time constant T is given by

$$V = V_o \exp\left(-\frac{t}{T}\right)$$

$$T = t\left(\ln \frac{V_o}{V}\right)^{-1}$$

$$R_2C = t\left(\ln \frac{V_o}{V}\right)^{-1}$$

$$C = t\left(\ln \frac{V_o}{V}\right)^{-1} \mu F$$

The nominal 100μF and 10μF capacitors were measured in this way. Readings were taken on several days, but any individual reading on any day did not vary from the mean by more than 0.1%. Results are as follows.

Nominal capacitor value	10μF	100μF
Measured capacitor value	11.20μF	126.1μF

$$\text{Ratio } \frac{100\mu F}{10\mu F} = 11.26$$

An independent experiment to determine the ratio of the capacitors was carried out with the ionization chamber. The saturation current obtained from a particular X-ray beam was integrated in turn on each of the three capacitors. These responses were normalised by their corresponding monitor readings. A mean of several readings gave the following ratios.

$$\text{Ratio } \frac{100\mu F}{1\mu F} = 125.1 \qquad \text{Ratio } \frac{100\mu F}{10\mu F} = 11.26 \qquad \text{Ratio } \frac{10\mu F}{1\mu F} = 11.11$$

The ratio $\frac{100\mu F}{10\mu F}$ agrees with that obtained above, and the other two ratios both give a value of 1.008μF for the nominal 1μF capacitor. It is estimated that the obtained capacitor values are correct to ± 0.1%.

ACKNOWLEDGEMENTS

I should like to thank:-

My supervisors, Professor J. R. Greening and Dr. K. J. Randle for continual guidance throughout this work.

Dr. J. Law for his work on ferrous sulphate dosimetry and Dr. K. J. Randle for his work on solid state dosimetry. Without such work the writing of Chapter 10 would have been impossible.

Dr. J. M. M. Neilson for useful discussions on the building of the electrical circuit for calorimetry.

The workshop staff of the Medical Physics department of the Royal Infirmary and of the Western General Hospital, Edinburgh, for the building of apparatus.

The Medical Research Council for financing the entire project.

REFERENCES

1. Cameron, J. R., Daniels, F., Johnson, N. and Kenney, G. Science 134, 333 (1961).

2. Genna, S., Jaeger, R. G., Nagl, J. and Sanielevici, A. Atomic Energy Rev., 1, No. 4, 239, (1963).

3. Myers, I. T., Le Blanc, W. H. and Fleming, D. M. AEC Progress Report Contract AT(45-1)-1350, (1961).

4. Ginnings, D. C., Ball, A. F. and Vier, D.T. J. Res. Natl. Bur. Std., 50, 75, (1953).

5. Genna, S. and Laughlin, J. S. Radiology, 65, 394, (1955).

6. Laughlin, J. S., Beattie, J. W., Henderson, W. J. and Harvey, R. A. Am. J. Roentgenol., Radium Therapy, Nucl. Med., 70, 294, (1953).

7. Kruglov, S. P. and Lopatin, I. V. Translated from Pribory i Tekhnika Eksperimenta, 4, 53, (1963).

8. Schleiger, E. R., Goldstein, N. and Tochilin, E. U.S.N.R.D.L.- T.R.-621, (1963).

9. Dove, D. B. and Cole, B. G. A.E.R.E. - R 3063, (1962).

10. Gomberg, H. J., Atkins, M. C., Clendinning, W. R., Siemon, R. E., Wegst, W. F. Jr. and Gordus, A. A. Michigan University Memorial-Phoenix Project Res. Rep., Ann Arbor, Michigan, (1965).

11. Schleiger, E. R. and Goldstein, N. Rev. Sci. Instr., 35, 890, (1964).

12. Goodwin, P. N. and Adair, H. W. Radiology, 81, 320, (1963).

13. Tian, A. J. Chim. Phys., 20, 132, (1922).

14. Radak, B. and Markovic, V. Intern. J. Appl. Radiation Isotopes, 13, 287, (1962).

15. Redpath, A. T., Law, J., Greening, J. R. and Randle, K. J. In "Solid State and Chemical Radiation dosimetry in Medicine and Biology", p. 241. I.A.E.A., Vienna, (1967).

16. Keene, J. P. and Law, J. Phys. Med. Biol., 8, 83, (1963).

17. Bewley, D. K. Brit. J. Radiol., 36, 865, (1963).

18. Gunn, S. R. Nucl. Instrum. Meth., 29, 1, (1964).

19. Gunn, S. R. U.C.R.L. - 50173 (1967).

20. Kulenkampff, H. Ann. d. Physik., 79, 97, (1926).

21. Crowther, J. A. and Bond, J. Phil. Mag., 6, 401, (1929).

22. Rump, W. Z. Physik., 44, 396, (1927)., 43 , 254 , (1927).

23. Laughlin, J. S. and Beattie, J. W. Rev. Sci. Instr. 22, 572, (1951).

24. Pauly, H. Strahlentherapie, 110, 462, (1959).

25. Coekelbergs, R., Crucq, A., Decot, J., Degols, L., Frennet, A. and Timmerman, L. J. Chim. Phys., 62, 1277, (1965).

26. 'Evanohm' supplied by Gilby-Brunton Ltd., Seamill, Musselburgh, Scotland.

27. Roberts, J. K. "Heat and Thermodynamics", Blackie and Son Ltd., London and Glasgow, p.274.

28. Laughlin, J. S. and Genna, S. In "Radiation Dosimetry", 2nd ed., 2, 403, Academic Press, New York and London, (1966).

29. Handbook of Chemistry and Physics (38th ed.) Chemical Rubber Publishing Co., Cleveland, (1956).

30. Milvy, P., Genna, S., Barr, N. and Laughlin, J. S. Proc. 2nd Int. Conf. Peaceful Uses At. Energy, Geneva, 58, Vol. 21, p.142. Columbia Univ. Press (I.O.S.), New York, (1958).

31. Beakley, W. R. J. Sci. Instr., 28, 176, (1951).

32. Mitvalsky, V. J. Sci. Instr., 41, 454, (1964).

33. Quigg, R. K. Elec. Eng., 38, 92, (1966).

34. Unsworth, M. H. Private Communication. Dept. of. Med. Phys., Univ. of. Edinburgh.

35. Stainer, H. M. Bureau of Mines, United States Department of the Interior, IC - 8166, (1963).

36. Blokhin, M. A. AEC - tr - 4502, p.228, (1957).

37. Compton, A. H. and Allison, S. K. "X-rays in theory and experiment", D. Van Nostrand Company, Inc., New York, (1954).

38. McGinnies, R. T. Natl. Bur. Std. (U.S.) suppl. to circular 583, (1959).

39. Hurst, G. S., Bortner, T. E. and Glick, R. E. J. Chem. Phys., 42, 713, (1965).

40. Fano, U. Phys. Rev., 70, 44, (1946).

41. Erskine, G. A. Proc. Roy. Soc., A, 224, 362, (1954a).

42. Valentine, J. M. and Curran, S. C. Rep. Progr. Phys. 21, 1, (1958).

43. Lehmann, J. F. Proc. Roy. Soc. A, 115, 624, (1927).

44. Gaertner, O. Ann. Phys., Lpz., 16, 613, (1933).

45. Gaertner, O. Ann. Phys., Lpz., 21, 564, (1934/5).

46. Gaertner, O., Ann. Phys., Lpz., 23, 285, (1935).

47. Crowther, J. A. and Orton, L. H. H. Phil. Mag., 13, 505, (1932).

48. Wilhelmy, E. Z. Phys., 83, 341, (1933).

49. Gerbes, W. Ann. Phys., Lpz., 30, 169, (1937).

50. Valentine, J. M. and Curran, S. C. Phil. Mag., 43, 964, (1952).

51. Jesse, W. P. and Sadauskis, J. Phys. Rev., 90, 1120, (1953).

52. Haeberli, W., Huber, P. and Baldinger, E. Helv. Phys. Acta., 25, 467, (1952).

53. Bortner, T. E. and Hurst, G. S. Phys. Rev. 93, 1236, (1954).

54. Reid, W. B. and Johns, H. E. Rad. Res. 14, 1, (1961).

55. Binks, W. Acta Radiol., Suppl., 117, 85, (1954).

56. Curran, S. C., Cockroft, A. L. and Insch, G. M. Phil. Mag., 41, 517, (1950).

57. Valentine, J. M. Proc. Roy. Soc. A, 211, 75, (1952).

58. Phipps, J. A., Boring, J. W. and Lowry, R. A. Phys. Rev. 135, A.36, (1964).

59. Bunde, E., Lang, D., Pohlit, W. and Sewkor, A. Z. Naturforch., 9a, 129, (1954).

60. Rajewsky, B. and Lang, D. Nature, 190, 249, (1961).

61. Weiss, J. and Bernstein, W. Phys. Rev., 98, 1828, (1955).

62. Weiss, J. and Bernstein, W. Phys. Rev., 103, 1253, (1956).

63. Jaffe, G. Ann. Phys., Lpz., 42, 303, (1913).

64. Lea, D. E. Proc. Camb. Phil. Soc., 30, 80, (1934).

65. Kara Michailova, E. and Lea, D. E. Proc. Camb. Phil. Soc., 36, 101, (1940).

66. Mie, G. Ann. Phys. Lpz., 13, 857, (1904).

67. Boag, J. W. and Wilson, T. Brit. J. Appl. Phys., 3, 222, (1952).

68. Greening, J. R. Phys. Med. Biol., 9, 143, (1964).

69. Shalek, R. J., Sinclair, W. K. and Calkins, J. C. Rad. Res., 16, 334, (1962).

70. Law, J. In press.

71. Pettersson, C. and Hettinger, G., Acta Radiol., 6, 160, (1967).

72. Law, J. and Redpath, A. T. In press.

73. Greening, J. R. Brit. J. Appl. Phys., 6, 73, (1955).